DESIGN OF MEDIUM PRESSURE NOZZLES FOR COOLING TOWERS

by

John Edward Thacker

Thesis presented in partial fulfilment of the requirements for the degree of Master of Engineering at the University of Stellenbosch.

Thesis Supervisor: Prof. P.J. Erens

Department of Mechanical Engineering
University of Stellenbosch

May 1997

DECLARATION

I, the undersigned, hereby declare that the work contained in this thesis is my own original work and has not previously, in part or its entirety, been submitted at any university for a degree.

(Signature of candidate)

day of . 1997

ABSTRACT

This project concerns the investigation of parameters controlling the behaviour of full-cone spray nozzles of the type used in cooling towers.

In the present study large medium pressure hollow and full cone nozzles were investigated. A literature survey provided insight into the relationships between the nozzle dimensions and their spray characteristics, while equations found in the literature were used to correlate the experimental data.

It was found that the spray cone angle of hollow cone nozzles could be manipulated by using rounded orifice outlets and this finding lead to the development of a uniquely profiled outlet that actually produces a square spray pattern.

More experimental work was done to determine the relationship between the central jet of a full-cone nozzle and the other major nozzle dimensions. These results were then correlated and formulated into a set of guidelines for designing full-cone nozzles.

OPSOMMING

Hierdie projek behels 'n studie van belangrike parameters in volkegel sproeimondstukke soos gebruik in koeltorings.

In die huidige studie word groot mediumdruk holkegel en volkegel sproeimondstukke ondersoek. 'n Literatuurstudie het die nodige insig verskaf omtrent die verwantskap tussen mondstuk dimensies en hul spuitkarakteristieke, terwyl vergelykings uit die literatuur gebruik is om die eksperimentele data te korreleer.

Dit was gevind dat die sproeir kegelhoek van die holkegelmondstuk verander kon word deur gebruik te maak van geronde uitlate. Afleidings wat gemaak is het gely tot die ontwikkeling van 'n unieke geprofielde uitlaat wat 'n vierkantige sproeipatroon gelewer het.

Bykomstige eksperimentele werk is gedoen om die verwantskap tussen die sentralestraal van 'n volkegelmondstuk en die ander hoof mondstukdimensies te bepaal. Die reultate is verwerk om riglyne vir die ontwerp van vierkantige patroon volkegel mondstukke daar te stel.

ACKNOWLEDGEMENTS

I would like to express my sincere appreciation to the following persons and institutions:

Prof. P.J. Erens for his guidance, patience and encouragement;

Boet, George and Scotty for their patience and technical assistance;

Industrial Water Cooling(Pty)Ltd for their interest and financial support;

Foundation for Research and Development for their financial support.

TABLE OF CONTENTS

NOMENCLATURE

List of Symbols

A	Area	[m^2]
A_R	Aspect ratio	[-]
B_f	Coefficient in Equation (B-6)	[-]
B_t	Coefficient in Equation (B-9)	[-]
B_σ	Coefficient in Equation (B-8)	[-]
b	Width of spray	[m]
C	Discharge Coefficient	[-]
d	Diameter	[m]
E	Flow coefficient	[-]
F	Flow loss coefficient	[-]
FN	Flow number	[m^2]
g	Gravitational constant	[m^2/s]
h	Height	[m]
I	Rainfall intensity	[kg/m^2s]
K	Nozzle parameter	[-]
l	Length	[m]
$\dot{m}$	Mass flow rate	[kg/s]
m	Fluid flow index	[-]
n	Number of data points	[-]
P	Pressure	[N/m^2]
$\dot{q}$	Volume flow rate	[m^3/s]
Re	Reynolds number	[-]
r	Radius	[m]
s	Swath width	[m]
t	Film thickness	[m]
U	Total velocity	[m/s]
U_p	Pressure velocity	[m/s]
V	Dimensionless axial velocity	[-]
v	Axial velocity	[m/s]

W	Dimensionless tangential velocity	[-]
w	Tangential velocity	[m/s]
x	Ratio of air-core area to orifice area	[-]
y	Nozzle constant of Taylor[48TA1]	[-]

List of Greek Symbols

α	Half spin chamber angle	[°]
β	Ratio of flow meter orifice diameter to pipe diameter	[-]
ΔP	Pressure drop	[Pa]
Δt	Time lapse	[s]
ϕ_n	Cone angle on rounded nozzle exit	[°]
γ	Port helical exit angle	[°]
λ	Wall friction coefficient	[-]
μ	Absolute viscosity	[kg/ms]
ν	Kinematic viscosity	[m^2/s]
θ	Half spray cone angle	[°]
ρ	Density	[kg/m^3]
σ	Dependent variable in Equation (B-7)	[-]
Ω	Rotational constant	[m^2/s]

List of Subscripts

a	Ambient conditions
c	Core
e	Entry
ep	Predicted entry
fm	Flow meter
gi	Generalised inlet
i	Indexing variable
Hg	Mercury
j	Jet

m	Mean of inlet and outlet values
n	Nozzle
o	Orifice
p	Swirl port
r	Frictional
rs	Rain sampler
s	Swirl chamber
sc	Sudden contraction
se	Sudden expansion
sw	Swirler

List of Dimensionless Groups

$C = \frac{\dot{q}}{\sqrt{2\Delta P_n \rho}}$ Discharge coefficient

$K = \frac{A_p}{d_s d_o}$ Nozzle parameter

$Re = \frac{\rho v d}{\mu}$ Reynolds number

$s = \frac{b}{2h}$ Swath coefficient

$V = \frac{v}{U_o}$ Dimensionless axial velocity

$W = \frac{w}{U_o}$ Dimensionless tangential velocity

$X = \frac{A_c}{A_o}$ Ratio of air-core area to orifice area

$x = \frac{v_o}{U_p}$ Ratio of axial velocity to pressure velocity

$y = \frac{\Omega}{r_o U_p}$ Nozzle constant of Taylor [48TA1]

$z = \frac{r_c}{r_o}$ Ratio of air-core radius to orifice radius

List of Acronyms

ABS	Acrylonitrile-butadiene-styrene
AVG	Standard average
FCN	Full-cone nozzle
FN	Flow number
HCN	Hollow cone nozzle
LHS	Left hand side
NC	Numerical control
PA	Polyamide
PBTP	Polybutylene terephthalate
PC	Polycarbonate
PE	Polyethylene
PIM	Plastic injection moulding
POM	Polyoxymethylene
PP	Polypropylene
PVC	Polyvinylchloride
RHS	Right hand side
RID	Rainfall intensity distribution
STD	Standard deviation
UV	Ultra violet

CHAPTER ONE

INTRODUCTION

This thesis is about designing new more effective nozzles for water distribution in cooling towers. The nozzles are not necessarily revolutionary, but their distribution is seen to be predictable and acceptable for application to the task of wetting cooling tower fill packs. The thesis title, "The Design of Medium Pressure Nozzles for Water Distribution in Cooling Towers", clearly defines the content of this thesis.

The word ***design*** implies a definite need for the development of better cooling tower nozzles. There are three reasons for the implementation of this project. First, the cooling tower industry in South Africa is dependent on imported brands of nozzle for use in its towers. The cost of these nozzles is becoming increasingly high and it is often difficult to obtain nozzles at short notice. Manufacturing nozzles locally would alleviate both these problems.

Second there is the problem of questionable nozzle performance, i.e. poor distribution. This problem can be addressed by studying existing nozzles and by looking for ways to optimise nozzle performance. The ultimate goal of this project is to provide a blueprint for designing more effective nozzles.

Third there is the problem of cooling tower performance – discussed in the literature survey. The cooling capacity of evaporative cooling towers is adversely affected by maldistribution of water to the fill pack. The design of more *effective* nozzles will alleviate the problem of poor water distribution and hence increase tower performance.

The question of operating pressure is a key issue as far as nozzles are concerned. Not only are the pumping costs proportional to nozzle supply pressure, but atomisation too is very much a function of nozzle injection pressure – according to Lefebvre [89LE1] drop diameter is inversely proportional to the cube root of pressure. For these reasons it has been necessary to limit the scope of this thesis to ***medium pressure*** nozzles only.

Low-pressure nozzles typically require pressures of between 5 kPa and 15 kPa. Applications for these nozzles are; water distribution in large natural draught wet cooling towers and

irrigation. Medium pressure refers to the range 20 kPa to 100 kPa. It is in this range that nozzles for mechanical draught cooling towers see Figure 1-2, operate. High-pressure nozzles are smaller in physical dimension than other nozzles. They operate at pressures anywhere between 700 kPa and 2000 kPa. These nozzles produce very fine sprays – droplets are in the order of 10 μm in diameter. A typical application for these nozzles is in the combustion of liquid fuels.

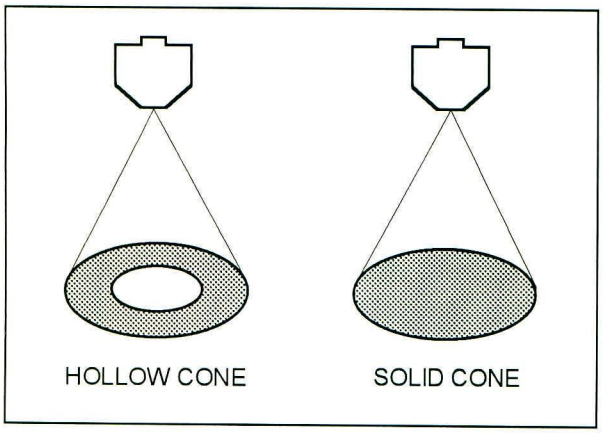

***Figure 1 - 1**: Spray patterns of simplex atomisers.*

The question arises as to which type of ***nozzle*** is most suitable for the task of wetting cooling tower fill packs? The answer to this question is the pressure-swirl or simplex atomiser. There are two basic types of simplex atomiser and they are classified according to their spray patterns. Firstly the *hollow-cone* nozzle, HCN, as the name implies, produces a spray in which most of the droplets are concentrated at the outer edge of a conical spray sheet. The traditional garden-variety sprinkler is the perfect example of a hollow cone nozzle. Secondly the *solid*, or *full-cone* nozzle, FCN, produces the same conical-shaped spray as the HCN, but it is now made up of a fairly uniform distribution of droplets throughout its volume. The two spray structures are depicted in Figure 1-1.

Obviously it is the FCN which must be used for the uniform ***distribution of water*** over a large surface area such as a cooling tower fill pack. However, since the FCN is simply the combination of a swirl atomiser and an axially aligned central jet, see Figure 2-3, it was necessary to study the swirl atomiser independently from

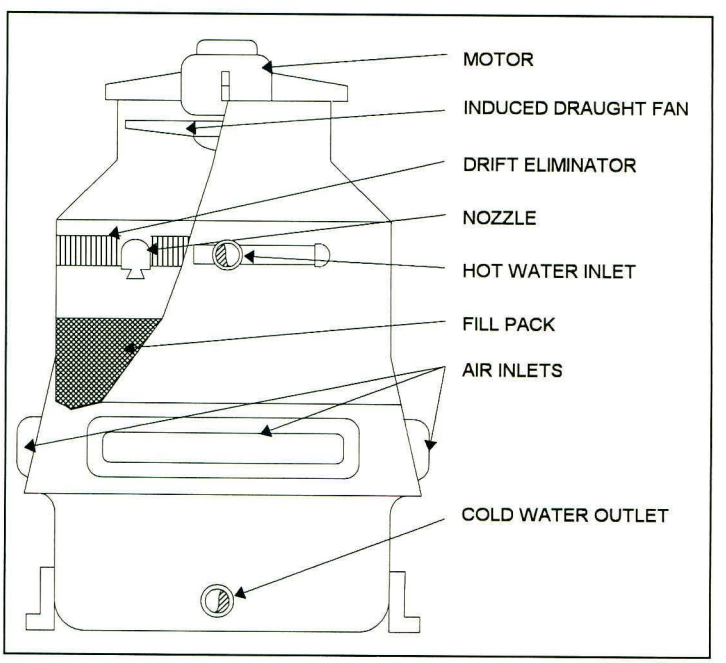

***Figure 1 - 2**: Mechanical draft cooling tower.*

the FCN. Much of the theoretical and experimental work was, therefore, concerned with the analysis of the HCN so that a more complete understanding of the FCN could be gained.

The aim of this thesis is to enable uniform water distribution in ***cooling towers***. Evaporative cooling towers are widely used in industry, and where natural draught cooling towers might be limited for use in power generation, industrial type mechanical draught cooling towers of the type depicted in Figure 1-2 are used extensively in many other industrial processes.

The first essential task for this project was to conduct a literature survey on hollow and full cone nozzles to become familiar with their operation and characteristics, while at the same time noting the relationship between the major nozzle dimensions and the flow characteristics of such nozzles. Empirical formulae and experimental correlations were also duly recorded for use in correlating any new experimental data.

Next an experimental investigation of HCNs had to be conducted to determine the relationship between the major nozzle dimensions, namely orifice diameter, d_o, swirl chamber diameter, d_s, and swirl port area, A_p, and the three fundamental flow characteristics, discharge coefficient, C_n, spray cone angle, 2θ, and film thickness, t. The emphasis of these experiments fell on determining accurate correlations that could be used to predict any of these characteristics for any flow condition that might arise inside a medium pressure cooling tower.

The next objective was to build and test various FCN configurations to observe and quantify the effect of the central jet on radial spray distribution and rainfall intensity. The scope of the experimental research was geared towards understanding FCNs under typical operating conditions, i.e. nozzle injection pressures, P_n, of between 25 and 65 kPa. This experimental data could then be correlated to reveal formulas for predicting rainfall intensity distribution, RID, as a function of injection pressure and total mass flow rate, $\dot{m}$.

Finally and most importantly a means of producing a *square* spray had to be investigated and mathematically recorded for future reproduction. Ultimately the experimental and theoretical analysis was to culminate in a comprehensive design code for designing FCNs for specific operating conditions including: nozzle injection pressure, P_n, installation height, h, spray area and required rainfall intensity, I.

CHAPTER TWO

LITERATURE SURVEY

The purpose of this chapter is not to delve into the complex nozzle theories of the various authors, but rather to summarise the findings relevant to medium pressure nozzle design. A more detailed reproduction of the formulas relating to nozzle characteristics and performance is given in Chapter 3.

2.1 Pressure-swirl atomisers

The simplest form of HCN is the simplex swirl atomiser, see Figure 2-1. Liquid is fed through tangential ports into the swirl chamber. The high angular velocity of the fluid in the swirl chamber results in the formation of an air-cored vortex, which is concentric with the axis of the nozzle. The outlet from the nozzle is the final orifice, the diameter of which is less than that of the swirl chamber. Conservation of linear and angular momentum requires that the fluid accelerates as it flows, under both axial and radial forces, along the nozzle and out through the final orifice. The spray cone angle, 2θ, is determined by the axial and tangential components of velocity at the nozzle exit.

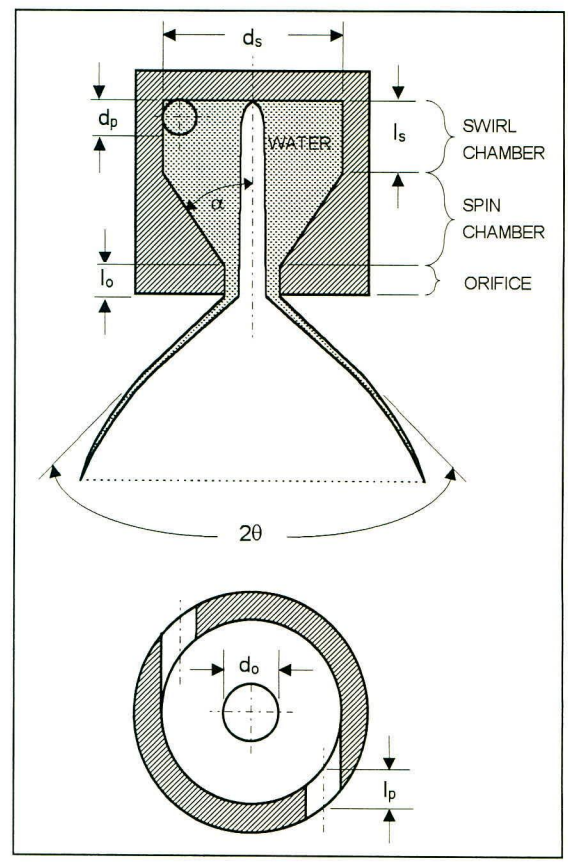

***Figure 2 - 1**: Sectional view of a swirl atomiser.*

Taylor [48TA1] made a simple analysis of the simplex swirl atomiser. His assumption of inviscid irrotational flow simplified the problem allowing him to use the Bernoulli equation in obtaining a solution. He proposes that the tangential velocity is inversely proportional to radius and that the constant of proportionality, Ω, the circulation constant, is dependent on the fluid entry conditions.

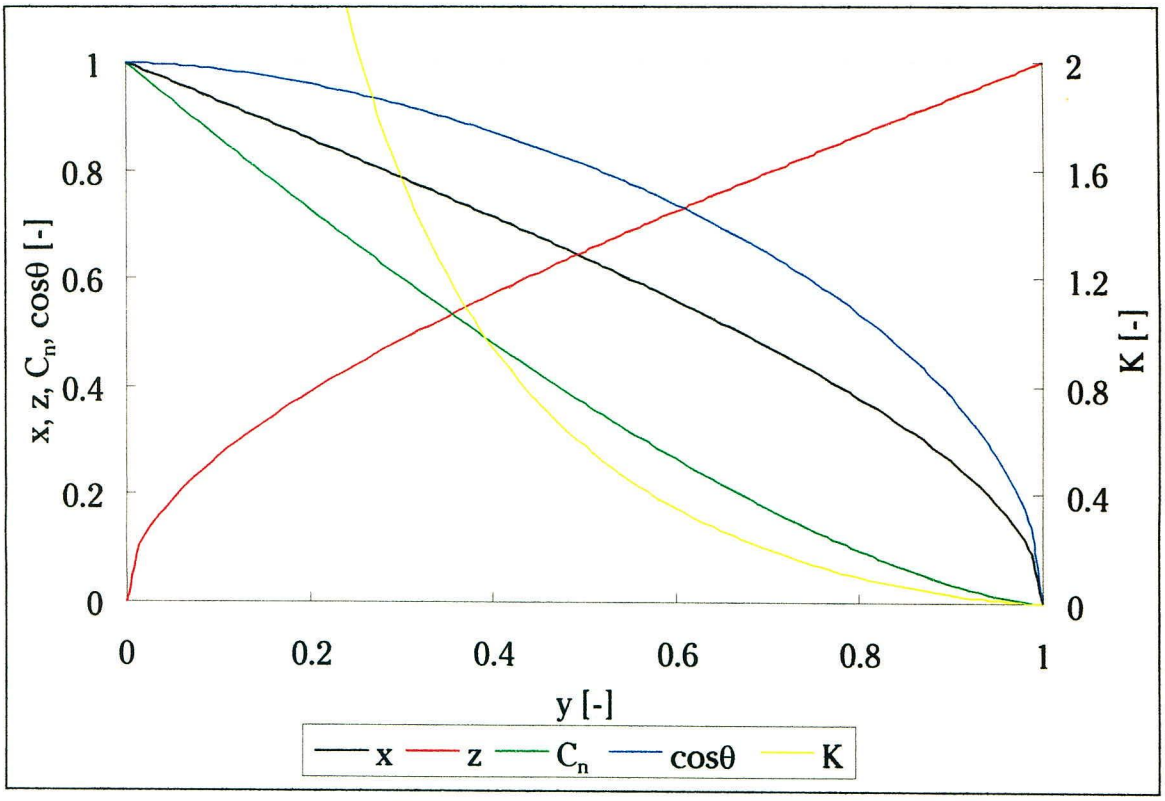

Figure 2 - 2: *Relationship between* K *and the flow variables of Taylor [48TA1].*

The results of his analysis are shown graphically in Figure 2-2. The variables depicted here include K, the nozzle parameter, x, the ratio of axial velocity within the orifice, v_o, to pressure velocity, U_p, z, the ratio of air-core radius to orifice radius and y, the nozzle constant. If either of the values of K or y are known for a particular HCN then this theory can be used to calculate the spray cone angle, 2θ and the nozzle discharge coefficient, C_n. Unfortunately this theory is not well suited for application to real fluids because of the presence of boundary layers which develop along the inside of the swirl chamber and within the orifice. He finally concludes his paper with the following sentence relating to the question of boundary layers; "For this reason perfect fluid theory has no application in the hydrodynamics of swirl atomisers."

In his next article Taylor [50TA1] examines the boundary layer which develops inside the conical spin chamber. He makes use of Pohlhausen's momentum integrals through the boundary layer in order to determine the velocity distribution and thickness of the boundary layer. Many authors have subsequently used the same approach to solve this unique problem. This analysis makes it possible to estimate the boundary layer thickness at the final orifice and

also determine the flow paths of the fluid in the boundary layer. Comparing the boundary layer thickness to the film thickness gives one an indication of the usefulness of the inviscid theory. According to Taylor [50TA1] "a condition can arise in which practically the whole of the outflow from the orifice is fed by a boundary layer current close to the surface of the swirl chamber." Chapter 3 contains a worked example, from this paper, which can be used to estimate the boundary layer thickness at the final orifice.

In their design of experimental swirl atomisers Dombrowski and Hasson [69DO1] recognised the importance of the ratio of swirl port length, l_p, to swirl port diameter, d_p. At low ratios the flow tends to diffuse from the port into the swirl chamber, while at higher values the frictional losses become too large. Results from their pilot experiments indicate an optimum value for l_p/d_p of 3. Their work was aimed at determining the effect of the variation of the ratios of swirl chamber diameter, d_s, to orifice diameter, d_o, and orifice length, l_o, to orifice diameter, d_o, on spray cone angle, 2θ, and nozzle discharge coefficient, C_n. Their results show that discharge coefficient is increased by an increase in d_s/d_o but decreases with increases in l_o/d_o. The spray cone angle is decreased when either of the two ratios is increased. A point of theoretical importance discovered by them is that for any given value of l_o/d_o a unique relationship exists between discharge coefficient and spray cone angle.

Som [83SO1] investigated the discharge coefficient and spray cone angle of the swirl pressure atomiser for a non-Newtonian fluid. His analysis pointed to the following as the independent control parameters;

- the generalised inlet Reynolds number, Re_{gi}, based on the tangential velocity at the nozzle inlet, the diameter of the swirl chamber and the apparent viscosity of the fluid
- the flow behaviour index number of the fluid, m
- the ratio of swirl chamber length to diameter, l_s/d_s
- the half spin chamber angle, α
- and the ratio of swirl chamber diameter to orifice diameter, d_s/d_o.

The results of his work reveal the dependence of discharge coefficient and spray cone angle on the generalised inlet Reynolds number and the flow behaviour index of the fluid. This dependence is especially significant at lower Reynolds numbers, i.e. $Re_{gi} < 60\,000$. The

relationships between the geometry of the nozzle and the spray characteristics are the same as that disclosed by Dombrowski and Hasson [69DO1] and Rizk and Lefebvre [85RI1].

Walzel [84WA1] discusses the various designs of single substance pressure atomisers and is particularly interested in their relevant sheet numbers. The sheet number is important for predicting drop formation and is the ratio of the product of the sheet length and thickness to the area of the final orifice. HCNs produce the smallest sheet numbers and thus generate the smallest drops, which makes them very attractive in industry. According to him larger spray angles can be generated either by increasing the swirl chamber diameter or by the addition of a rounded profile at the nozzle exit which deflects the streamlines thereby producing a larger spray angle. This phenomena of deflecting streamlines along a convex solid body is known as the Coanda effect, after the Rumanian aeronautical engineer Henri Coanda (1885 - 1972).

Walzel [84WA1] classifies the FCN as a turbulence nozzle, for which atomisation does not begin until a critical Weber number is exceeded. Drops form as a result of turbulence in the central jet, sheet break-up of the fluid annulus and also on account of the relative velocity between the water jet and annulus. FCNs serve for uniform spraying of large surfaces when small drops are not required. The FCN is the combination of a HCN and a jet atomiser, see Figure 2-3.

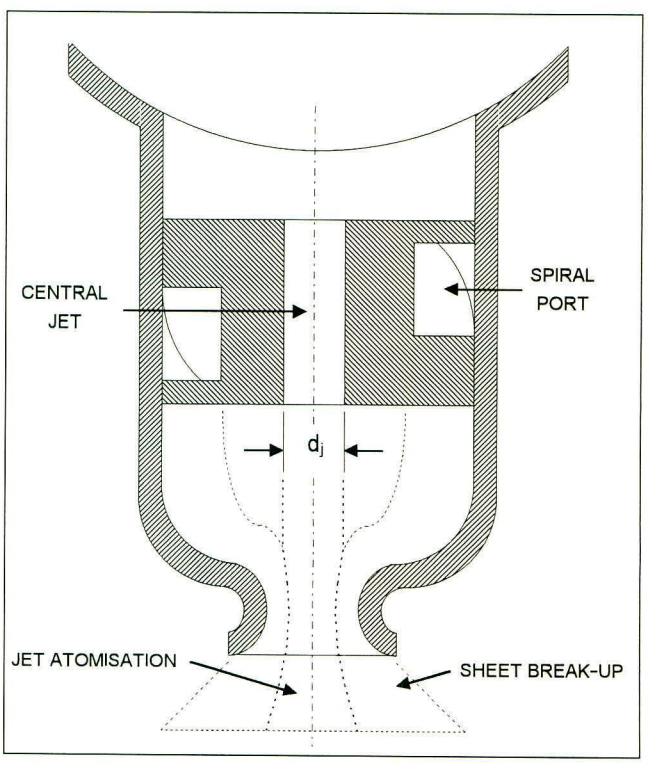

Figure 2 - 3: *Sectional view of a FCN.*

Rizk and Lefebvre [85RI1] analysed the simplex atomiser giving equations for flow number and discharge coefficient and also deriving a relatively simple equation for film thickness. Their findings concerning the effects of varying nozzle dimensions on nozzle flow characteristics can be summarised as follows:

- Film thickness increases with increases in swirl port area, A_p, orifice diameter, d_o and swirl chamber length, l_s, but decreases with increases in swirl chamber diameter, d_s, and orifice length, l_o.
- Flow number, FN, increases with increases in swirl port area, A_p, and orifice diameter, d_o, but decreases with increases in swirl chamber diameter, d_s. Flow number is not affected by changes in orifice length, l_o, and swirl chamber length, l_s.
- The variation of X, the ratio of air-core area to orifice area, is such that it increases when injection pressure, P_n, is increased but decreases when K, the nozzle parameter, is increased.
- Spray cone angle, 2θ, is increased when the ratio d_s/d_o is decreased.

Horvay and Leuckel [86HO1] made use of the Navier - Stokes equations in their analysis of swirl pressure nozzles. They derived theoretical equations for the spray cone angle, air-core radius, r_c, and the tangential, u_o, and axial, v_o, velocities at the nozzle exit. They also derived similar equations experimentally.

Prywer and Kulesza [87PR1] conducted experiments with full cone nozzles. They investigated the effect of the ratio of inlet port area to central jet area, A_p/A_j, on the uniformity of the spray distribution; best results were achieved with values of this ratio of about 4,3. This means that for a nozzle with four swirl ports the most uniform distribution can be expected when the ports and the central jet each comprise roughly twenty percent of the total flow area.

The most comprehensive source of nozzle information is Lefebvre's [89LE1] **Atomization and Sprays**. The sections relating to swirl atomisers incorporate nearly all of the information contained in this literature study, which makes a summary of this work redundant. This book is important reading for anyone interested in the field of fluid atomisers. Documented are all the effects of nozzle dimensions, fluid properties and operating conditions on spray characteristics such as discharge coefficient, patternation and atomisation.

Dahl and Muschelknautz [92DA1] made use of cyclone theory in their analysis of the HCN. The inclusion of a wall friction coefficient in their calculations makes it possible to determine both axial and tangential velocity at the nozzle exit and also the frictional pressure loss through the nozzle. They estimate that roughly 80 percent of the total pressure drop across a swirl

atomiser is used to accelerate the fluid, while the remainder is dissipated through wall friction. These figures are in agreement with data obtained in this thesis.

Chen et al. [93CH1] studied the circumferential liquid distribution of simplex atomisers. Uniformity in the context of this paper is a measure of the symmetry of the distribution. The most uniform distributions were obtained with nozzles having an orifice length to diameter ratio of between 1,5 and 2, although viscous fluids showed better uniformity at l_o/d_o equal to 0,5. The results also showed that spray uniformity was improved markedly at higher pressures. The number of inlet ports had little effect on the uniformity of distribution so long as the ports were spaced evenly around the entry to the swirl chamber.

Dumouchel et al. [93DU1] conducted a numerical analysis of the viscous flow in a swirl atomiser. The main input parameter for their computer program was a Reynolds number that is based on the inlet port diameter and the radial inlet velocity. The flow was simulated for Reynolds numbers less than 150, however it was found that for $Re \geq 100$ the velocity field was independent of Re. Their analysis focuses on determining the effects of varying nozzle geometry in order to predict the spray cone angle. They concluded that the characteristics of the conical sheet produced at the nozzle exit are indeed functions of nozzle geometry, a finding that is in agreement with experimental data.

Koo and Kuhlman [93KO1] developed a theoretical spray performance of swirl-type nozzles by solving boundary flows in the swirl chamber of the nozzle using the integral momentum method. Their investigation revealed the essential structures of the discharge coefficient and the swath coefficient, s, which is the ratio of height of the nozzle to the width of the spray and is an indication of the spread of the spray. They also define several parameters, which are different from those used by previous authors.

In their next paper, Koo and Kuhlman [93KO2] design, test and calibrate an experimental nozzle using the theoretical spray performance theory, which they had previously been developing. The results are characterised by two flow regimes, namely turbulent and laminar. This difference in flow was evident in the swath coefficient, which showed two completely separate but similar trends.

2.2 Water Distribution and Cooling Tower Performance

Kranc [83KR1] studied the effect of non-uniform water distribution on counterflow cooling tower performance. There are two factors which influence the cost of operation of a cooling tower: pumping head which is a function of the distribution system and the thermal performance which is a function of the packing geometry, water distribution and air-side pressure drop. Flooded areas represent excess pump work and reduced cooling due to minimised evaporation while dry areas correspond to under performance, even though lower water temperatures are achieved. The problem of flooding is compounded when the total flow rate is increased in order to improve coverage of dry areas. He uses the Merkel equation to compute the design performance of the tower. Performance of a tower with non-uniform water distribution is calculated relative to the same tower operating with a uniform water distribution. Results from this work show that some degree of non-uniformity can be tolerated within a tower without seriously affecting the thermal performance of that tower, while the negative effect of greater non-uniformities is evident.

Schultz [87SC1] investigated the effect of uneven water distribution on the performance of counterflow cooling towers. Having measured the actual distributions of existing nozzles, he then used this data in a computer simulation program to predict the cooling capacity of the tower. Results showed reductions in cooling tower performance of between 54 and 64 percent. These high estimates can be attributed to the simulation program neglecting the effects of redistribution of water by the fill pack and break-up of water in flooded regions of the tower by the counter flowing air.

Bellagamba et al. [88BE1] investigated the distribution of water in cooling towers by commercially available spray nozzles. Their focus is on low-pressure nozzles used in the distribution of water to splash packs in large natural draft cooling towers. Here distribution is a key element in the performance of the whole tower and in particular within the rain zone, which is the region between the splash pack and the nozzles. According to them tower performance is affected by uniformity of spray, air-side pressure drop and heat transfer occurring in the rain zone, which in turn is dependent on drop size.

Kranc [93KR1] presents a method for estimating the performance of a counterflow cooling tower with a regular fill. The model utilised is different from his previous work in that redistribution of water, due to interaction with the structured fill, is taken into account. Three models of water distribution through the tower are discussed in the paper. In the first instance the ideal case of uniform flow, the second an initially non-uniform distribution which persists throughout the tower, and finally an initially non-uniform distribution which is redistributed by the fill. Results of this analysis show that regions of non-uniformity persist for some depth into the tower and that performance is significantly degraded. The introduction of a redistributing fill is beneficial to tower performance.

2.3 Drop Size Distribution

Drop size distribution from HCNs is not actually within the scope of this thesis. It is only in large natural draught type cooling towers that the size of drops in the rain zone can affect overall tower performance. In smaller mechanical draught type cooling towers it is rather the rainfall intensity distribution, RID, that is important and not the drop size distribution. The following article, which concerns drop formation in FCNs, has been included to illustrate the relative complexity of this atomisation process.

Sada et al. [78SA1] conducted experimental work with FCNs in order to determine the relationship between drop size distribution and injection pressure. They found that the geometric mean diameter of drops decreased when injection pressure was increased, but that this was only significant at the centre of the spray. They also found that the drop size distribution varied widely with respect to position within the spray. At the centre of the spray the drop size distribution could be expressed as logarithmic normal, while at greater local radial positions the drop size distribution contained two peaks. The peaks are indicative of two mechanisms of drop formation – turbulence atomisation in the centre and sheet break-up at the perimeter. This double peak distribution is such that the geometric mean diameter for the first peak decreases as the radial distance from the spray centre increases while the logarithmic standard deviation for the second peak decreases with radial distance from the centre, this implies that the second peak becomes more acute at the environs of the spray.

2.4 Summary Conclusions

Cooling tower performance is dependent on uniform water distribution for optimum performance. This finding supports the motion to design more effective sprayers. Improved FCNs are the solution to the problem of uneven water distribution in cooling towers. Although there is an abundance of literature on the subject of HCNs, many of the experimental correlations are only valid for *small* high-pressure nozzles. Consequently it will be necessary to calibrate *large* HCNs at medium pressures so that accurate correlations can be obtained. The nozzle parameters that most affect the spray characteristics are; K, d_s/d_o, l_o/d_o and l_s/d_s. The effect of some form of Reynolds number, related to operating conditions, will have to be investigated because this effect is not evident with high-pressure nozzles.

2.5 Design Objectives for a Sound Nozzle

The type of nozzle developed here is designed for use in specific towers, for this reason the experimental test conditions were selected to approximate typical cooling tower conditions. There are many parameters which affect the spray characteristics of both hollow and full cone nozzles, however, an experimental investigation, more detailed than the one described within these pages, would only have complicated the design process without necessarily yielding a better solution.

Taking into account the ultimate goal for this project, i.e. to produce a practical cooling tower nozzle, it was necessary to limit the extent of the study of HCNs so that time could be more appropriately spent on investigating FCNs. However, since roughly 80 percent, following the advice of Prywer and Kulesza [87PR1], of the water flowing through a FCN is forced through the swirl ports, this water will behave within the nozzle primarily as though it were inside a HCN. Therefore, it is necessary to examine those specific HCNs from which the full cone cooling tower nozzles will assume their dimensions and many flow characteristics.

Restrictions on the operating conditions of cooling tower nozzles include; an installation height of between 17 cm and 40 cm above the cooling tower fill pack and an injection pressure of

between 25 kPa and 90 kPa. Operating pressure is an important consideration in mechanical draft cooling towers since if the pressure is too high tiny droplets may form and be drawn with the air stream out of the top of the tower without actually doing any cooling. A supply pressure of 35 kPa is adequate for sustaining the atomisation process without causing undue water loss.

Rainfall intensity, I, spray area and airflow rates are the three controllable variables affecting the thermal performance of cooling towers. The easiest variable to change in an existing tower is water flow rate, since packing is often standard and the airflow rate is coupled to the performance of the fan. Typical values for rainfall intensity of industrial type cooling towers are between 0,5 and 8 kg/m²s. The ideal result for this project would be to yield a formula for designing nozzles for specific rainfall intensities.

Finally the crux of this thesis; "What is required from a cooling tower nozzle?" In point form the prerequisites of a good nozzle design are:

- uniform distribution in a *square* spray pattern
- no clogging under normal operating conditions
- minimal pressure losses
- predictable characteristics for design purposes
- simplicity of design and ease of manufacture
- competitive low cost production.

CHAPTER THREE

THEORETICAL TREATMENT

3.1 The Swirler

In order to predict the flow rate through the swirler it is necessary to estimate the pressure loss coefficient. Approximate analyses of the geometry of the two swirlers will clearly outline the advantages of streamlining the swirl ports. Figure 3-1 illustrates the two basic swirl port geometries.

There are three features of the sharp swirler, which will result in significant pressure losses namely, the sudden contraction, the protruding sharp lip, which may also cause flow separation within the swirl port, and the change in flow direction. The streamlined swirler will have smaller entry losses, no separation and smaller losses from the gradual directional change. However, frictional losses may well be greater than those of the sharp swirler because of the increased port surface area.

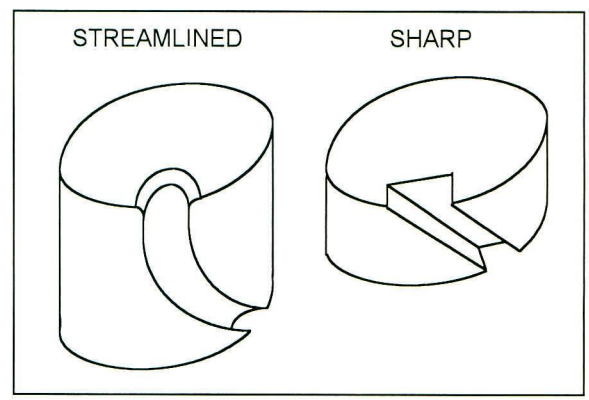

Figure 3 - 1: *Swirl port geometries.*

Neglecting gravitational acceleration the following energy balance equation expressed in terms of pressure and pressure losses describes the flow through a swirl port:

$$P_n = P_1 + \tfrac{1}{2}\rho U_1^{\,2} = P_2 + \tfrac{1}{2}\rho U_e^{\,2}\left[\sum F_i + 1\right] \qquad (3\text{-}1)$$

where the subscripts 1 and 2 indicate static pressure upstream and downstream of the swirler and the F_i's are the individual dynamic head loss coefficients. The loss coefficient due to sudden contraction, F_{sc}, can be approximated with the following equation derived from White's [86WH1] empirical formula for flow losses due to sudden contraction in a pipe:

$$F_{sc} \approx 0{,}42\left(1 - \frac{d_1^{\,2}}{d_2^{\,2}}\right),$$

where by substituting port area, A_p, for $d_1^{\,2}$ and swirler area, A_s, for $d_2^{\,2}$ we obtain:

$$F_{sc} \approx 0{,}42\left(1-\frac{A_p}{A_s}\right). \qquad (3\text{-}2)$$

This equation can be used to estimate the entry loss coefficient for the sharp swirler. Based on the ratio of the swirl port area, A_p = 932 mm^2, to the swirl chamber area, A_s = 3664 mm^2, this equation yields a loss coefficient of 0,31. The values given above are the actual flow areas of the two tested swirlers. For well-rounded entrances, such as those found in the streamlined swirler, White [86WH1] suggests that the loss coefficient could be in the region of 0,05.

The next loss coefficient to be estimated is for the overhanging sharp lip. In the absence of any other significant data and as a crude approximation for this loss coefficient it was decided to model this geometry as a three-quarters-open gate valve. The loss coefficient could then be taken from Appendix C of Foust et al. [60FO1]. The equivalent length in pipe diameters of a three-quarters-open gate valve is 35. For a schedule 40 pipe with inside diameter of 19 mm (0,75 inches) this is equivalent to a loss coefficient of 0,85, which if nothing else at least gives an estimate for the magnitude of the losses associated with the overhanging lip of the sharp-edged swirler.

The third loss coefficient for both swirlers, taken from Appendix C of Foust et al. [60FO1], is that of a 45° standard elbow, which has an equivalent length in pipe diameters of 16, or a loss coefficient of 0,35. This coefficient can be used to estimate the losses due to the directional change in the liquid brought about by the individual swirl ports. By summing up all these individual loss coefficients, we are now in a position to predict the total loss coefficient for each of the two swirlers.

For the sharp swirler:

$\Sigma F_i = 0{,}31 + 0{,}85 + 0{,}35$

$= 1{,}51.$

For the streamlined swirler:

$\Sigma F_i = 0{,}05 + 0{,}35$

$= 0{,}4.$

Rearranging Equation (3-1) gives the unknown port velocity, U_e:

$$U_e = \sqrt{\frac{2\Delta P_{sw}}{\rho \times \left[\Sigma F_i + 1\right]}}, \qquad (3\text{-}3)$$

where ΔP_{sw} is the pressure drop across the swirler.

Substituting for the two loss coefficients yields:

for the sharp swirler:

$$U_e = 0{,}631\sqrt{\frac{2\Delta P_{sw}}{\rho}}$$

and for the streamlined swirler:

$$U_e = 0{,}845\sqrt{\frac{2\Delta P_{sw}}{\rho}}.$$

From this estimation of the two loss coefficients it is expected that the fluid velocity through the streamlined swirler will be 33,9 percent greater than through the ports of the sharp swirler. Alternatively, if these swirlers were to operate at the same flow rate, i.e. port exit velocities equal, then the pressure drop across the streamlined swirler would be 44,2 percent less than the pressure drop across the sharp swirler.

3.2 The Hollow Cone Nozzle

The following sections describe some of the theories and relevant formulas pertaining to swirl-pressure atomisers. The idea here is not to make a complete analysis of the HCN but rather to select from the literature those calculation methods that can be readily applied in predicting the spray characteristics of simplex atomisers.

3.2.1 Spray Cone Angle

The spray cone angle is defined as the angle between the tangents to the spray envelope at the nozzle exit. Neglecting radial velocity, which is an order of magnitude less than the tangential and axial velocities, the spray cone angle is usually expressed as:

$$\theta = \cos^{-1}\left(\frac{\bar{v}}{U_a}\right) \tag{3-4}$$

where U_a is the total velocity of the spray sheet and $\bar{v}$ is the mean axial velocity of the liquid leaving the nozzle.

The first estimate of θ comes from Taylor [48TA1]. The equation for $\cos\theta$ is depicted graphically in Figure 2-2 but is reproduced here for clarity:

$$\cos\theta = x + \frac{y\sqrt{2}z^2}{\left(1-z^2\right)^{\frac{3}{2}}}\left[\frac{1}{2}\left(\frac{1}{z^2}-1\right)+\log_e z\right]. \tag{3-5}$$

The relationship between the variables comes from the Bernoulli equation at the core, which can be written in the form

$$1 = x^2 + \frac{y^2}{z^2} \tag{3-6}$$

here $z = \frac{r_c}{r_o}$ and r_c is the radius of the air-core within the orifice,

$x = \frac{v_o}{U_p}$, v_o being the axial velocity in the orifice and U_p the so called pressure velocity which is defined thus:

$$U_p = \sqrt{\frac{2\Delta P_n}{\rho}} \text{ and finally}$$

$$y = \frac{\Omega}{r_o U_p}.$$

The equation for z in terms of y is:

$$z^2 = \frac{y^2}{4} + \sqrt{\frac{y^4}{16} + \frac{y^2}{2}}, \tag{3-7}$$

which is derived through the continuity equation. The nozzle parameter, K is related to y and the nozzle discharge coefficient, C_n by the following formula:

$$K = \frac{\pi C_n}{4y}. \tag{3-8}$$

The cyclone theory of Dahl and Muschelknautz [92DA1] provides a practical method for determining the axial and tangential velocity components, immediately before and after the final orifice. From these velocities the other discharge characteristics such as spray angle are easily determined. The first equation they give is that of tangential velocity within the orifice:

$$w_o = \frac{U_e \frac{r_e}{r_o}}{1 + \frac{\lambda}{2} \frac{A_R U_e}{\dot{q}} \sqrt{\frac{r_e}{r_o}}}. \tag{3-9}$$

A_R is the frictional area of the swirl ports and swirl chamber combined and λ is the wall friction coefficient dependent on the mean nozzle Reynolds number. The Reynolds number is defined thus:

$$Re_m = \frac{\rho w_m r_m}{\mu}. \tag{3-10}$$

Dahl and Muschelknautz [92DA1] provide a graph, somewhat like a Moody diagram, for estimating λ. For Reynolds numbers between 100 000 and 300 000 λ varies between 0,007 and 0,003 and has a near linear relationship with Re_m on the log-log scale. According to Dahl and Muschelknautz [92DA1] the axial velocity in the outlet depends on the centrifugal forces of the rotational flow. Under the influence of friction, they give the tangential velocity profile as:

$$vr^n = \text{const.}$$

Therefore, by integrating this profile and equating the static pressure near the air core to zero, the following relationship between dimensionless tangential and axial velocity within the orifice is found.

$$W_o^{\,2} = 2V_o \frac{(V_o - 1)^{n+1}}{V_o^{\,n-1}} \tag{3-11}$$

with

$$W = \frac{w}{U_o}, \tag{3-12}$$

$$V = \frac{v}{U_o} \tag{3-13}$$

and

$$U_o = \frac{\dot{q}}{\pi r_o^{\,2}}. \tag{3-14}$$

When leaving the nozzle the liquid near the wall of the orifice accelerates in the direction of the static pressure gradient, while the liquid near the air core is at ambient static pressure and therefore does not accelerate. By integration of the radial pressure gradient within the orifice and conversion to dimensionless form the liquid velocity after leaving the nozzle can be calculated as:

$$V_a^{\,2} = V_o^{\,2} + \frac{1}{n} W_o^{\,2} \left[\left(\frac{V_o}{V_o - 1} \right)^n - 1 \right]. \tag{3-15}$$

The dimensionless mean axial velocity past the outlet of the nozzle is then the root mean square of V_o and V_a:

$$\overline{V} = \sqrt{\frac{V_o^{\,2} + V_a^{\,2}}{2}}. \tag{3-16}$$

The film thickness in the final orifice is calculated from the continuity equation:

$$t = r_o - \sqrt{r_o^2 - \frac{\dot{q}}{\pi v_o}}. \tag{3-17}$$

Finally the total velocity of the liquid sheet past the nozzle can be calculated by vectorial addition of the tangential and axial velocity components:

$$U_a = \sqrt{\bar{v}^2 + w_o^2 \left(\frac{r_o}{r_o - t}\right)^n}. \tag{3-18}$$

The spray cone angle can now be calculated from Equation (3-4):

$$\theta = \cos^{-1}\left(\frac{\bar{v}}{U_a}\right). \tag{3-19}$$

Som [83SO1] provides an equation for spray cone angle. The numerical values in the equation have been evaluated from experimental results even though the form of the equation was derived theoretically using the Pohlhausen momentum integral method. The equation is:

$$\theta = \frac{77{,}260\left(d_o/l_s\right)^{0{,}3153}(2\alpha)^{0{,}1949}}{\left(l_s/d_s\right)^{0{,}0611}}\left[1 - e^{\left(-8{,}695\times10^{-5}\right)Re_{gi}}\right], \tag{3-20}$$

where Re_{gi} is the generalised inlet Reynolds number based on the tangential inlet velocity and swirl chamber diameter.

3.2.2 Discharge Coefficient

The discharge coefficient based on mass flow of a simplex atomiser is defined as the ratio of actual flow rate to theoretical maximum flow rate through the final orifice. In equation form:

$$C_n = \frac{\dot{m}}{\dot{m}_{max}}, \tag{3-21}$$

where

$$\dot{m}_{max} = \rho A_o U_p \tag{3-22}$$

$$\therefore C_n = \frac{\dot{m}}{\rho A_o \left(\frac{2\Delta P_n}{\rho}\right)^{0,5}}. \tag{3-23}$$

Numerous formulas have been proposed for the prediction of discharge coefficient of HCNs. The equations that follow are some of the more practical formulas found in the literature. The first equation is from Taylor's [48TA1] inviscid analysis of the HCN:

$$C_n = \left(1 - z^2\right)\left(1 - \frac{y^2}{z^2}\right)^{0,5} . \qquad (3\text{-}24)$$

Jones [82JO1] provides an empirical equation containing all the key nozzle dimensions:

$$C_n = 0,45\left(\frac{\rho U_p d_o}{\mu}\right)^{-0,02}\left(\frac{l_o}{d_o}\right)^{-0,03}\left(\frac{l_s}{d_s}\right)^{0,05} K^{0,52}\left(\frac{d_s}{d_o}\right)^{0,23} . \qquad (3\text{-}25)$$

Som [83SO1] derived the basic form of his equation analytically and then adjusted the constants and exponents according to experimental data:

$$C_n = \frac{3,377(n)^{1,520}\left(l_s/d_s\right)^{0,117}}{\left(Re_{gi}\right)^{0,347}\left(d_o/d_s\right)^{1,166}(2\alpha)^{0,274}} . \qquad (3\text{-}26)$$

By far the simplest and potentially most accurate equation for discharge coefficient is from Rizk and Lefebvre [85RI1]:

$$C_n = 0,35K^{0,5}\left(d_s/d_o\right)^{0,25} . \qquad (3\text{-}27)$$

3.2.3 Film Thickness

Taylor's [48TA1] analysis lead to an equation for z, Equation (3-7). This equation leads directly to the film thickness. Due to the nature of the equations it is impossible to obtain an explicit formula for z in terms of K. However, if K is known then z can either be read off Figure 2-2 or solved iteratively:

$$t = r_o(1 - z) . \qquad (3\text{-}28)$$

On the topic of film thickness, now is the time to investigate the paper of Taylor [50TA1], which deals with the question of boundary layer thickness. What follows is a short sample calculation in which the boundary layer thickness in the final orifice is estimated for a nozzle with $r_s = 34$ mm, $r_o = 16$ mm and $\Delta P_n = 28$ kPa.

$$U_p = \sqrt{\frac{2 \times 28\,000}{998}}$$
$$= 7,483\,\text{m/s}.$$

From Table 1 in Taylor [50TA1] take $R_1 = \frac{r_o}{r_s}$ and read off δ_1:

$$R_1 = \frac{16}{34} = 0{,}47$$
$$\therefore \delta_1 = 2{,}58.$$

The boundary layer thickness is:

$$\frac{\delta}{r_o} = \frac{\delta_1}{R_1 \sin\alpha}\sqrt{\frac{\nu \sin\alpha}{\Omega}} \qquad (3\text{-}29)$$

but since Ω is less than $r_o U_p$

$$\frac{\delta}{r_o} \geq \frac{\delta_1}{R_1}\sqrt{\frac{\nu}{r_o U_p \sin\alpha}}. \qquad (3\text{-}30)$$

Therefore, substituting in the known values with $\alpha = 90°$

$$\frac{\delta}{r_o} \geq \frac{2{,}58}{0{,}47}\sqrt{\frac{1\times10^{-6}}{0{,}016 \times 7{,}483 \times \sin 90^\circ}}$$
$$= 0{,}0159.$$

In this case, therefore, the boundary layer only extends inwards to a distance of one-sixtieth the radius of the orifice, or in physical measurement only 0,25 mm. For the same nozzle the film thickness, t, in the final orifice could be expected to be around 4 mm. Therefore it would seem from this example that the boundary layer in the final orifice could be ignored in a theoretical analysis of the swirl pressure atomiser.

Another equation for film thickness, which was seen earlier, is that of Dahl and Muschelknautz [92DA1]. We record it here again for convenience:

$$t = r_o - \sqrt{r_o^2 - \frac{\dot{q}}{\pi v_o}}. \qquad (3\text{-}31)$$

Two more equations for film thickness from Rizk and Lefebvre [85RI1] round off this chapter on the theoretical analysis of simplex atomisers. The first equation, which follows from a fairly complex derivation, is implicit and therefore needs to be solved through iteration:

$$t^2 = \frac{1560 FN\mu}{\sqrt{\rho \Delta P_n}\, d_o}\frac{1+X}{(1-X)^2}. \qquad (3\text{-}32)$$

The coefficient, 1560, is dependent on the flow path of the liquid in the swirl chamber and on the pressure drop across the final orifice – here it was derived from experimental data. The

second equation is appreciably simpler than Equation (3-32) while still retaining all the key parameters that have been shown to influence film thickness:

$$t = 3{,}66\left[\frac{d_o FN\mu}{\sqrt{\rho \Delta P_n}}\right]^{0{,}25} . \qquad (3\text{-}33)$$

The flow number which is not a dimensionless number, but which rather has the units of length squared, is defined thus:

$$FN = \frac{\dot{m}}{\sqrt{\rho\, \Delta P_n}} . \qquad (3\text{-}34)$$

CHAPTER FOUR

APPARATUS AND TEST PROCEDURE

From the literature study it became apparent that contemporary swirl atomiser theory would not be directly applicable to the question of analysing and predicting medium pressure nozzle characteristics. In pursuit of some mathematical model for medium pressure nozzles it was, therefore, necessary to gather experimental data through testing of prototype nozzles. In this chapter the experimental techniques and the physical apparatus used in the project are discussed.

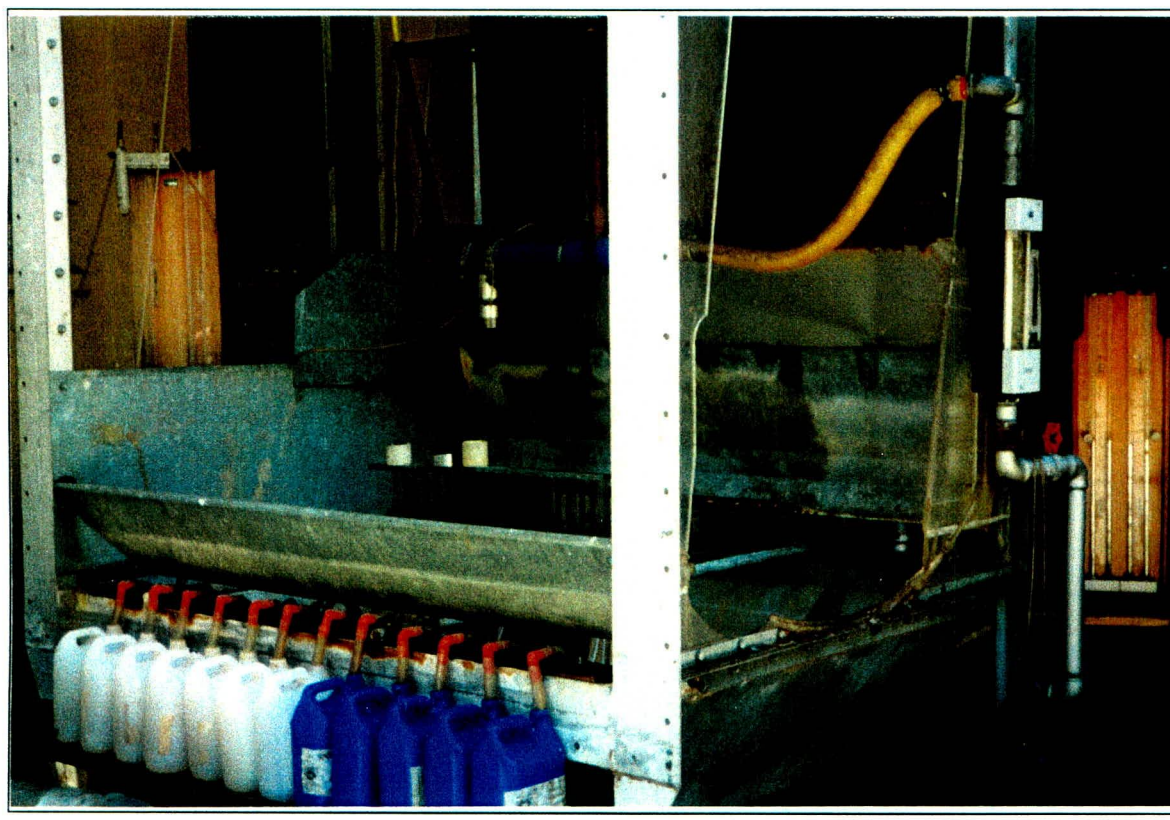

Figure 4 - 1: *Photograph of test rig.*

The main test facility, see Figure 4-1, was originally designed and built by Lake [93LA1] for an undergraduate thesis in which he measured the rainfall distribution of several commercially available FCNs. The variable nozzle, see Figure 4-3, which was also designed and built by him allows nozzle components to be easily changed between tests. PVC components are placed inside the main housing together with the necessary spacers so that the various parameters affecting distribution might be investigated. His work, which involved much experimental

testing, showed that the water distribution from commercial nozzles was often not uniform and this finding prompted the present investigation.

4.1 Test Facility

In this section the operation of the test facility is discussed while mention is made of the various components and flow metering devices. Figure 4-2 shows all the essential elements of the test facility. Water is supplied to the nozzle by pumps which draw their water from an underground reservoir. Test conditions are controlled by manipulating the control valve and the by-pass valve. The flow rate is measured by means of a mercury manometer coupled to an orifice plate which was designed, manufactured and installed in accordance with BS 1042. The orifice plate has D and ½D taps and has plate has a diameter ratio, β, of 0,68 with the supply pipe which has an inside diameter of 50 mm. The nozzle supply pressure is measured with a mercury manometer, the open end of which is connected to a reservoir with a large surface area, the surface of which can be positioned horizontal to the nozzle pressure tapping, thereby negating the need for a *zero* reading during testing.

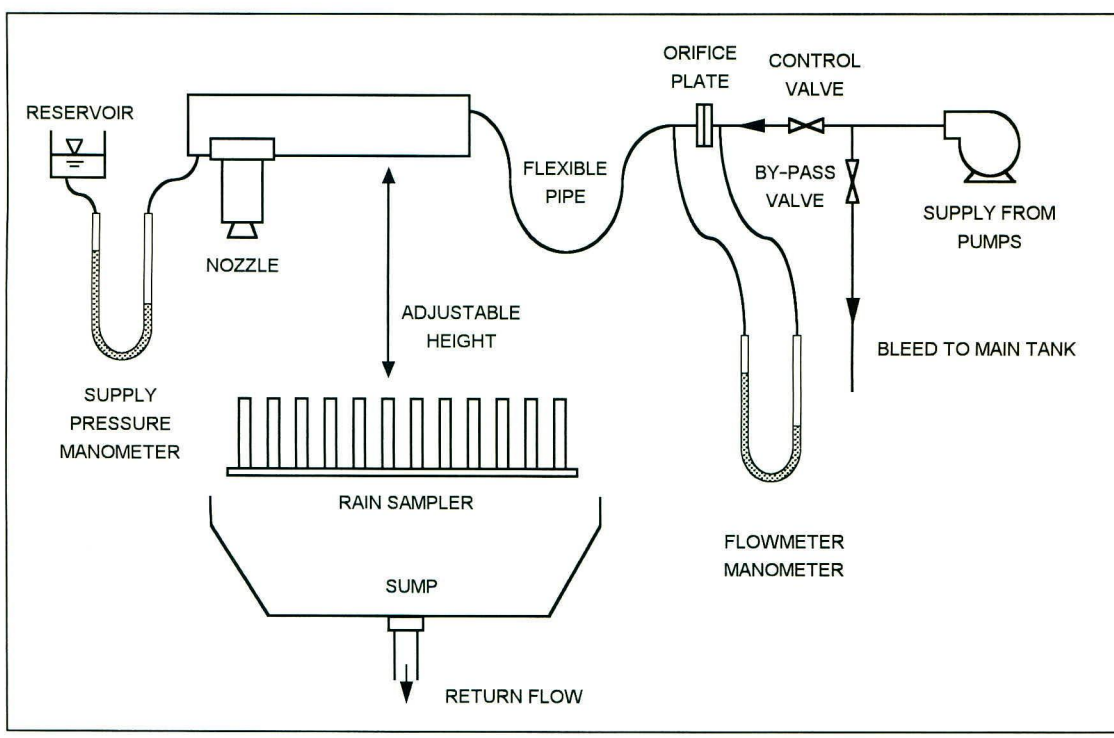

Figure 4 - 2: *Layout of test facility.*

Figure 4-1 is a photograph of the test rig. The rotameter visible on the right of the photograph can only be used to measure flow rates less than 3,5 kg/s and was not used during the course of these experiments. The rain sampler, another of Lake's [93LA1] designs, is an array of 45 mm diameter cylinders, vertically aligned and equi-spaced at 8 cm intervals, see Figure 4-9. He originally used the sampler to measure distribution in a polar co-ordinate system, however, it was found to be more convenient to obtain rainfall intensity distribution, RID, data in a Cartesian co-ordinate system. Consequently modifications were made to the test facility to enable collection rainfall intensity data in this format. One quadrant of the spray is sampled, which is sufficient to characterise the particular spray distribution. A flexible plastic pipe between the nozzle and the rest of the pipe network allows for easy adjustment of the nozzle installation height, h.

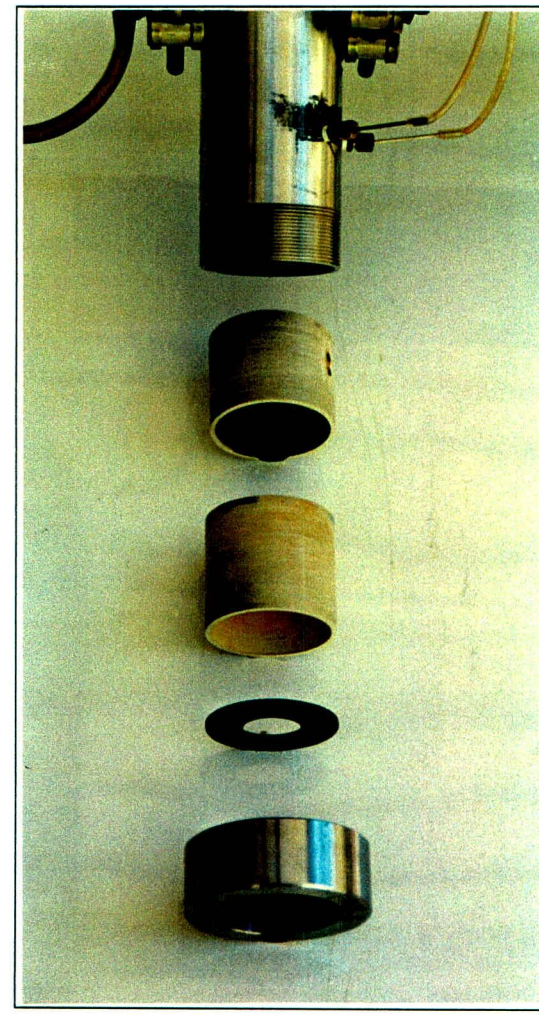

Figure 4 - 4: *Prototype nozzle.*

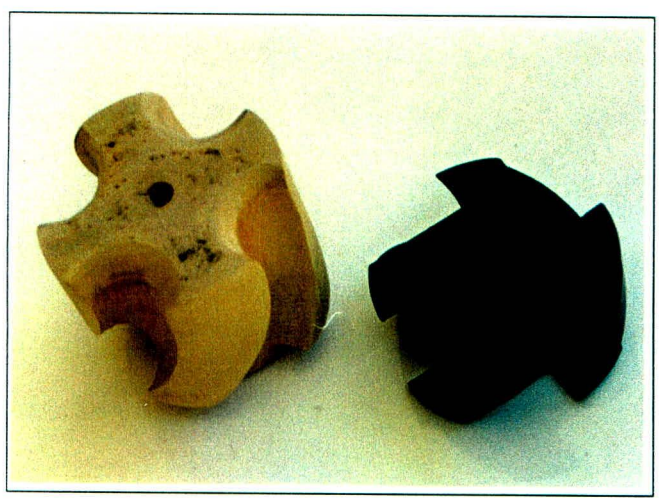

Figure 4 - 3: *Photograph of tested swirlers.*

After passing through the nozzle and over the rain sampler, the water is collected in the sump from where it then drains back into the underground reservoir. The inlet water temperature was measured with an alcohol thermometer.

4.2 Prototype Nozzle

The most striking internal feature of the HCN is the swirler. Most HCNs make use of tangential inlet ports, which means that the axial velocity component is almost nil at the top of the swirl chamber. HCNs however, usually make use of spiral inlets, which are produced by cutting helical grooves through the central core. Preliminary tests on a reproduction of a commercially available swirler showed significant pressure losses across the swirler. Therefore, it was decided to design a streamlined swirler. Figure 4-3 shows a prototype nozzle with all its appendages ready for assembly. The nozzle is assembled within the stainless steel housing by compressing the various components together between a stopper rim, in the top of the housing, and the threaded end cap. The tested swirlers can be seen in Figure 4-4. The object on the left is a wooden model of the streamlined swirler while on the right is the plastic model of a commercial type swirler.

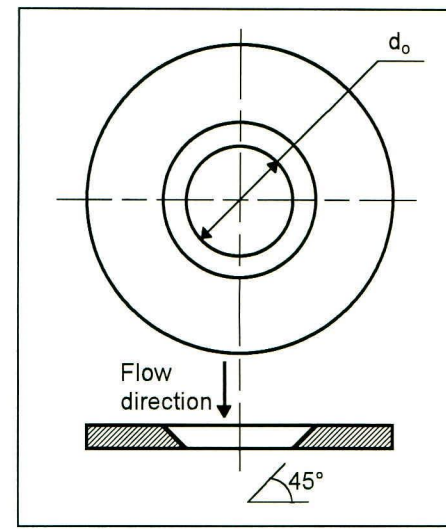

Figure 4-5: *Sharp-edged orifice.*

Most of the experimental work was carried out with nozzles using a sharp-edged orifice of the type depicted in Figure 4-5. The six sharp-edged orifices manufactured had the following diameters: 21,6 mm, 29,9 mm, 32,4 mm, 37,2 mm, 42,3 mm and 45,6 mm.

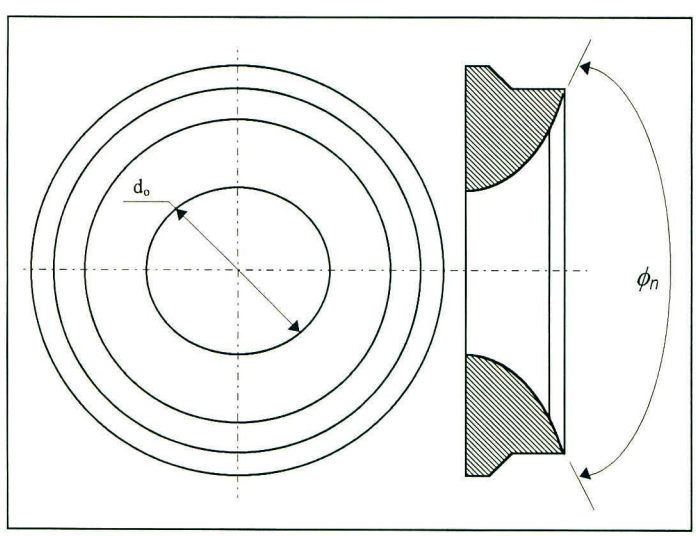

Figure 4 - 6: *Rounded nozzle exit.*

Figure 4-6 shows a typical rounded exit that was used to investigate the Coanda effect. Three of this type of exit were manufactured, all having a throat diameter, d_o, of 37,2 mm but having exit angles, ϕ_n, of 90°, 110° and 130°. The Coanda effect was investigated by measuring the change in spray cone angle that resulted from the use of the rounded exit profiles as

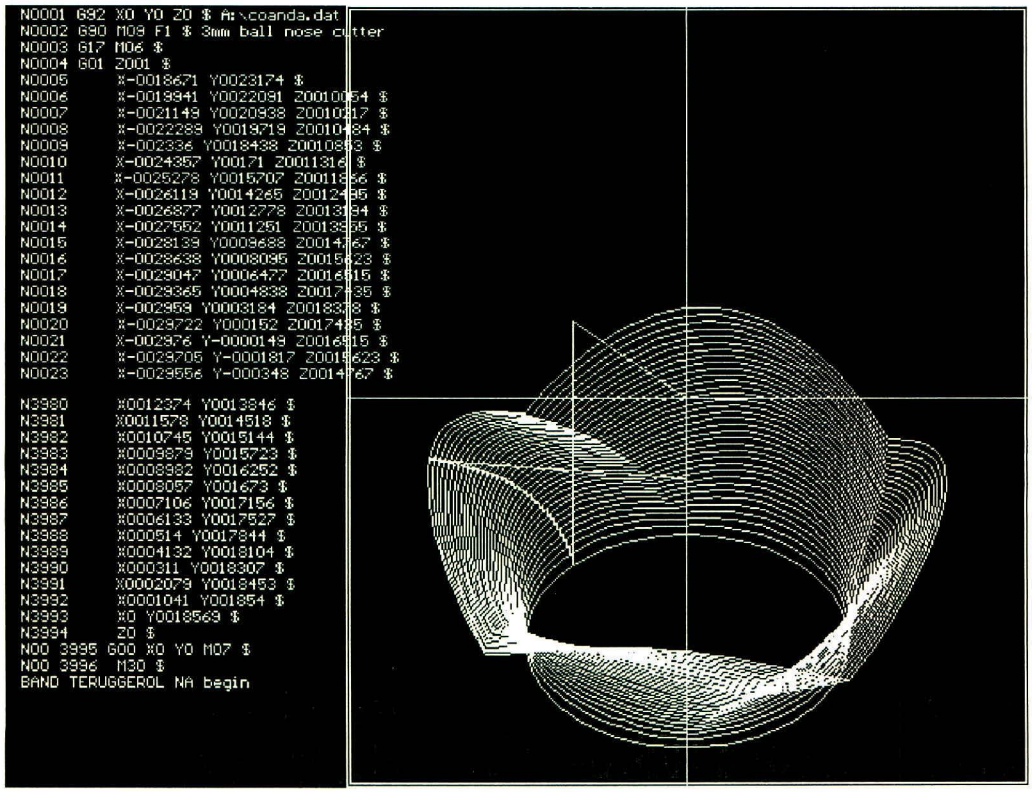

Figure 4 - 7: *Isometric view of cutter path for machining profiled outlet.*

compared to the spray cone angle generated by the equivalent sharp-edged orifice. Figure 4-7 shows the result of a simulation of the NC codes for cutting the prototype profiled exit. A mathematical description of the profile is given in Appendix D.

The streamlined swirler has a central cavity in which the central jet of the FCN is positioned, there is also a solid plug which was used to seal off the cavity in the event of HCN testing. Figure 4-7 shows the central jet located inside the swirler. The diameter, d_j, and protrusion length, l_j, of the central jet can be adjusted by inter-changing the lower inserts, which fit firmly into the main sleeve. Eight lower inserts were manufactured with the following jet diameters, d_j: 12,5 mm, 13,25 mm, 14 mm, 15 mm, 15,5 mm, 16 mm, 17 mm and 18 mm. A diffuser type central jet was also built and tested. This jet had a 12 mm inlet diameter and a 17 mm outlet diameter and was machined out to a linear 6° taper.

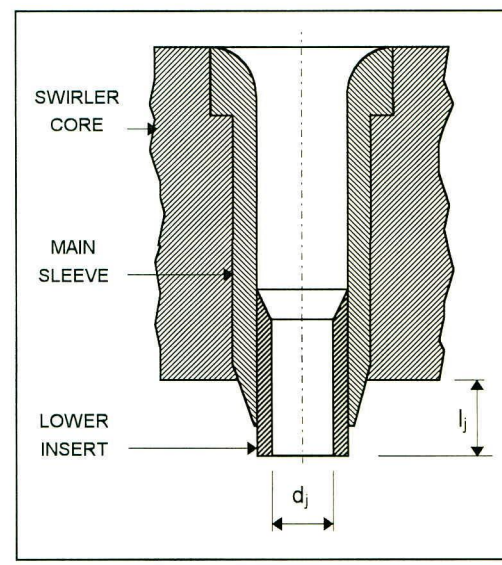

Figure 4 - 8: *Central jet.*

4.3 Measurement of Characteristics

The following paragraphs describe the various methods employed in obtaining nozzle characteristic data. Some of the methods are unorthodox but still effective under the circumstances. For example, it was initially expected that the film thickness probe would precisely indicate the interface between the air-core and liquid annulus meet within the orifice. However, after readings had been taken, the exact position was difficult to locate due to the insensitivity of the mercury manometer to the small pressures present in the water near the inner surface of the annulus. This procedure did however, provide informative graphs of the axial velocity profiles within the orifice.

4.3.1 Spray Cone Angle

A fundamental characteristic of the HCN that requires measuring is the spray cone angle, 2θ. The angle in question is subtended by the tangents to the un-atomised liquid sheet and only exists for a short distance beyond the final orifice. The task of measuring this angle is, therefore, more perplexing than it might seem. Previous workers have made use of the method of shadow graphing to record spray angles, however, this technique is ineffective for thicker spray sheets generated by medium pressure swirl atomisers.

In this project two methods were employed to measure the spray cone angle. The first method involved measuring the angle with a pair of dividers and protractor, and was used in pilot experiments to verify the claim that spray angle is independent of injection pressure. The second method was photographic and involved using a camera, mounted with lens perpendicular to the axis of the nozzle and parallel to the plane of the orifice, to photograph the spray so that the spray cone angle could then be measured with a protractor.

4.3.2 Film Thickness

The film thickness within the orifice was measured with the aid of a small probe mounted on a traverse, see Figure 4-8. The probe consists of a thin pointed tube, with an inlet diameter of

0,3 mm, connected to a mercury manometer. Since the probe is located at the nozzle exit the static pressure of the water is assumed to be zero. This means that the pressure reading on the manometer is the fluid dynamic pressure, $\frac{1}{2}\rho v_o^2$, and can be used to calculate the axial velocity.

The film thickness can be calculated indirectly from the axial velocity profile or, directly determined during the experiment as the point where the manometer reading becomes zero. To measure the axial velocity profile the probe is moved incrementally across the nozzle exit while the manometer readings are recorded at each increment. It is from these values that the axial velocities are calculated. The film thickness is now the value of the radius at which the axial velocity becomes equal to zero.

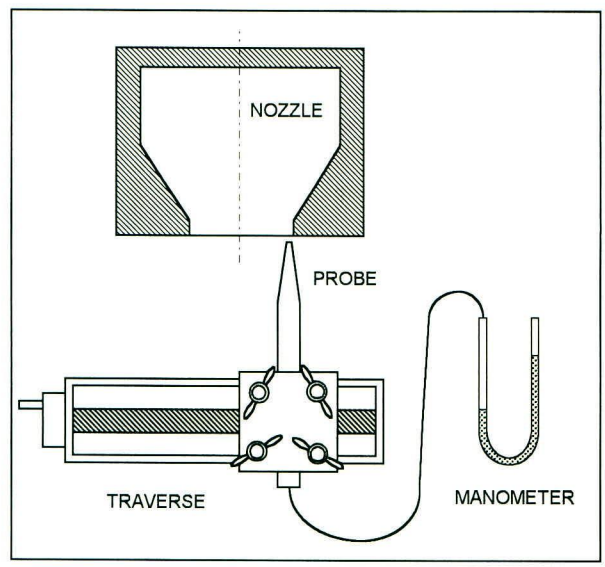

Figure 4 - 9: *Axial velocity probe.*

A photographic method was also implemented to measure the film thickness. This was done by placing the camera directly below the centre of the nozzle. The camera was isolated from the spray by a clear perspex sheet placed just above the lens. A macro lens was used so that the photographs taken would have a narrow focal depth and therefore sharply focused on the annulus of fluid within the orifice. A calibration photograph was also taken of the orifice, before the water supply was turned on, so that the measurements taken from the photographs could be accurately scaled. A spotlight reflecting off a parabolic mirror, below the camera, provided sufficient lighting for the photographs. The air-core diameter was then measured to scale off these photographs and the film thickness calculated accordingly. A sample photograph can be seen in Chapter 5.

4.3.3 Spray Distribution

The specific apparatus needed to measure a spray distribution are the rain sampler connected to collecting troughs, in this case 5ℓ plastic bottles were used, a scale to weigh each bottle and a stopwatch. A test is conducted at a pre-selected pressure with the nozzle positioned at a specified height above the sampler. Before commencing a test all the troughs and bottles are emptied and a cover is placed over the rain sampler. Now the water supply is turned on and the valves are adjusted until the desired pressure registers on the manometer. When the flow has stabilised the stopwatch is started and simultaneously the rain sampler cover is removed. The length of time required to fill one 5ℓ bottle is dependent on the specific local flow rates at each sampler. Fortunately the water inside the 5ℓ bottles is visible through the plastic, which simplifies the task of deciding when to stop the test, and also gives a good visual indication of the uniformity of the distribution.

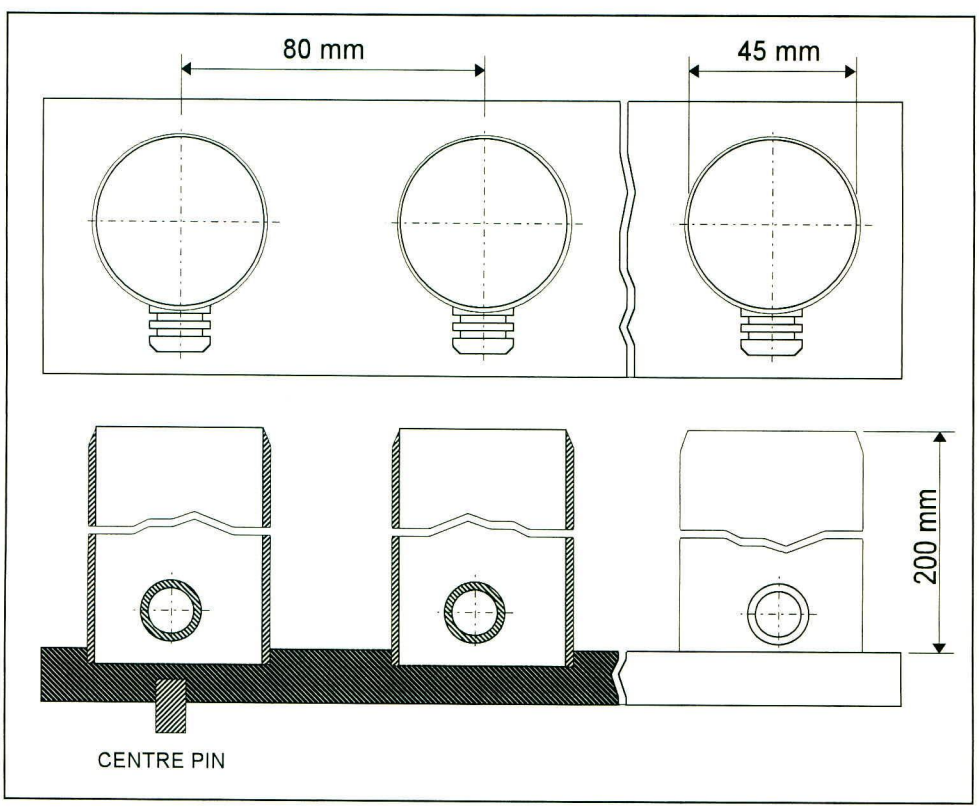

Figure 4 - 10: *Rain sampler.*

The test is completed by replacing the cover on the rain sampler and recording the duration of the test. The rainfall intensity is calculated from the mass of water collected in each sampler, the duration of the test and the inlet area of the sampler. In the case of an asymmetric nozzle, i.e. one producing a *square* pattern, the above process is repeated several times. For each new set of readings the rain sampler is brought forward, parallel to the previous position, until the rainfall intensity has been recorded for the entire wetted area beneath the nozzle. With the aid of a spreadsheet program the results can then be displayed either as three dimensional relief plots or as contour plots of the rainfall intensity, see Chapter 5 for characteristic samples.

CHAPTER FIVE

EXPERIMENTAL WORK

5.1 The Swirler

The main objective for testing the two swirlers was to evaluate the theoretical analysis of each swirl port geometry, which was done with loss coefficients in Chapter 3. The swirler configuration for these tests is shown in Figure 5-1. This configuration ensures that the swirler being tested will discharge at atmospheric pressure so that the pressure drop across the swirler can be exactly calculated. The swirlers are tested at a range of pressures while the corresponding flow rates are calculated from the pressure drop across the orifice plate. The results of these experiments are shown graphically in Figure 5-2 and Figure 5-3 where the actual port velocity is calculated from the continuity equation. An example of how the actual velocities and loss coefficients are calculated is given in Appendix B.

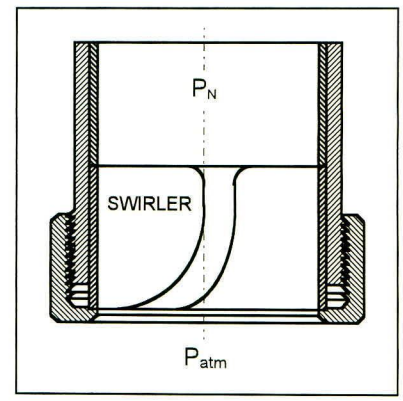

Figure 5 - 1: *Swirler test configuration.*

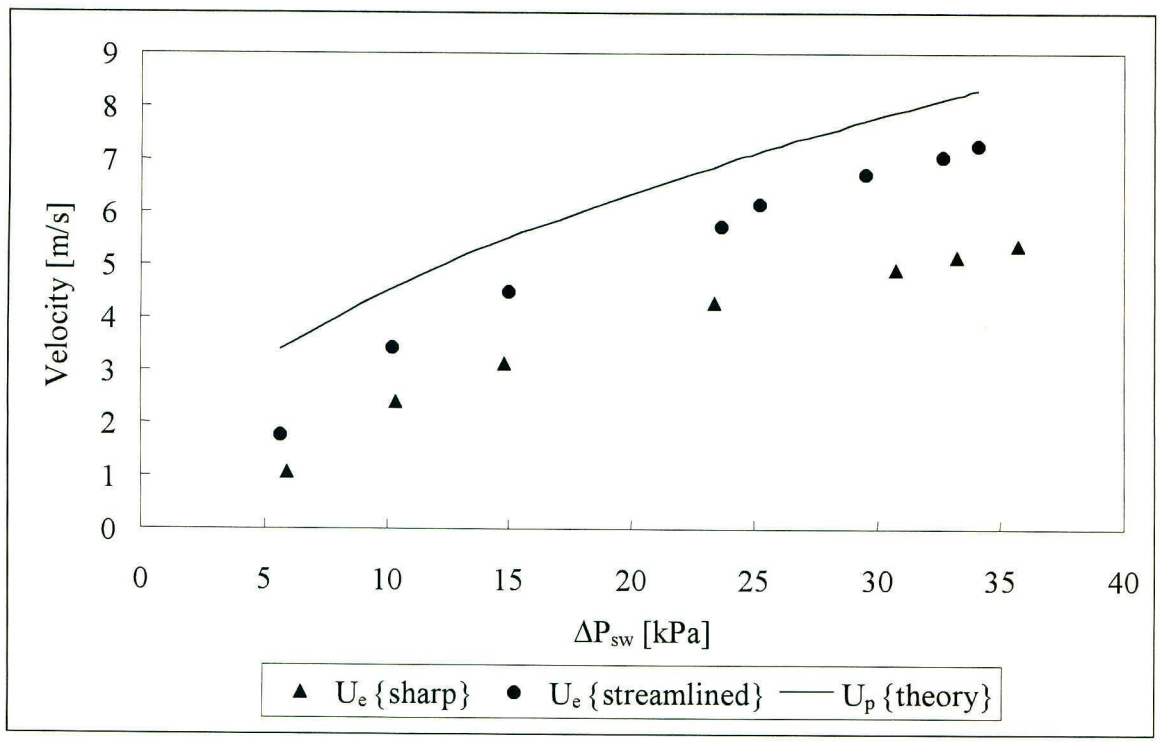

Figure 5 - 2: *Comparison of swirl port velocities.*

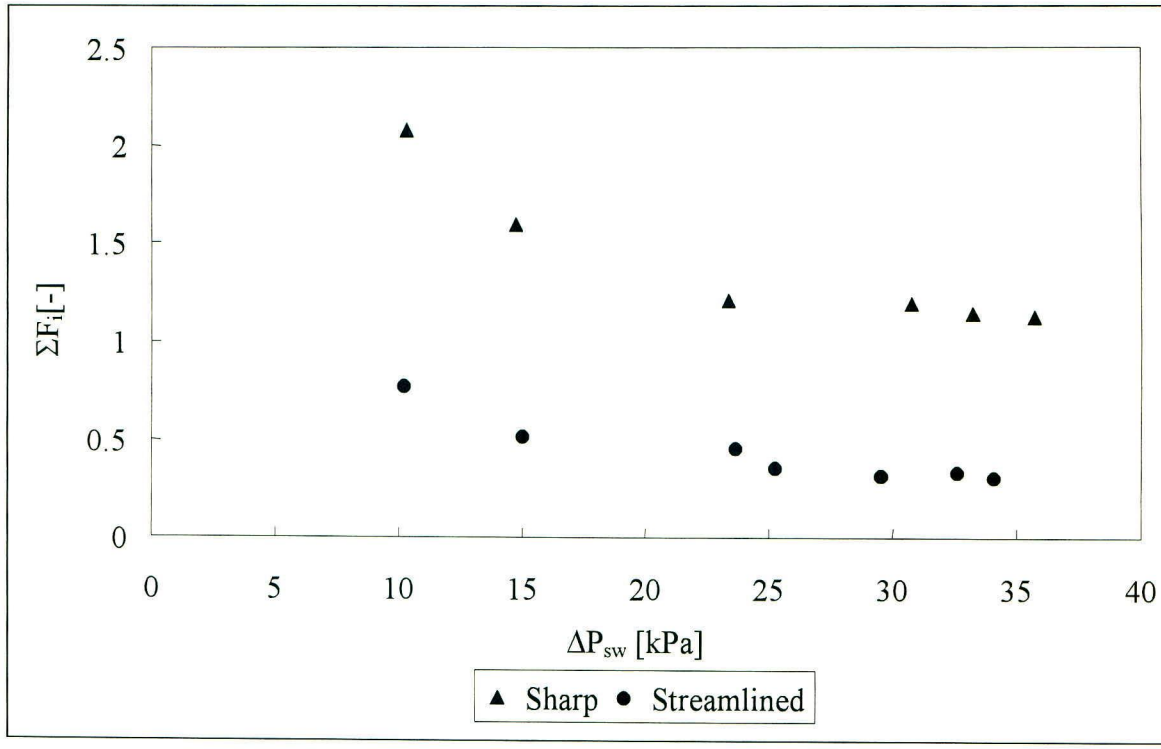

Figure 5 - 3: *Comparison of swirler loss coefficients.*

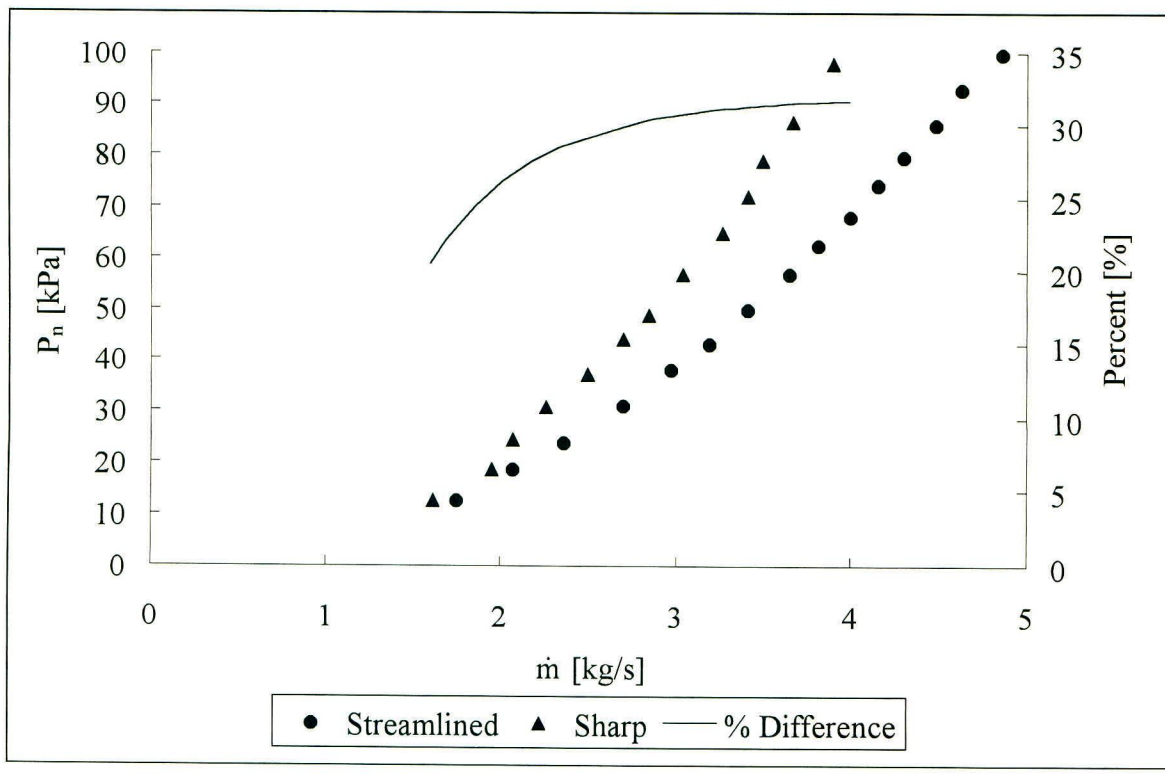

Figure 5 - 4: *Comparison of HCNs with different swirlers.*

The next experiment was aimed at determining the effect of swirler design on the required operating pressure of complete HCNs. This was achieved by assembling two identical nozzles, i.e. K = 0,421, with the two different swirlers and then measuring their respective mass flow

rates over a range of injection pressures. Results from this experiment show the significant reduction in operating pressure, which is achieved through the use of a streamlined swirler. Figure 5-4 shows the comparative supply pressures of the two nozzles required to maintain the various flow rates.

5.2 Hollow Cone Nozzle Tests

Having established that the new streamlined swirler considerably reduces the operating pressure of the HCN, it was decided to abandon the sharp edged swirler in all further tests. Thus, having decided only to use the new swirler in all remaining experimental work it was therefore necessary to determine all the relevant spray characteristics of the *new* HCN.

5.2.1 Spray Cone Angle

The first spray characteristic to be measured was the spray cone angle, 2θ. Figure 5-5 shows the liquid spray sheet issuing from a nozzle with $K = 0{,}632$. The spray cone angles of the nozzles tested were measured off photographs like this one. Visual observations and measurements taken with a pair of dividers, using the method described in Chapter 4, showed that 2θ was dependent on injection pressure for pressures less than 15 kPa. At these low pressures the spray cone is not yet fully developed and the spray sheet tends to be unstable. Increasing the pressure from 15 kPa to 25 kPa increases the spray cone angle and removes the instability. Increasing the injection pressure further above 25 kPa has no affect on the spray cone angle. With this in mind it was decided to measure the spray angle at an arbitrary pressure of 28 centimetres of mercury, roughly 35 kPa. In Figure 5-6 the spray cone angle data is shown graphically together with angles predicted by the equations presented in Chapter 3. Sample calculations implementing the various formulas are given in Appendix B.

Figure 5 - 5: *Photograph of spray cone.*

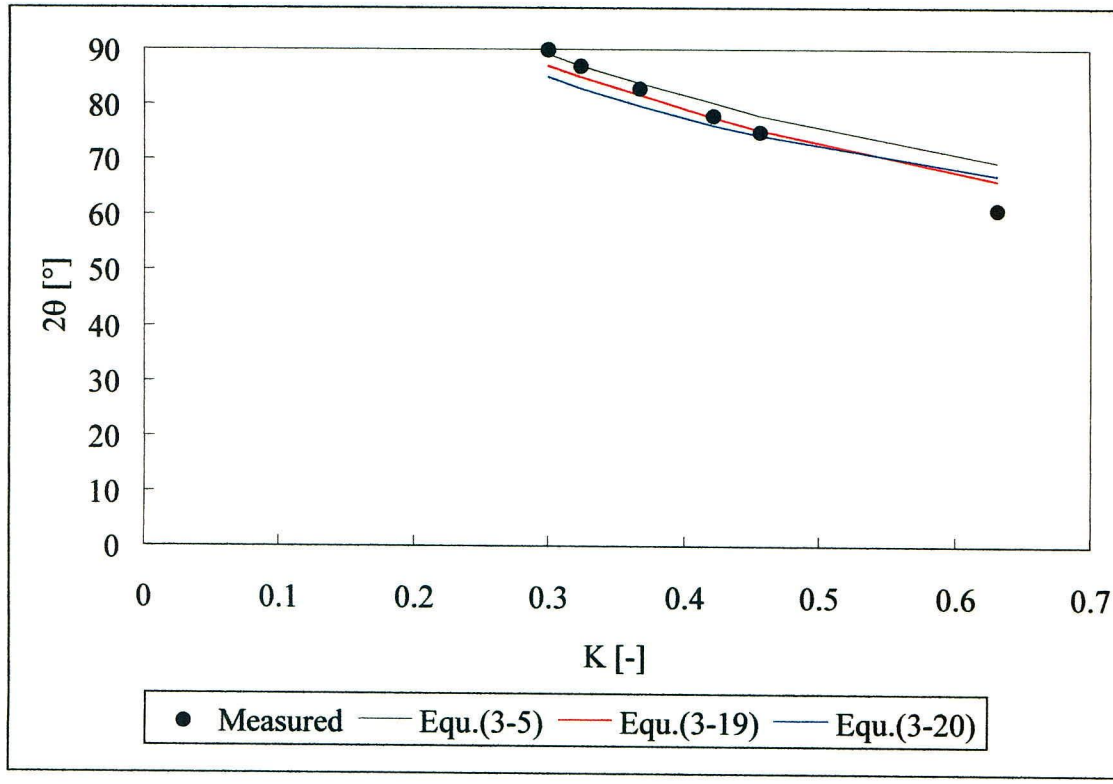

Figure 5 - 6: *Spray cone angle versus nozzle parameter, K.*

5.2.2 Discharge Coefficient

The data on discharge coefficient was collected from seven nozzles, which varied in geometry

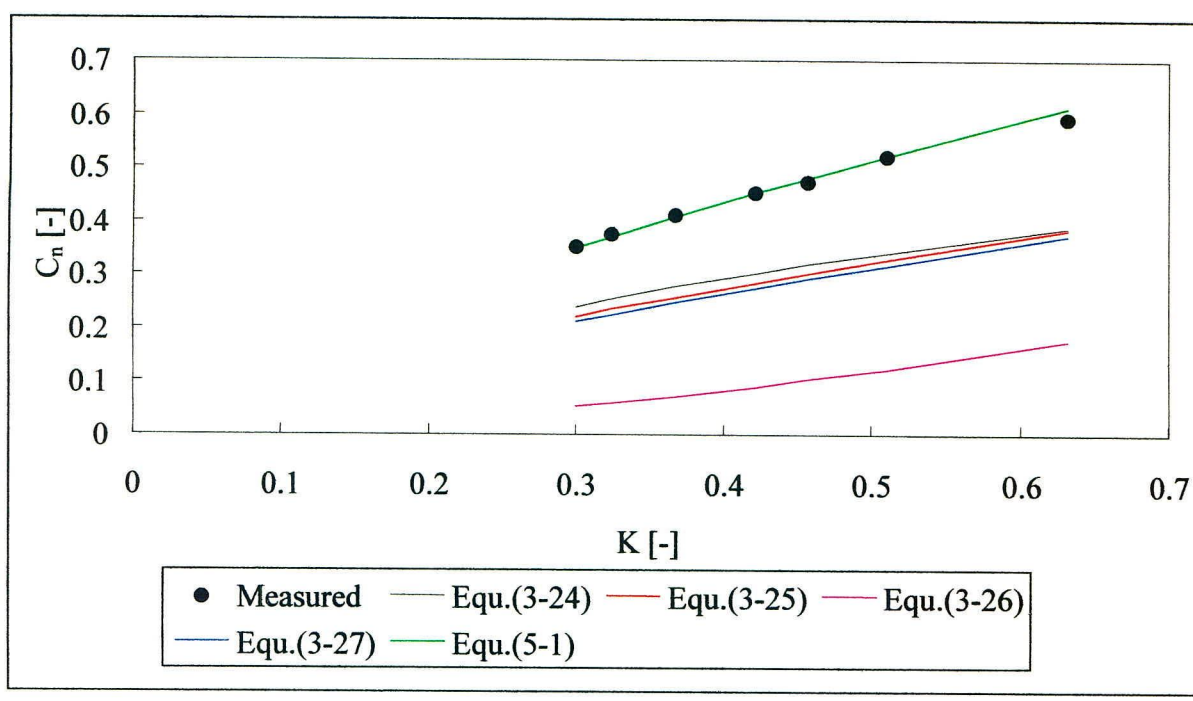

Figure 5 - 7: *Comparison of experimental and theoretical discharge coefficients.*

only with respect to orifice diameter. Measurements were taken at four different injection pressures ranging from 12 kPa to 77 kPa. The objective for this experiment was to determine whether or not discharge coefficient is affected by variations in injection pressure and if so whether it would be necessary to incorporate this dependence in correlating the data. Figure 5-7 shows the results from the test at 28 kPa and also shows the comparative predictions for discharge coefficient by the formulas presented in Chapter 3. Equation (5-1) was derived directly from Equation (3-27) – the two equations differing only by a factor. The derivation of Equation (5-1) is discussed in Appendix B, for now it is sufficient merely to present it here:

$$C_n = 0{,}578\,K^{0{,}5}\left(d_s/d_o\right)^{0{,}25}. \qquad (5\text{-}1)$$

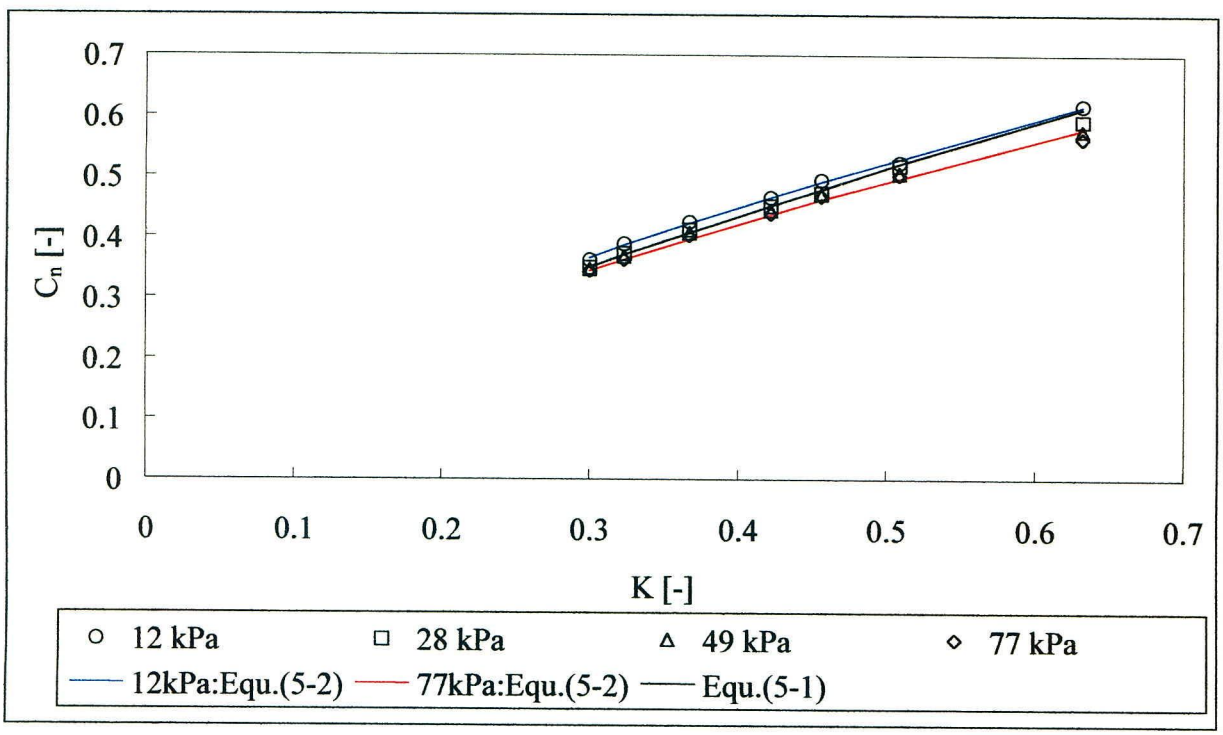

Figure 5 - 8: *Discharge coefficient versus K.*

Figure 5-8 shows the complete collection of discharge coefficient data from all seven nozzles — the dependence of C_n on injection pressure is clearly evident in this figure. Equation (5-2), which was also derived from Equation (3-27), takes the variation of discharge coefficient with injection pressure into account with the use of a Reynolds number term which replaces the coefficient in Equation (3-27). The equation looks as follows:

$$C_n = 1{,}468\left(Re_{d_o}\right)^{-0{,}067} K^{0{,}5}\left(d_s/d_o\right)^{0{,}125}. \qquad (5\text{-}2)$$

The Reynolds number, Re_{do}, is based on the pressure velocity, U_p, and the orifice diameter of the nozzle. In spite of these changes Equation (5-2) still retains many similarities with Equation (3-27). The only real difference between these two equations is the exponent of one eighth on the (d_s/d_o) term. This exponent was changed to compensate for the d_o term which is hidden in the Reynolds number, however, the combined exponent for d_o in Equation (5-2) is still approximately -0,7 as opposed to -0,75 in Equation (3-27). The exponent that does change is the one on d_s, which now has a value of -0,325 as opposed to -0,25 previously. The derivation of Equation (5-2) is given in Appendix B.

5.2.3 Film Thickness

As was explained in Chapter 4, two methods were used to measure the film thickness within the final orifice. The traverse mounted probe proved to be the more accurate and reliable means of measuring the film thickness. Figure 5-9 shows the axial velocity profiles of a HCN with d_o = 37,2 mm at four different injection pressures. The similarity between these profiles is an indication of the reliability of this method of measurement, however, the imperceptible difference in the air-core diameters, which may be due to the relatively large probe diameter,

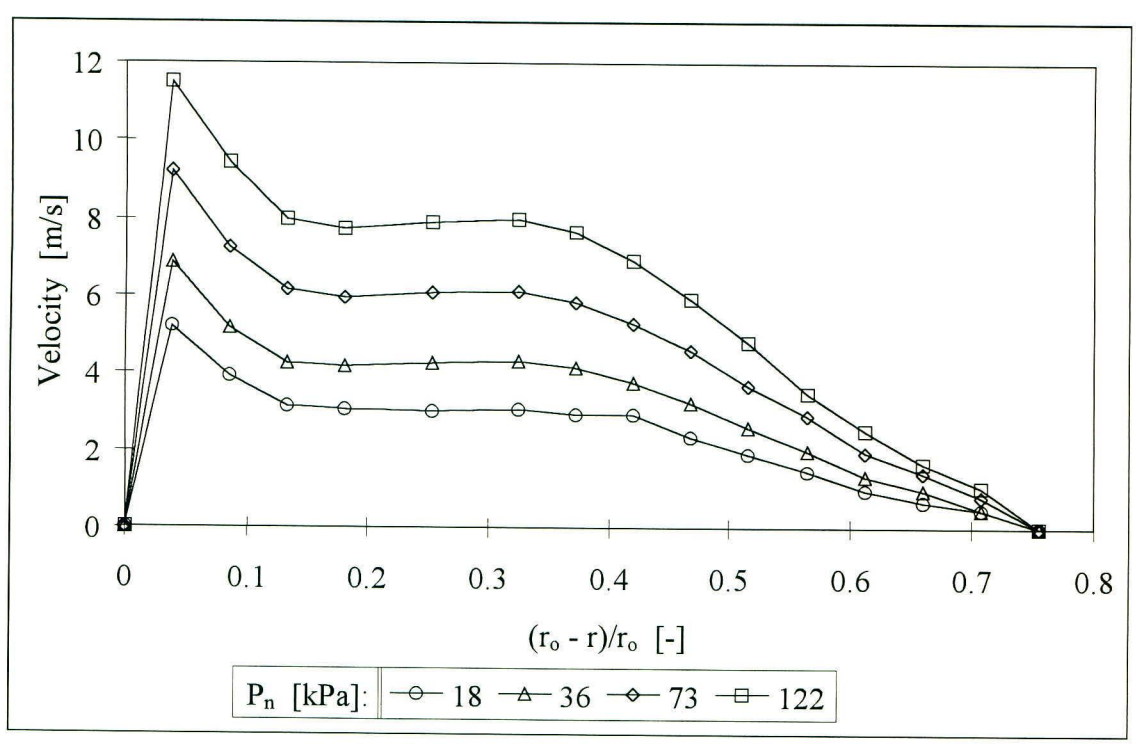

Figure 5 - 9: *Axial velocity profiles, K = 0,367.*

may also cause this method to appear inaccurate. However, measurements of the film thickness of five different orifice diameters taken with the probe all indicate that film thickness is not affected by variation in injection pressure. Therefore, it was concluded that for the range of pressures tested film thickness could be assumed to be a constant for each nozzle. With this in mind it was decided to implement a photographic method of film thickness measurement.

Figure 5-10 shows the photograph of the air-core of a HCN with $d_o = 29{,}9$ mm — not all the photographs taken are as clear as this one. Consequently slides were produced so that measurements of the air-core diameters could be taken from magnified images projected onto a screen. This, however, did not improve the accuracy of the method and it is proposed that perhaps a thermal imaging camera would result in a better contrast between water and air and therefore yield more accurate measurements of film thickness.

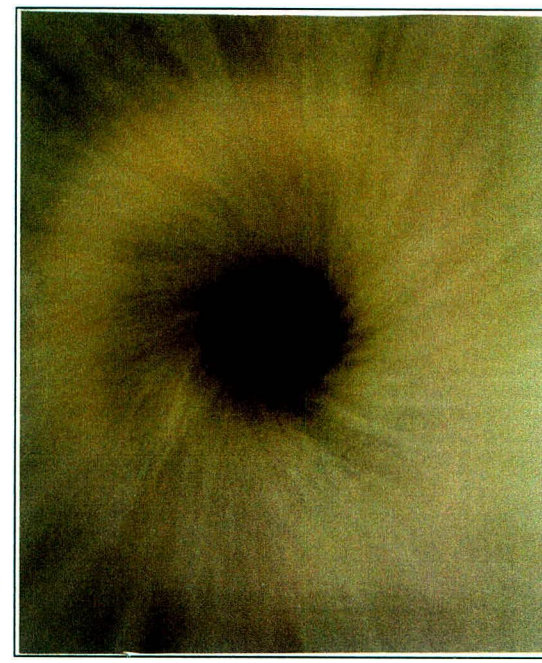

Figure 5 - 10: *Photograph of air-core.*

Figure 5-11 compares the measured data on film thickness with the various correlations and theoretical formulas given in Chapter 3. Due to the similarity of the gradients of the series labelled *probe* and Equation (3-33) it was decided to use this equation as a basis for correlating the film thickness. As with Equation (5-1), this equation differs from its predecessor by a factor only:

$$t = 9{,}81\left[\frac{d_o FN\mu}{\sqrt{\rho \Delta P_N}}\right]^{0.25} \qquad (5\text{-}3)$$

The method of determining the coefficient, 9,81, is given in Appendix B.

5.2.4 Spray Distribution

Experiments concerning the radial spray distribution of HCNs were done to obtain a more complete understanding of the operation of HCNs. Although the system of measurement which

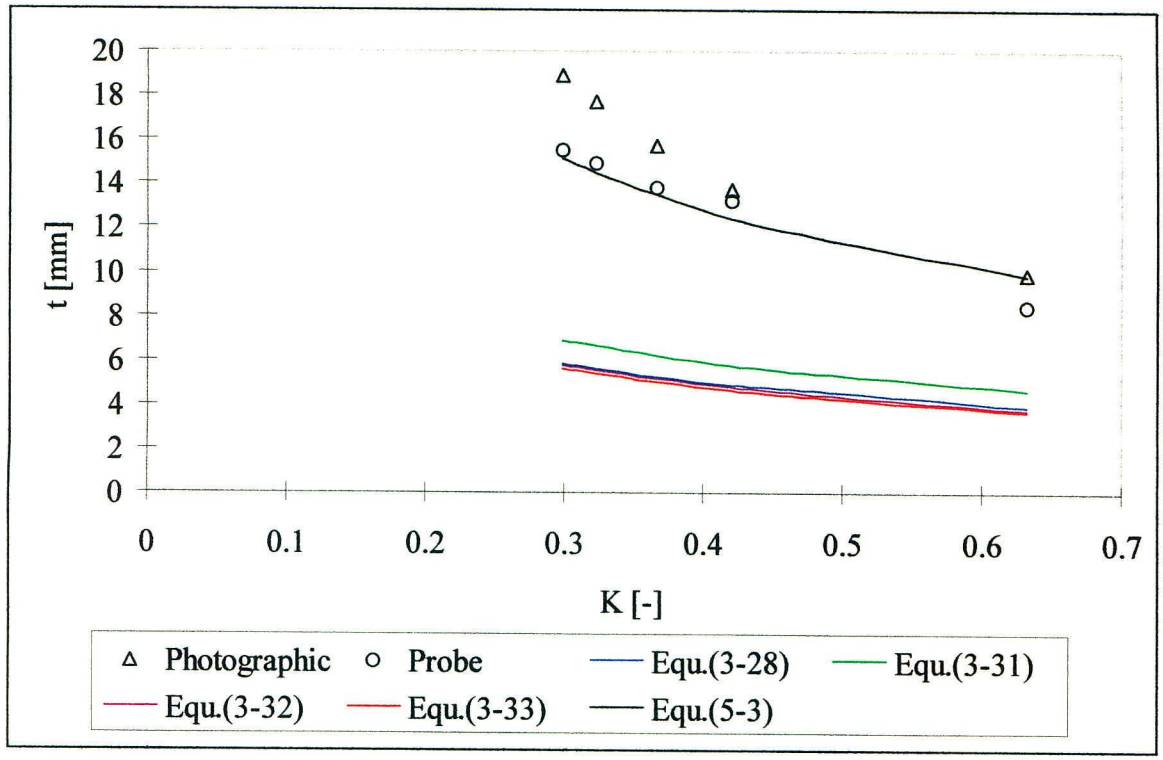

Figure 5 - 11: *Film thickness versus nozzle parameter, K.*

only takes selected rainfall intensity data points at one position beneath the spray may not be a true representation of the distribution, this is sufficient to obtain a visual record of the distribution and adequately characterise the spray. The data points in all of the following graphs have been fitted with cubic splines so that the general trend can be more readily identified.

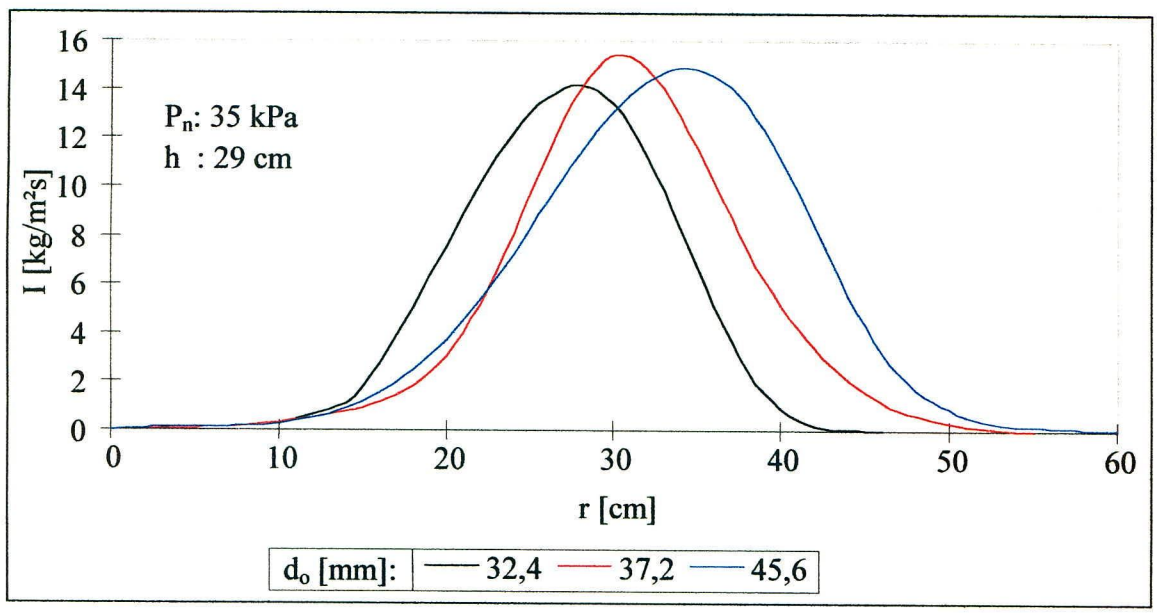

Figure 5-12: *Affect of varying orifice diameter.*

The first experiments involved measuring the radial distribution of HCNs using the sharp-edged orifice so that the effect of increasing orifice diameter could be investigated. Figure 5-12 shows how the radial distribution moves outwards as orifice diameter is increased, this is to be expected since the spray cone angle is also greater for larger orifice diameters.

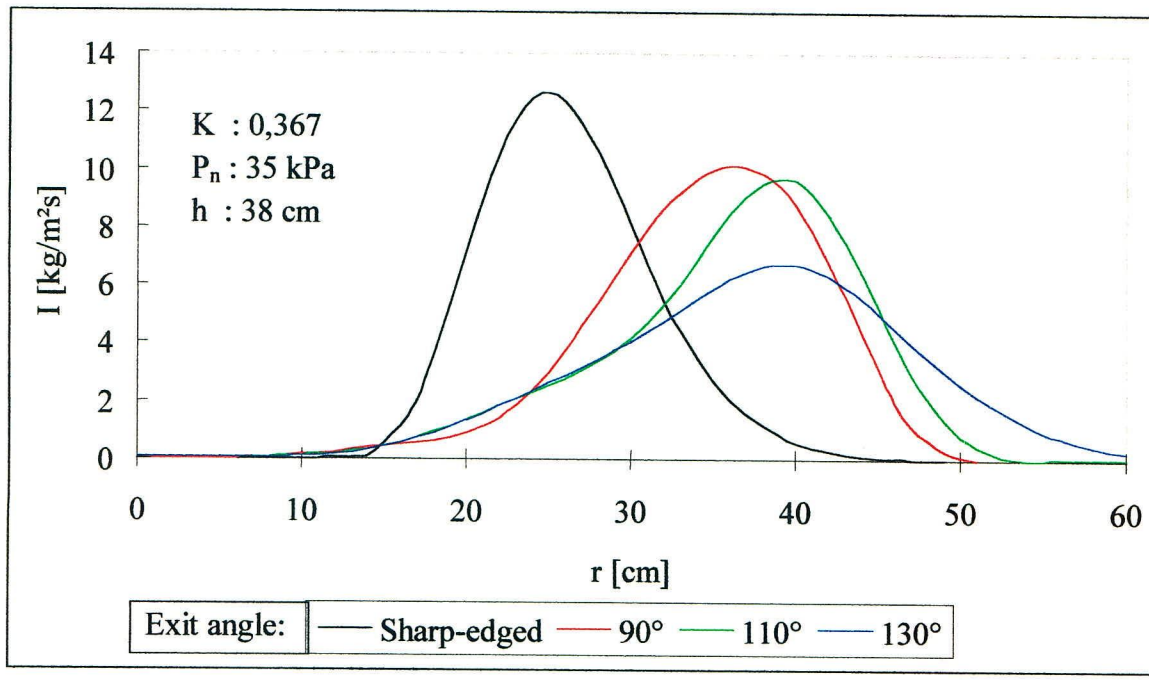

Figure 5 - 13: *Effect of rounding the nozzle exit.*

The next experimental work was aimed at investigating the effect of rounding the final orifice on radial distribution. Although the ratio of orifice diameter to swirl chamber diameter appears to govern the radial distribution, rounding the final orifice can dramatically alter this distribution. Rounded outlets, see Figure 4-6, were constructed to cover a range of exit angles in order that the practical limits of the Coanda effect could be determined. The effect of rounding as compared to not rounding the nozzle exit is shown graphically in Figure 5-13. Notice how the exit rounded to 130° seems only to flatten out the distribution without actually increasing the radius of the spray.

Integration of this knowledge concerning the Coanda effect lead to the design and manufacture of a non-axisymmetrically profiled outlet to produce a *square* spray pattern. The profile makes use of a varying exit angle to induce the spray further outwards into the corners of the projected *square* spray area. Figure 5-14 is a contour plot of the rainfall intensity measured beneath the HCN using this profiled outlet. Although the distribution intensity was only

measured over one quadrant of the spray, this distribution has been assumed to prevail in the others quadrants also so that the complete distribution could be plotted for visual emphasis. Figure 5-14 illustrates the *squaring* effect, which can be achieved with the use of a profiled outlet. Appendix C, which describes the process of designing a FCN, contains a detailed description of the geometry of such a profiled outlet.

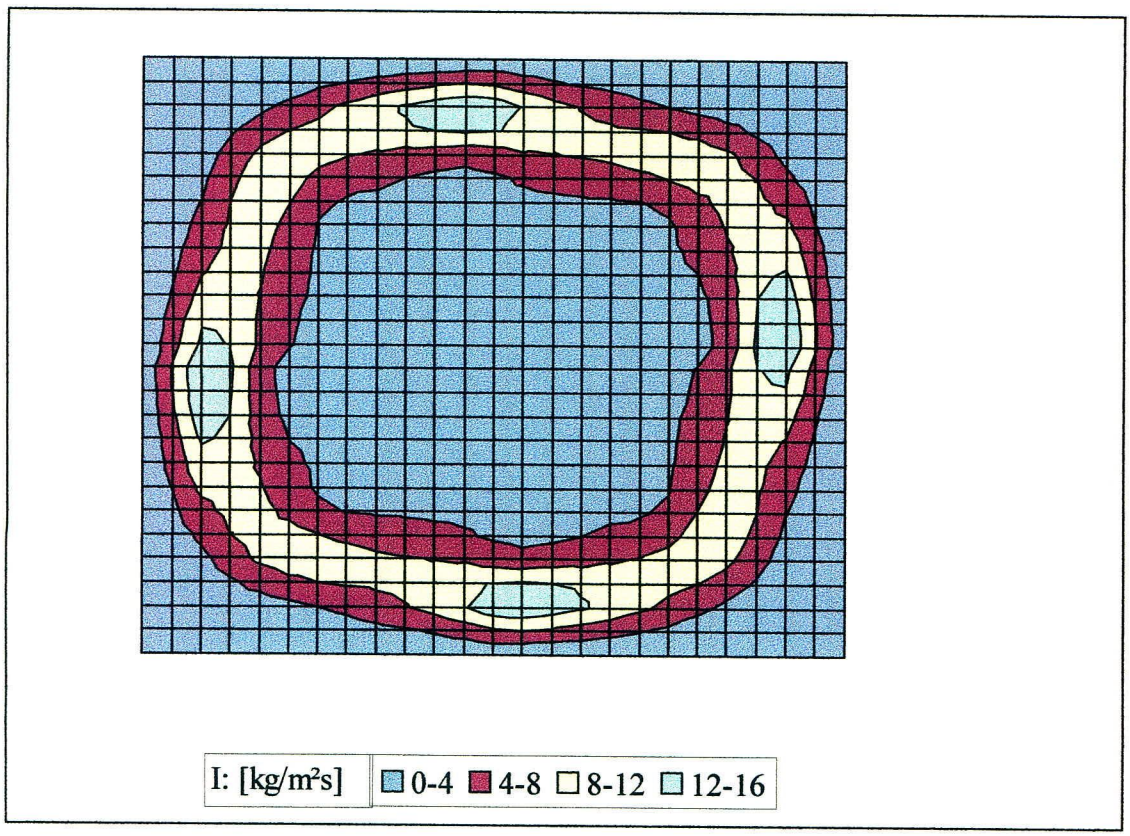

Figure 5 - 14: *RID from nozzle with profiled exit.*

5.3 Full Cone Nozzle Tests

Having tested the HCN and obtained useful correlations for all the necessary characteristics, the next step was to test the FCN for a better understanding of its operation and distribution characteristics. There are two aspects of the central jet, which affect distribution uniformity; they are central jet diameter, d_j, and central jet protrusion length, l_j. See Figure 4-7 for a recap of where these dimensions are measured on the nozzle. The graphs in the following sections are an attempt to illustrate the affect of the various nozzle elements on the radial distribution of the FCN. Where it is sufficient merely to show the distribution with a single line graph that

has been done, however, in the event of non-symmetrical distributions, contour intensity graphs similar to Figure 5-14 have been used.

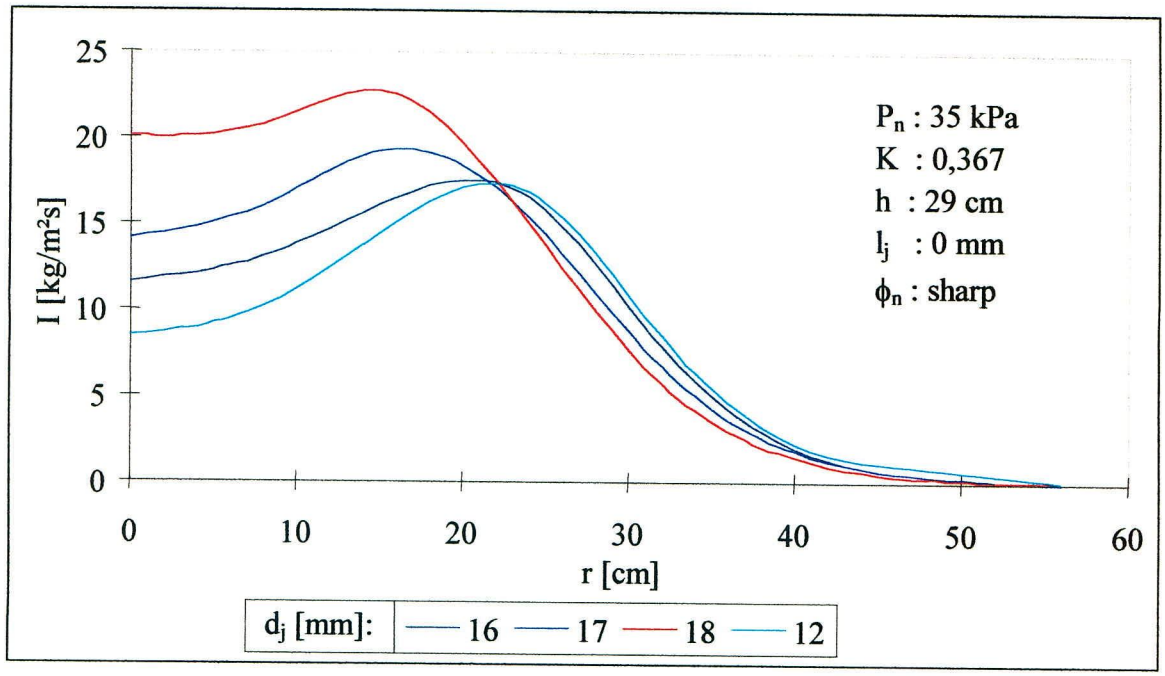

Figure 5 - 15: *Measured RIDs from FCNs with sharp-edged orifice.*

5.3.1 Influence of Central Jet

Many combinations of jet diameter and orifice diameter were tested during the course of this project. Much of the data is of little significance, however, because of the irregular and uneven distributions. Figure 5-15 shows some of the arbitrary distributions obtained from nozzles using only the sharp-edged exit profile. Notice how these distributions are all hollow in the centre. This is due to the strong influence of the rotating liquid sheet through which most of the water exits the nozzle.

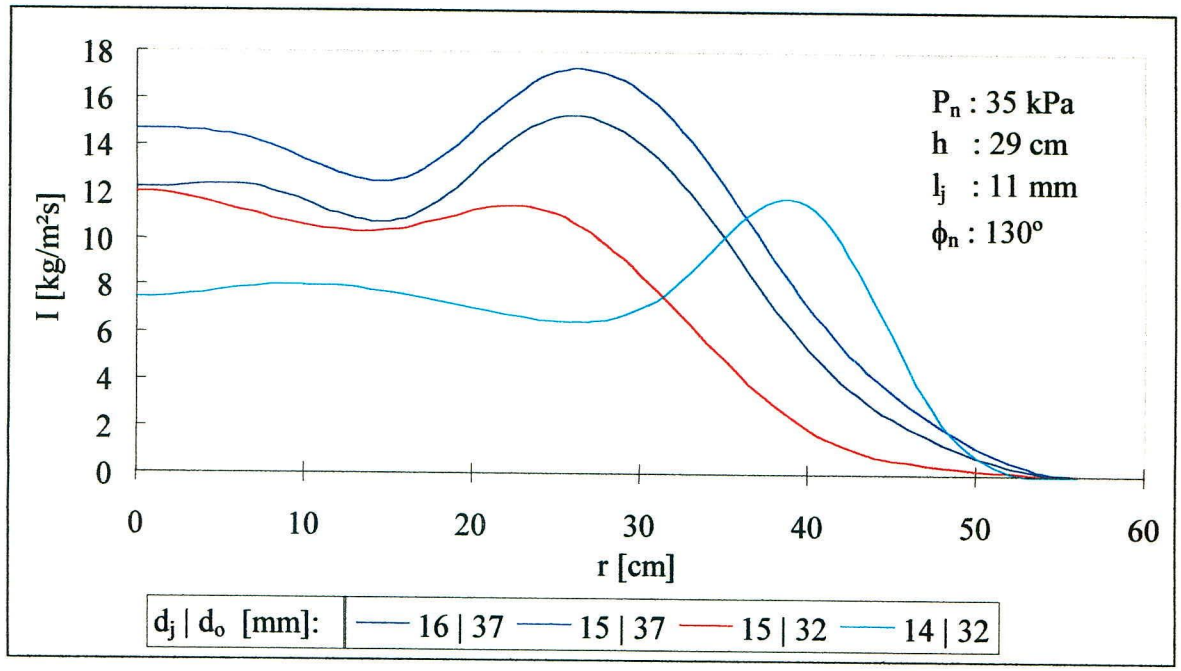

Figure 5 - 16: *Measured distributions from FCNs with various K values.*

The remainder of the graphs in this section depict distributions from nozzles using the profiled exit, $\phi_n = 130°$. Notice, in Figure 5-16, how the curves for the nozzle with $d_o = 32$ mm have lower average rainfall intensities. This is due to a reduction in outlet flow area, which causes a greater pressure loss across the orifice, resulting in smaller mass flow rates through the nozzle.

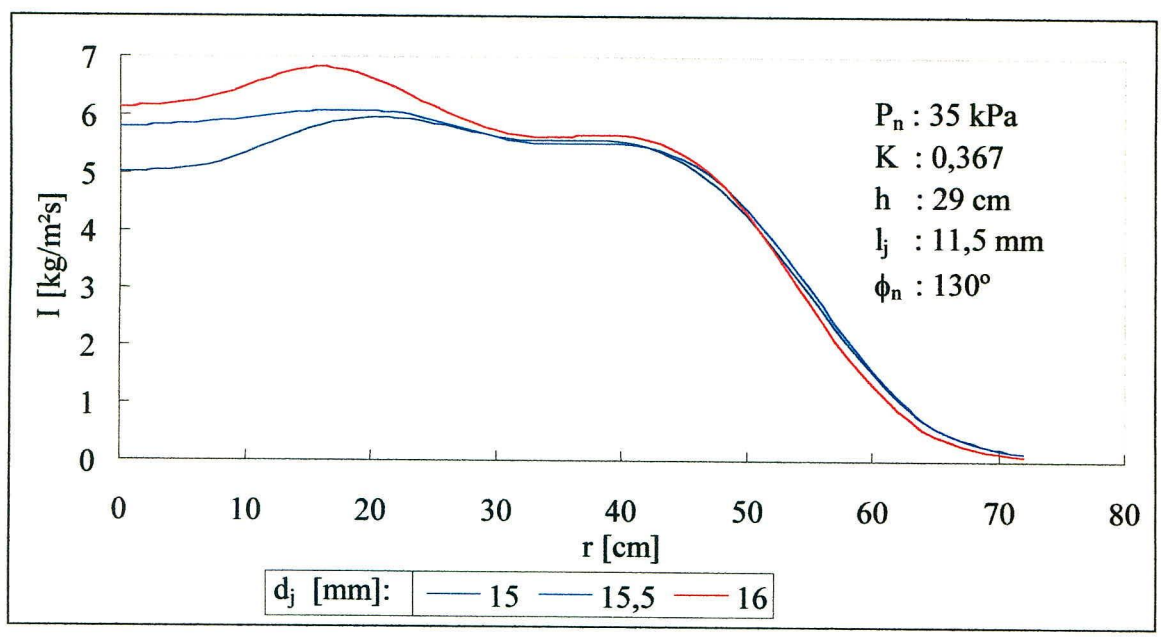

Figure 5 - 17: *Effect of varying jet diameter.*

The first aspect of the central jet to be investigated was central jet diameter, d_j, which was found to significantly affect the radial distribution of FCNs. Figure 5-17 contains selected data which illustrates the effect of jet diameter, d_j, on radial distribution. The data used in this

illustration are from experiments conducted with nozzles using a jet protrusion length, l_j, of 13 mm. The effect of varying the jet diameter, d_j, can be summarised, in terms of the ideal limit which would result in a perfectly flat and uniform curve, as follows:

- Increasing jet diameter, d_j, beyond the ideal limit causes the rotating liquid sheet to become entrained with the jet thus inducing the distribution to peak in the centre.
- Decreasing jet diameter, d_j, marginally below the ideal limit causes the jet to become diffused by the rotating liquid sheet resulting in a depression at the centre of the distribution.
- Decreasing jet diameter, d_j, substantially below the ideal limit causes the jet to stream through the air-core, i.e. not interfering with the rotating liquid sheet, resulting in an extreme peak at the centre of the distribution.
- The ideal jet diameter, d_j, results in a distribution that is uniform or flat on top.

While experimenting with HCNs it became apparent that the discharge coefficient of the HCN could be increased by inserting a solid core into the centre of the nozzle immediately below the swirler. Not only did this solid core increase the flow rate, but also there was in fact an optimal protrusion length, which resulted in a maximum discharge coefficient for each nozzle. The discovery of this phenomenon prompted an investigation into the effect of jet protrusion length, l_j, on FCN performance. Figure 5-18 shows the effect of protrusion length, l_j, on radial distribution. The effects of varying the jet protrusion length, l_j, can be summarised as follows:

- Increasing jet protrusion length, l_j, has the same effect as increasing jet diameter, d_j, namely

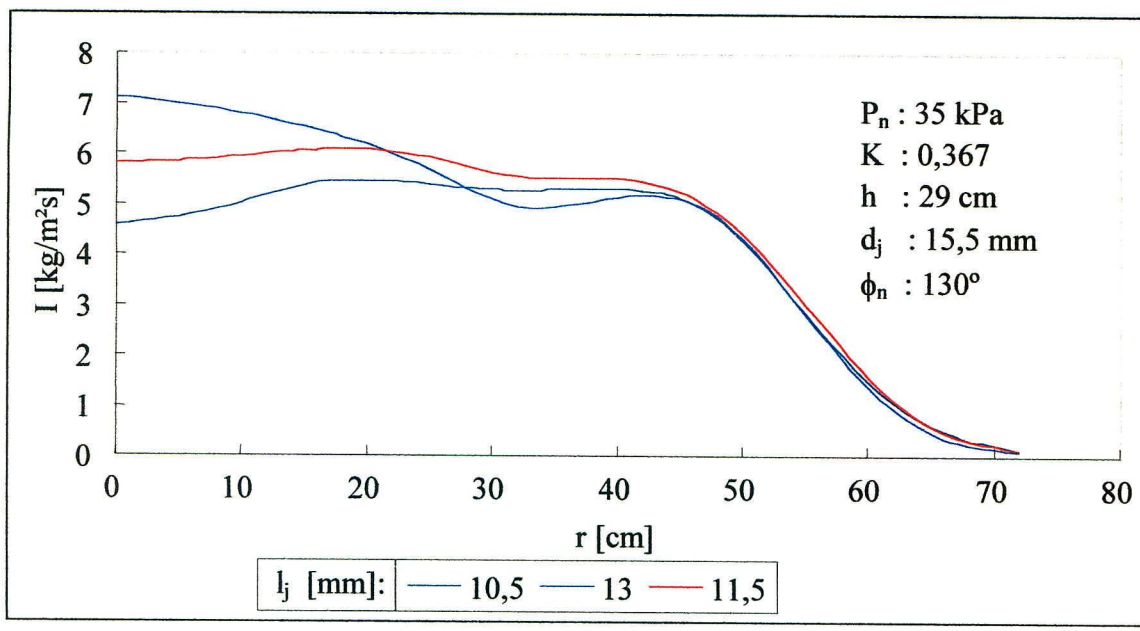

Figure 5 - 18: *Effect of varying protrusion length.*

that the distribution will peak in the centre.

- Decreasing jet protrusion length, l_j, has the same effect as decreasing jet diameter, d_j, namely that the distribution will dip in the centre.
- As with jet diameter there is also an ideal protrusion length that will result in a uniform spray distribution, however, this limit is dependent on both these quantities and cannot be realised if either is outside of the range for such distributions.

Having gained an understanding of the effect of central jet geometry on FCN distribution, it was then necessary to determine experimentally the relationship between central jet geometry and orifice diameter. Ideally this work should have been done with a range of profiled nozzle outlets, however, due to the expense of producing such a range of profiled outlets it was decided to calibrate jet diameter, d_j, and orifice diameter, d_o, for the sharp-edged orifice nozzles only, and then to extrapolate the results to include profiled exits. The task of selecting the jet diameter proved to be more difficult than was originally anticipated due to the fact that jet inserts had only been manufactured at diameter intervals of 0,5 mm. After much experimentation, mostly unrecorded visual testing, a series of uniform distributions were obtained from which the following relationship was wrested:

$$d_j = 0{,}0193\,X^{0{,}117}. \qquad (5\text{-}4)$$

This correlation was determined from experimental data for nozzles with a jet protrusion length, l_j, of 9 mm and operating at an injection pressure, P_n, of 35 kPa. In this equation X is the ratio of air-core area to orifice area and is a function of film thickness.

Having found a correlation for calculating the correct diameter of jet for a given orifice diameter, the next experiment was aimed at determining the relationship between the flow rate through the central jet and the flow rate through the swirler. This relationship is necessary for accurately calculating the flow rate through complete FCNs. Figure 5-19 shows the experimental set-up that enabled the jet flow rate to be measured independently of the swirler flow rate. The water flowing through the jet was separated from the rest, which naturally flowed through the swirl ports, collected in a large drum and then simply weighed on a scale. The flow rate was then calculated by dividing the mass of ware collected by the time in seconds that the drum took to fill. This was the only practical means of determining the relationship between the central jet flow rate and the combined swirl port flow rate. Testing was conducted over a range of flow rates and with jet diameters of 16, 17 and 18 mm.

The anticipated result for this experiment was that the flow rate through the jet would be proportional to the ratio of jet area to inlet port area, A_p – this was indeed found to be so. The following correlation, which relates jet flow rate to swirl port flow rate, was determined from the experimental results:

$$\dot{q}_j = 0{,}989 \frac{A_j}{A_p} \dot{q}_p . \qquad (5\text{-}5)$$

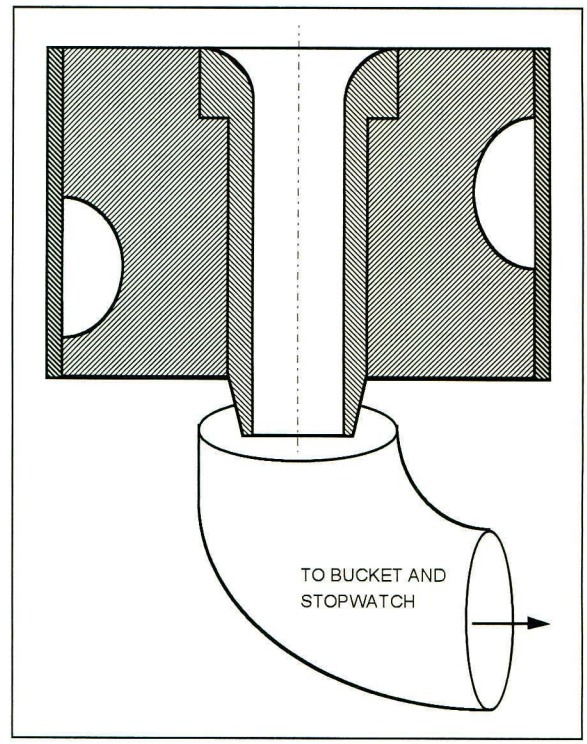

Figure 5 - 19: *Configuration for determining central jet flow rate.*

5.3.2 Comparison of Two FCNs

Until now, most the experiments concerning distribution have been conducted on nozzles that produce axially symmetric sprays. For practical reasons, however, cooling towers are constructed with square cross-sections, which means that nozzles producing a circular spray pattern cannot be effective in wetting the pack uniformly. In this section the prototype FCN that has been used throughout this project was tested with the profiled exit, see Appendix D, and compared to a commercially available cooling tower nozzle of similar dimensions. The critical dimensions of the prototype nozzle are d_o = 37,2 mm, d_j = 15,5 mm and l_j = 5,5 mm and of the commercial nozzle are: d_o = 37 mm, d_j = 17 mm and l_j = 0 mm. Both nozzles have a swirl chamber diameter of approximately 68 mm. Figures 5-20 and 5-21 show sample three-dimensional relief plots of the distribution intensity of the two nozzles.

Figures 5-22 and 5-23 again show the distribution intensity data of a these two nozzles, only this time as contour plots. The distribution uniformity and spray pattern is readily identified in each of these figures. As opposed to being compared at a given injection pressure, P_n, of 35 kPa, the two nozzles were tested at an equivalent mass flow rate, $\dot{m}$, of 4,68 kg/s. The reason for this is that the two nozzles have different discharge coefficients resulting from the different swirler designs and the only fair way to compare the rainfall distributions for such nozzles is at equal mass flow rates.

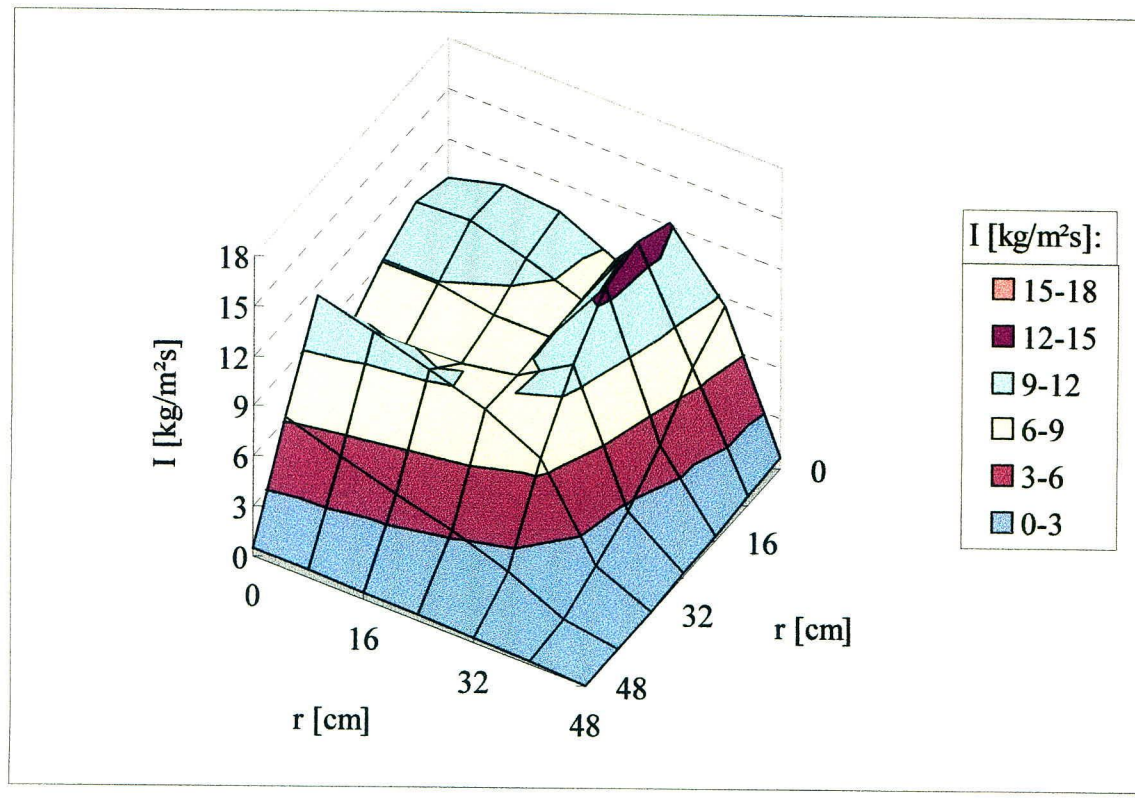

Figure 5 - 20: *3-D RID of prototype FCN with profiled outlet.*

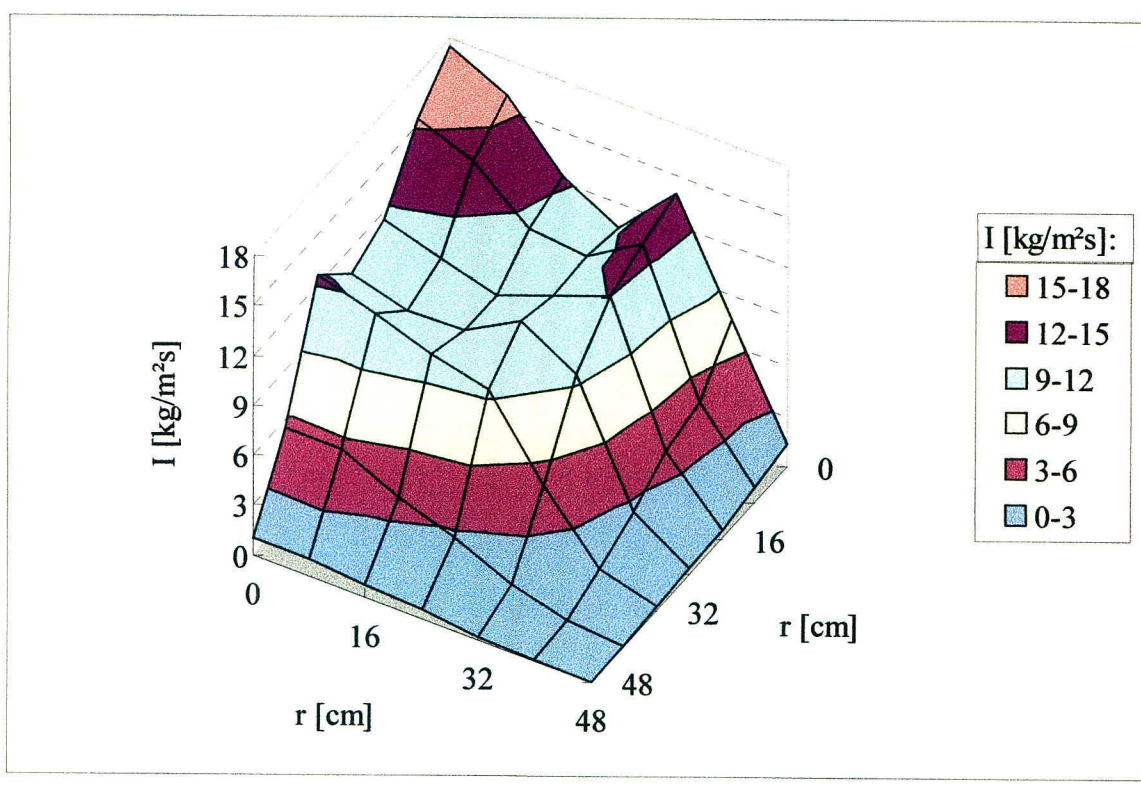

Figure 5 - 21: *3-D RID of commercial FCN.*

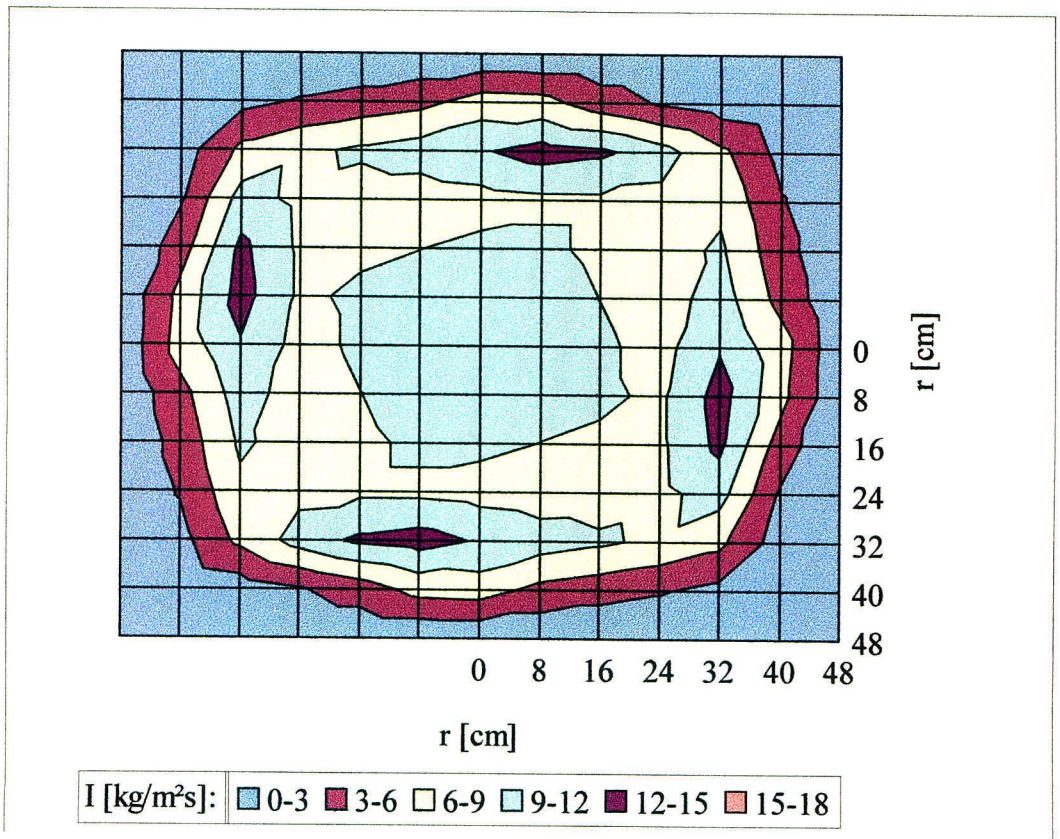

Figure 5 - 22: *RID from prototype FCN with profiled outlet.*

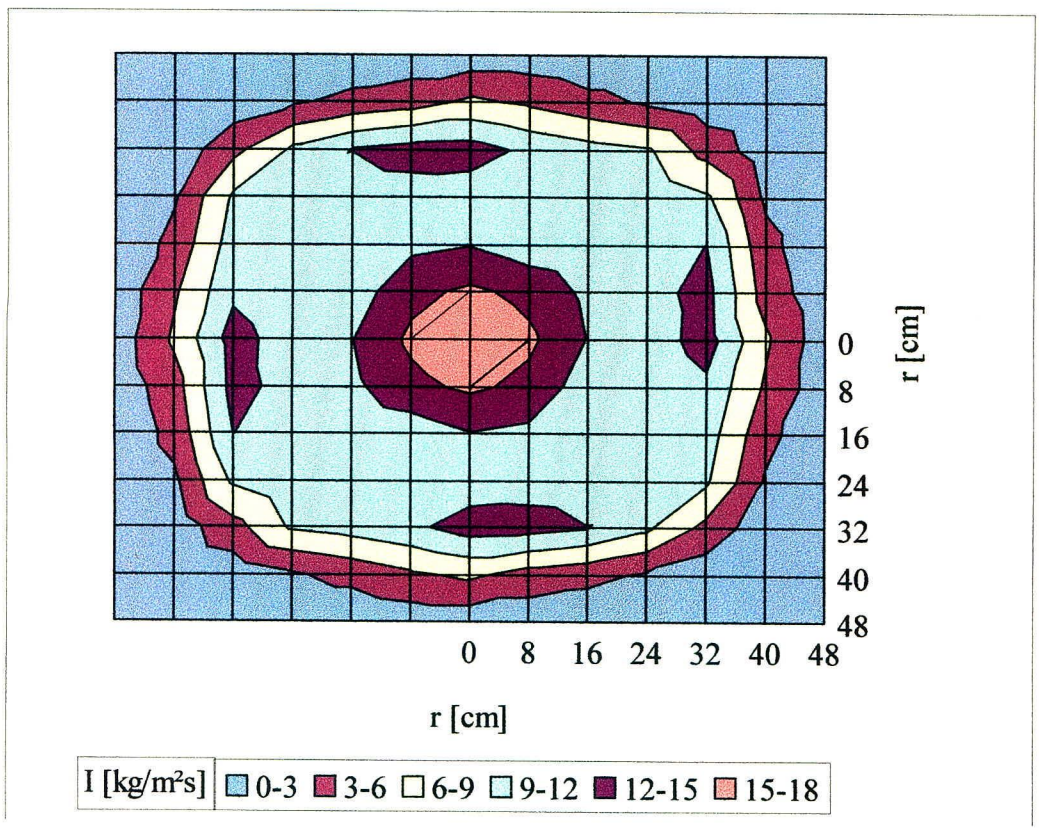

Figure 5 - 23: *RID from a commercial FCN.*

CHAPTER SIX

DISCUSSION OF EXPERIMENTAL RESULTS

6.1 The Swirler

The most notable observation concerning the streamlined swirler is the significant reduction in required operating pressure compared with the sharp-edged swirler. Figure 5-2 compares the performance of two HCNs using different swirlers but having identical K values of 0,421 and although this is only one test case, the trend is indicative of all HCNs using a more streamlined swirler. At a supply pressure of 35 kPa the nozzle utilising the streamlined swirler shows a gain in flow rate of roughly 25 percent compared with the other nozzle. As the pressure increases the percentage difference in flow rate approaches a constant value of 31,5 percent. This levelling off is the result of the swirler loss coefficients approaching their asymptotic values as the pressure drop across the swirlers increases. At a flow rate of 2,5 kg/s the nozzle using the streamlined swirler requires only 70 percent of the pressure required for the nozzle using the sharp-edged swirler. This reduction in operating pressure is of primary importance to the overall efficiency of the nozzle, especially when considering the long-term costs of cooling tower operation.

Under normal operating conditions a HCN will exhibit two distinct pressure drops – one across the swirler and the second across the final orifice. The method of predicting swirler loss coefficients has proved to be an effective means of analysing the flow through the swirler, therefore, by expanding this analysis it is also possible to estimate the individual pressure drops across the swirler and the orifice. This is done by modifying the swirler loss coefficient to include an exit loss coefficient, which can be attributed to the sudden expansion of the flow into the swirl chamber. This extra term can be estimated with the following equation, modified from the original White [86WH1] equation:

$$F_{se} \approx \left(1 - \frac{A_p}{A_s}\right)^2, \qquad (6\text{-}1)$$

where F_{se} is the pipe loss coefficient for sudden expansion. Substitute the same values used in Equation (3-2) namely, A_p = 932 mm² and A_s = 3664 mm², into Equation (6-1) to obtain a value of 0,556 for F_{se}, which is valid for both sharp-edged and streamlined swirlers.

The variation of experimental loss coefficient data with nozzle pressure drop, see Figure 5-3, is included in this analysis through the use of the following approximate power law curve fit equations for the two swirlers:

- streamlined: $F_{sw} \approx 13{,}3\Delta P_{sw}^{-1{,}097} + 0{,}556$ (6-2)
- and sharp : $F_{sw} \approx 27{,}2\Delta P_{sw}^{-0{,}942} + 0{,}556$, (6-3)

where F_{sw} is the total loss coefficient for swirlers with submerged exits, i.e. under normal operating conditions. Rearranging Equation (3-1) yields the following equation for pressure drop across the swirler:

$$\Delta P_{sw} = 1/2\,\rho U_e^{\,2}(F_{sw} + 1), \quad (6\text{-}4)$$

where swirl port velocity, U_e, can be calculated from one of the correlations for discharge coefficient namely Equation (5-1) or Equation (5-2).

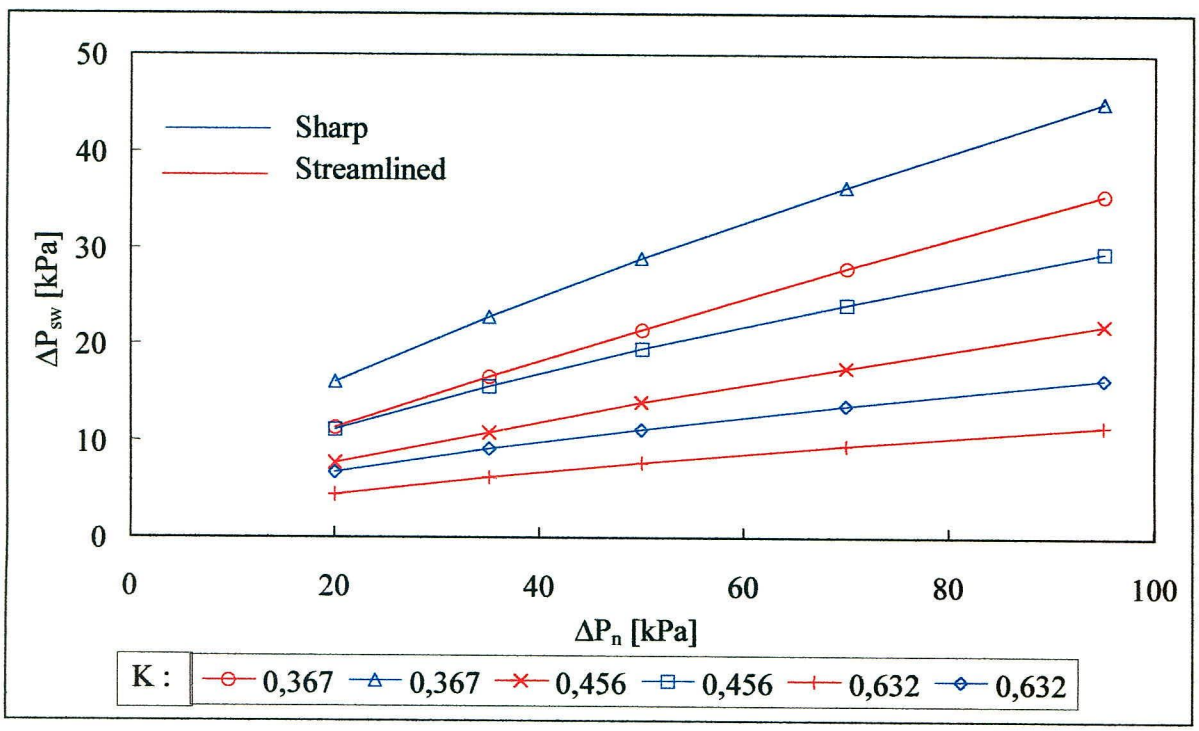

Figure 6 - 1: *Swirler pressure drop in a HCN.*

Figure 6-1 shows the results of this analysis for nozzles with different K values and different swirlers. The sample calculations can be seen in Appendix B.7. Referring back to Figure 5-1 it becomes apparent why the discharge coefficient falls away when the nozzle parameter, K, exceeds 0,5. This is due to the high swirler loss coefficients that occur at low swirler pressure drops. Minimum swirler pressure drops of 10 kPa for the streamlined swirler and 15 kPa for the sharp swirler are required if the loss coefficients are to approach their asymptotic values.

For the nozzles with K = 0,632 the swirler pressure drop does not exceed either of these minimum values even at a nozzle pressure drop of 80 kPa, therefore, at injection pressures of less 80 kPa these nozzles will incur high irreversible losses through the swirler.

6.2 HCN Characteristics

Spray cone angle is the only characteristic that was measured and found to be in good agreement with the theoretical treatment of Chapter 3. Unfortunately, due to the distortion of this angle that is caused by the presence of the central jet in the FCN, knowledge of this angle is of little use in designing FCNs. This does not mean that the spray cone angle of a FCN cannot be accurately predicted, but rather that it can be, especially when a rounded exit profile with known exit angle is attached to the final orifice. In the case of a symmetrical FCN the spray cone angle can be expected to be within 5 degrees of the nozzle exit angle, ϕ_n.

The discharge coefficients of the tested nozzles show both a steeper gradient and higher all-round values compared with the estimates from the equations in Chapter 3. There are two reasons for the increased discharge coefficient. Firstly, streamlining the swirl ports reduced the required operating pressure by minimising the irreversible losses. Secondly, these higher values are due to the use of spiralled inlet ports as opposed to tangential inlets for which the theoretical formulas were derived.

There are two factors that are related to port entry angle and which greatly affect discharge coefficient. They are viscous dissipation, which takes place along the length of the swirl chamber, and back pressure, which is dependent on the ratio of axial to tangential velocity at the entry to the swirl chamber. For tangential inlet nozzles the velocity of the liquid entering the swirl chamber is almost purely tangential. This means that in order for the nozzle to discharge any liquid at all, some of the kinetic energy in the swirling liquid must be used to increase the axial velocity component. The conversion of tangential velocity to axial velocity is not in itself a loss, but the viscous losses associated with this process are significant.

Tangential inlet nozzles have lower discharge coefficients due to the greater back pressure, which is experienced at the swirl port exits. Back pressure exists because of the radial pressure

gradient that is set up by the swirling liquid. The higher the ratio of tangential to axial velocity at the swirler exit the greater will be the radial pressure gradient and the greater will be the back pressure also. This increases the required injection pressure and reduces the discharge coefficient. The fact that testing was done at relatively low injection pressures is also a factor that has contributed to the increased discharge coefficients for the experimental nozzles. This is apparent from the dependence of discharge on injection pressure and is evident in Figure 5-7. Equation (5-1) and Equation (5-2) have been shown to satisfactorily correlate the measured discharge coefficient data.

Film thickness showed little variation with injection pressure. In spite of this finding the equation used to correlate film thickness contains a pressure term. However, due to the nature of this equation, i.e. taking the fourth root of the various arguments, the influence of pressure is kept to a minimum.

Radial distribution from HCNs is affected by orifice diameter and orifice rounding and is also a function of the height of the nozzle above the plane of measurement. Judging from Figure 5-13 there appears to be a limit to the effectiveness of rounding of the nozzle outlet. The 90° and 110° exit profiles move the distribution radially outwards while the 130° profile only succeeds in *flattening out* the distribution without actually shifting it any further outwards than was achieved with the 110° profile. Figure 5-14 shows that a *square* distribution can be created if the right exit profile is used.

6.3 FCN Characteristics

Jet diameter and jet protrusion length are two parameters that have been shown to influence the distribution uniformity of FCNs. The general trend and relationship between these two dimensions and the orifice diameter have already been discussed in Chapter 5, however, there are some finer points on central jet selection which have not yet been discussed.

The first point concerns jet diameter. If a distribution is observed to have a peak of higher intensity halfway between the centre of the spray and the perimeter, as shown by curve labelled d_j = 16 mm in Figure 5-17, this is an indication that the jet diameter is too large for the nozzle

orifice diameter. Such a distribution cannot be made uniform by altering l_j because decreasing l_j will only amplify the trough at the centre and increasing l_j will only exaggerate the bulge, which is already present in the distribution.

The indication of d_j being too small is evident from a distribution that exhibits one peak in the centre and another towards the edge of the spray. A distribution such as described here cannot be made uniform by adjusting the protrusion length. The explanation for this is that increasing l_j will only amplify the central peak and decreasing l_j will only magnify the peripheral peak. The three curves in Figure 5-18 are a good illustration of this phenomenon, the distribution with l_j = 11,5 mm is, however, very close to being *perfectly* uniform.

The ideal jet diameter will cause the distribution to peak in the centre when l_j is too large and cause the distribution to peak at the perimeter when l_j is too small. However, as l_j is gradually decreased from being too large the distribution will flatten out in the centre and build up on the perimeter. This process will result in a distribution that seesaws from a peak in the centre to a peak at the perimeter. The ideal protrusion length, which corresponds to the ideal jet diameter, will ultimately lead to a perfectly uniform distribution. The correlation obtained for d_j as a function of X, Equation (5-4), is a necessary and very useful tool for designing FCNs. Even though this is strictly only valid for sharp-edged orifices, the mere fact that such a relationship exists at all is useful knowledge. In Appendix D this equation was adapted by adding the difference between d_j obtained from Equation (5-4) and d_j determined experimentally with the FCN using the profiled exit.

Figure 5-20 and Figure 5-21 compares three-dimensional graphs of one quadrant of the spray distributions of the prototype and commercial FCNs. From these graphs it would appear that the prototype nozzle delivers a much more even distribution. The large peak in the centre of the distribution of the commercial nozzle is an unwanted characteristic. In Figures 5-22 and 5-23 the same data used in Figure 5-20 and Figure 5-21 is used to generate contour plots of the two distributions. These figures clearly illustrate the improvement in distribution uniformity that is achieved with the prototype nozzle. Both distributions have some semblance to the ideal *square* spray pattern, though it is difficult to determine which spray pattern is more *square*.

CHAPTER SEVEN

NOZZLE MANUFACTURE

There are several manufacturing techniques that could be used in the production of cooling tower nozzles. There are numerous casting methods like the lost wax process, centrifugal die casting and permanent mould injection die casting. Casting is the most suitable tool for the manufacture of full cone nozzles, however, it may also be possible, if not too expensive, to machine the nozzle housings.

7.1 Plastic Injection Moulding

The manufacture of full cone nozzles for cooling towers lends itself to plastic injection moulding (PIM) and is the logical choice for such an assignment. The choice of plastic is the most important consideration in the design process. There are many excellent plastics available today, all with their own unique properties and limitations. Some of the properties that are listed for plastics today are heat, chemical and UV resistance, tensile strength, hardness, dielectric strength and flammability.

The choice of plastic for a cooling tower nozzle is governed by the operating conditions inside the cooling tower. These conditions include: moderate pressures, possibly high temperatures, 60 °C is regarded as high for plastic components, a certain amount of vibration. Often the water is highly chlorinated or being treated with some other chemicals making it essential to know the chemical resistance of the plastic material. The degree of vibration may promote the selection of an amorphous plastic above a plastic that has a crystalline structure.

There are many plastics suitable for use in a cooling tower environment, especially since chlorinated water is not normally used in cooling towers. The list of available plastics includes ABS, PA, POM, PC, PP, PVC, PBTP and PE. The choice of plastic should not be governed solely by cost but should rather be a decision based on functional requirements, e.g. if the maximum operating temperature, under the above conditions, of plastic A is 50 °C and of plastic B is 120 °C then plastic B should be chosen, even if plastic B is more expensive than

plastic A. The three plastics that go highly recommended for this application are ABS, POM and PC.

Once a suitable material has been found it is time to design the mould. Injection moulding and especially mould design is a highly specialised industry where years of experience is a decided advantage. For the inexperienced designer a sound mould cavity can be produced if common sense is used and if cognisance is taken of three important aspects of mould design.

First it is important to remember that, as a general rule, the maximum section thickness permissible with plastics is ±4 mm. A section that is too thick will result in the formation of voids or will warp, buckle and shrink. Second a well designed cooling and heating system is an essential part of the mould. Poor heating or too much cooling, anywhere in the mould, can cause premature freezing of the molten plastic which may result in thermal stresses or even fractures within the component. The cooling system ensures that component surfaces cool evenly thus leaving the surfaces smooth and flush. Thirdly the venting system should be designed in conjunction with the other elements of the mould and should not just be added to the mould as an afterthought. Sound venting ensures that the mould is completely filled during the injection process and therefore improves the quality of the final product.

Another aspect of mould design is the question of mould material. Moulds can either be made from high quality wear resistant steel or from case-hardenable steel. Steel moulds are cheaper to produce but can themselves only produce a limited number of castings, ±10 000. Two more factors which dramatically affect production costs are the specified dimensional tolerances and surface finish. A tolerance of ±0,1 mm is three times more expensive to produce than a tolerance of ±0,5 mm, while a specified surface roughness of 0,25 μm/m could result in production costs being up to ten times that required to manufacture to a finish of 6 μm/m.

7.2 Proposed Nozzle Design

The nozzle design presented here is a modular construction, which allows nozzle components to be interchanged to precipitate alternative performance characteristics. The fundamental element in the nozzle is the swirler. One swirler is the basis for a range of nozzles, i.e. for a

given swirl chamber diameter one swirler is manufactured while two or three final orifices can be inter-changed within the swirler to produce different nozzles. Each orifice is produced together with a central jet, which also fits into the single swirler.

Each nozzle is designed according to the requirements of its specific application. Typical requirements for a cooling tower nozzle will be rainfall intensity and nozzle installation data such as nozzle height above fill pack and the area requiring to be wetted. Appendix D contains a complete worked example on how to design a full cone nozzle. As far as actual manufacturing is concerned the following modular construction is proposed:

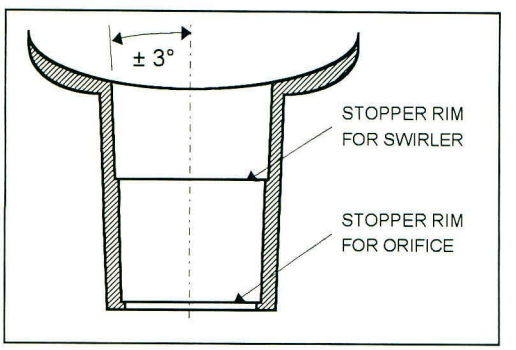

Figure 7 - 1: *Nozzle housing.*

- A basic housing is used for assembling between two and three nozzles with different orifice diameters, see Figure 7-1 for a diagram of the proposed housing design.

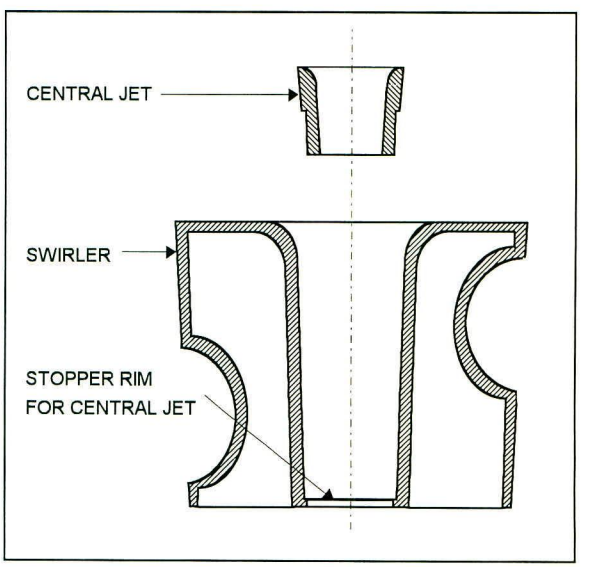

Figure 7 - 2: *Swirler and central jet.*

- The swirler is produced with a central cavity into which various central jets fit firmly. The cavity is the same shape as the one depicted in Figure 4-7, except that a taper must be included to facilitate the injection moulding. Figure 7-2 is a sectional view of the swirler and central jet.
- The orifice and rounded outlet will be manufactured as one unit. The orientation of the orifice within the nozzle is also important due to the fact that the *square* spray must be orientated to coincide with the tower fill pack. Figure 7-3 shows a cross-section of the proposed moulded orifice.
- The central jet is moulded to the exact length and diameter necessary to produce a uniform spray with the corresponding orifice. The central jet can either be glued or clipped into the central cavity of the swirler.

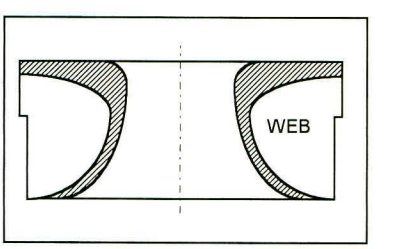

Figure 7 - 3: *Moulded orifice.*

CHAPTER EIGHT

CONCLUSIONS AND RECOMMENDATIONS

The primary objective for this project has been to design, test and correlate the behaviour of a large pressure jet atomiser for water distribution in a *square* spray pattern for use in industrial type cooling towers. This objective lead to theoretical and experimental examination of hollow and full-cone simplex swirl atomisers.

In many respects, however, it must be said that this thesis has only just scratched the surface as far as swirl spray atomisers are concerned. For instance, it is probable that the swirl port exit angle, γ, exerts a significant influence on the performance characteristics of the HCN and yet in this study only one swirler outlet angle of 41,5° was used throughout all of the experimental work.

Two more parameters, which have remained unchanged throughout this project, are inlet port area and number of ports. These parameters have a significant effect on spray uniformity. The balance between frictional loss caused by too many ports and spray non-uniformity caused by too few ports is an aspect, which has not been investigated. Also, the relationship between swirl port exit angle, γ, and swirl port length, l_p, is one that may well hold significant influence on the length and shape of the swirl chamber. The purpose of the swirl chamber is to damp out the separate streams from the swirl ports and thus ensure that a uniform liquid annulus will form in the final orifice. However, if γ could be chosen so that liquid would enter the swirl chamber with the exact velocity components needed at the exit to produce a specific spray cone angle and if the swirler could be constructed to deliver a semi-continuous liquid sheet into the swirl chamber, then swirl chambers could be designed a fifth of their current length. This would dramatically increase discharge coefficients allowing researchers to focus their efforts on refining the drop size distribution of sprays.

Experimental testing of existing cooling tower nozzles revealed that the performance of these nozzles was less than optimal, both with respect to distribution uniformity and required operating pressure. The claim that these nozzles produced a *square* spray pattern was also found wanting. The geometry of some of the swirlers in these nozzles was found to be of a rather crude design and it was clearly evident that the sharp edges and overhanging lips would

contribute to excessively high flow losses. Consequently it was decided to initiate this project by redesigning the swirler.

The new swirler was designed to have the same port area, A_p, and port entry angle, γ, as the sharp-edged swirler so that the behaviour of the two swirlers could be evaluated and compared through experimental testing. A theoretical analysis of the swirl port geometries lead to crude if not effective prediction of the loss coefficients associated with the ports. The loss coefficient predicted by this method more than three times greater for the sharp-edged swirler than for the streamlined swirler, a finding which was later validated through experimental work.

The testing of complete HCNs containing the different swirlers showed that required operating pressure can be significantly reduced for a given nozzle if a streamlined swirler is used. Having observed the advantages of using a streamlined swirler it was decided to complete the remaining experiments with nozzles embodying only the streamlined swirler.

Tests were conducted to determine the effect of the variation of orifice diameter, d_o, and nozzle supply pressure, P_n, on the performance characteristics of the HCN. These experiments showed that spray cone angle, 2θ, and film thickness, t, are not affected by variation in injection pressure but that discharge coefficient, C_n, has a marked dependence on the orifice Reynolds, Re_{do}. Equations from the work of Rizk and Lefebvre [85RI1] proved useful in obtaining correlations for film thickness and discharge coefficient.

By rounding the nozzle outlet it was found that the radial spray distribution could be *flattened out*, which is beneficial to the rainfall intensity distribution of the FCN. Knowledge gained from experiments done to quantify the effect of rounding the orifice outlet was used to design a profiled nozzle outlet that actually produces a *square* spray pattern.

FCN tests were then done to determine the effect of jet diameter, d_j, jet protrusion length, l_j, and orifice diameter, d_o, on the distribution uniformity of the tested nozzles. Results showed that a unique relationship exists between jet diameter and orifice diameter for any given jet protrusion length. This relationship was used to develop a code for designing FCNs for specific applications. Finally a complete FCN was tested and found to produce spray with uniform rainfall intensity distribution in the desired *square* spray pattern.

REFERENCES

[48TA1] Taylor, G.I., ***The Mechanics of Swirl Atomizers***, Proc. 7th Intern. Congr. Appl. Mech., Vol. 2, pp. 280 -285, 1948.

[50TA1] Taylor, G.I., ***The Boundary Layer in the Converging Nozzle of a Swirl Atomizer***, Quart. Journal of Mechanics and Applied Mathematics, Vol. 3, Pt. 2, pp. 129-139, 1950.

[60FO1] Foust, A.S., Wenzel, L.A., Clump, C.W., Maus, L. and Andersen, L.B., **Principles of Unit Operations**, John Wiley & Sons, New York, pp. 541-543, 1960.

[69DO1] Dombrowski, N. and Hasson, D., ***The Flow Characteristics of Swirl (Centrifugal) Spray Pressure Nozzles,*** AIChE Journal, Vol. 15, July, pp. 604-611, 1969.

[78SA1] Sada, E., Takahashi, K., Morikawa, K. and Ito, S., ***Drop Size Distribution by Full Cone Nozzle***, Canadian J. Chem. Eng., Vol. 56, pp. 455-459, August 1978.

[81BS1] British Standards Institution, **Methods of measurement of Fluid flow in closed conduits**, BS 1042: Section 1.1, pp. 33-39, 1981.

[82JO1] Jones, A.R., ***Design of Large Pressure Jet Atomiser for Power Plant***, ICLASS-82, pp. 181-185, 1982.

[83KR1] Kranc, S.C., ***The Effect of Non-uniform Water Distribution on Cooling Tower Performance,*** J. Energy, Vol. 7, no. 6, pp. 636-639, 1983.

[83SO1] Som, S.K., ***Theoretical and Experimental Studies on the Coefficient of Discharge and Spray Cone Angle of a Swirl Spray Pressure Nozzle Using a Power-Law Non-Newtonian Fluid,*** J. of Non-Newtonian Fluid Mechanics, Vol. 12, pp. 39-68, 1980.

[84WA1] Walzel, P., ***Design of Single Substance Pressure Atomizers,*** German Chem. Eng. Vol. 7, pp. 1-12, 1984.

[85RI1] Rizk, N.K. and Lefebvre, A.H., ***Internal Flow Characteristics of Simplex Swirl Atomizers,*** J. Propulsion, Vol. 1, No. 3, pp. 193-199, May-June, 1985.

[85SO1] Som, S.K. and Biswas, G., ***Dispersion of Spray from Swirl Nozzles,*** Department of Mech. Eng., Indian Institute of Technology, Kharagpur 721302 (India), pp. 191-200, 1985.

[86HO1] Horvay, M. and Leuckel, W., ***Experimental and Theoretical Investigation of Swirl Nozzles for Pressure-Jet Atomization***, Germ. Chem. Eng., Vol. 9. pp. 276-283, 1986.

[86WH1] White, F.M., **Fluid Mechanics,** International Edition, McGraw-Hill Book Co., Singapore, pp. 335-336, 1986.

[87PR1] Prywer, J and Kulesza, J., ***Jet-Centrifugal Atomizer in Application to Spray-Evaporative Condenser,*** Proc. 17th Intern. Congr. Refrig., Vienna, Austria, Vol. B, pp. 775-781, August 1987.

[87SC1] Schultz, T., ***The Estimated Effect of Uneven Water Distribution on the Performance of Cooling Tower Fills,*** B. Eng. Thesis, University of Stellenbosch, October 1989.

[88BE1] Bellagamba, B., Dinelli, G., Tognotti, L., Zanelli, S., ***Water Distribution in Cooling Towers: Characterisation of Industrial Spray Nozzles,*** Proc. Intern. Cooling Tower Conference (Proc. April 1989) Pisa, Italy, pp. 1.4: 1-10, 1988.

[89KR1] Kröger, D.G., **Cooling Tower Performance and Design,** Department of Mech. Eng., University of Stellenbosch, Stellenbosch, pp. A.9, 1989.

[89LE1] Lefebvre, A.H., **Atomization and Sprays,** Hemisphere Publishing Corporation, New York, pp. 5; 112-117; 165-189; 281-300, 1989.

[91MU1]Muschelknautz, E. and Trefz, M., **VDI-Wärmeatlas**, VDI-Verlag, Düsseldorf, 6. Aufl., pp. Lj1-Lj9, 1991.

[92DA1] Dahl, H.D. and Muschelknautz, E., ***Atomization of Liquids and Suspensions with Hollow Cone Nozzles,*** Chem. Eng. Technol. 15, pp. 224-231, 1992.

[93CH1] Chen, S.K., Lefebvre, A.H. and Rollbuhler, J., ***Factors Influencing the circumferential Liquid Distribution from Pressure-Swirl Atomizers,*** Trans. of ASME, Vol. 115, pp. 447-452, 1993.

[93DU1] Dumouchel, C., Bloor, M.I.G, Dombrowski, N., Ingham, D.B. and Ledoux, M., ***Viscous Flow in a Swirl Atomizer,*** Chem. Eng. Sci., Vol. 48, No. 1, pp. 81-87, 1993.

[93KO1] Koo, Y.M. and Kuhlman, D.K., ***Theoretical Spray Performance of Swirl-Type Nozzles,*** Trans. of ASAE, Vol. 36, pp. 671-678, May-June, 1993.

[93KO2] Koo, Y.M. and Kuhlman, D.K., ***Spray Performance Models of a Designed Swirl Nozzle,*** Trans. of ASAE, Vol. 36, pp. 679-684, May-June, 1993.

[93KR1] Kranc, S.C., ***Performance of Counterflow Cooling Towers with Structured Packings and Maldistributed Water Flow,*** Numerical Heat Transfer, Part A, Vol. 23, pp. 115-27, 1993.

[93LA1] Lake, P., ***Spray Distributions under Medium Pressure Nozzles for Cooling Towers,*** B. Eng. Thesis, University of Stellenbosch, November 1993.

APPENDIX A

PHYSICAL PROPERTIES OF WATER

The following two equations for calculating water density and absolute viscosity are taken from Kröger [83KR1].

Saturated water liquid from 273,15 K to 380 K.

Density:

$$\rho = (a + bT + cT^2 + dT^6)^{-1}: \text{kg/m}^3 \qquad \text{(A-1)}$$

where:

$a = 1{,}49343\times10^{-3}$

$b = -3{,}7164\times10^{-6}$

$c = 7{,}09782\times10^{-9}$

$d = -1{,}90321\times10^{-20}$

Absolute Viscosity:

$$\mu = a\times10^{b/(T-c)}: \text{kg/ms} \qquad \text{(A-2)}$$

where:

$a = 2{,}414\times10^{-5}$

$b = 247{,}8$

$c = 140$

APPENDIX B

SAMPLE CALCULATIONS

The purpose of this appendix is to show the reader how the various formulas and calculation methods were implemented in obtaining the data for the numerous graphs of Chapter 5 and Chapter 6. An attempt has been made to present the calculations in the order in which the relevant equations appear in the thesis. Unless otherwise stated the following conditions will apply to all the sample calculations:

- water temperature: 30 °C (≈ 303 K)
- supply pressure manometer reading: 25 cm Hg
- flow meter manometer reading: 14,5 cm Hg
- A_p: 932 mm²; d_s: 68,3 mm; d_o: 37,2 mm; l_s: 68,3 mm; l_o: 3 mm; d_p: 16 mm; l_p: 72 mm

Refer to Figure 2-1 for a recap of where these various dimension apply.

B.1 Calculation of Mass Flow Rate

The most important calculation is to calculate the actual mass flow rate from the reading on the flow meter manometer. To do this we must first calculate the water density and viscosity from the equations given in Appendix A.

The density of water at 303 K is calculated from Equation (A-1):

$$\rho = (1{,}49343\times10^{-3} - 3{,}7164\times10^{-6}\times303 + 7{,}09782\times10^{-9}\times303^2 - 1{,}90321\times10^{-20}\times303^6)^{-1}$$
$$= 995{,}7\ \text{kg/m}^3.$$

The absolute viscosity of water at 303 K is calculated from Equation (A-2):

$$\mu = 2{,}414\times10^{-5}\times10^{\left(\frac{247{,}8}{303-140}\right)}$$
$$= 7{,}998\times10^{-4}\ \text{kg/ms}.$$

The pressure drop across the orifice is calculated from the following equation:

$$\Delta P = (\rho_{Hg} - \rho)g\,h, \qquad \text{(B-1)}$$

where g is taken as 9,796 m/s² and ρ_{Hg} is taken as 13 550 kg/m³.

Substituting into Equation (B-1) we obtain the flow meter pressure drop in Pascal:

$$\Delta P_{fm} = (13\,550 - 995{,}7)\times 9{,}796\times 0{,}145$$
$$= 17\,832 \text{ Pa.}$$

The flow rate can now be determined iteratively with the following routine.

1. Guess the pipe Reynolds number for the flow leading up to the flow meter orifice.
2. Calculate the discharge coefficient, C_d, from the Stoltz equation:

$$C_d = 0{,}5959 + 0{,}0312\beta^{2{,}1} - 0{,}184\beta^8 + 0{,}0029\beta^{2{,}5}\left[\frac{10^6}{Re_D}\right]^{0{,}75} + \\ + 0{,}09\beta^4\left(1-\beta^4\right)^{-1} - 0{,}0337\times 0{,}47\beta^3. \qquad \text{(B-2)}$$

3. Calculate the mass flow rate from the following equation:

$$\dot{m} = C_d \rho A_t \sqrt{\frac{2\Delta P_{fm}}{\rho\left(1-\beta^4\right)}}, \qquad \text{(B-3)}$$

where A_t refers to the throat area of the orifice plate.

4. Calculate a new pipe Reynolds number based on the calculated flow rate and use this Reynolds number to re-calculate C_d from Equation (B-2).
5. Repeat until the Re_D at step 2. and the Re_D at step 4. differ only by a selected tolerance.

For this sample calculation we shall use an already converged solution for Re_D as the initial guess in 1. Therefore, substituting $Re_D = 118\,988$ into Equation (B-2) we obtain:

$$C_d = 0{,}5959 + 0{,}0312\times 0{,}68^{2{,}1} - 0{,}184\times 0{,}68^8 + 0{,}0029\times 0{,}68^{2{,}5}\left[\frac{10^6}{118\,988}\right]^{0{,}75} + \\ + 0{,}039\times 0{,}68^4\left(1-0{,}68^4\right)^{-1} - 0{,}0337\times 0{,}47\times 0{,}68^3$$
$$= 0{,}61245.$$

Calculate the flow rate from Equation (B-3):

$$\dot{m} = 0{,}61245\times 995{,}7\times \pi 0{,}017^2\sqrt{\frac{2\times 17832}{995{,}7\left(1-0{,}68^4\right)}}$$
$$= 3{,}737 \text{ kg/s.}$$

The new Re_D is obtained from the following equation:

$$Re_D = \frac{4\dot{m}}{\pi D\mu}. \qquad \text{(B-4)}$$

Substituting into Equation (B-4) we obtain:

$$Re_D = \frac{4 \times 3{,}737}{\pi\, 0{,}05 \times 7{,}998 \times 10^{-4}}$$
$$= 118\,982,$$

which only differs from the initial guess by 0,005 percent. Therefore, the calculated mass flow rate of 3,737 kg/s is correct.

B.2 Calculation of Swirl Port Velocity

The velocity through a port is calculated from the measured mass flows, while the predicted velocities are calculated from the estimated loss coefficients using Equation (3-3). For an example of how these values are calculated take the actual test conditions:

- the water temperature is 55° C, therefore from Equation (A-1) $\rho = 985{,}8$ kg/m^3
- the pressure drop across the swirler is 25,23 kPa
- the total mass flow rate is 5,65 kg/s.

The predicted port velocity for the streamlined swirler is calculated from Equation (3-3):

$$U_{ep} = \sqrt{\frac{2 \times 25230}{985{,}8 \times [0{,}4 + 1]}}$$
$$= 6{,}047 \text{ m/s},$$

while the actual measured port velocity is calculated from the continuity equation:

$$U_e = \frac{\dot{m}}{\rho A_p}$$
$$= \frac{5{,}65}{985{,}8 \times 932 \times 10^{-6}}$$
$$= 6{,}149 \text{ m/s}.$$

Rearranging Equation (3-1) the actual loss coefficient can also be calculated:

$$\sum F_i = \frac{2\Delta P_{sw}}{\rho U_e^{\,2}} - 1$$
$$= \frac{2 \times 25230}{985{,}8 \times 6{,}149^2} - 1$$
$$= 0{,}354,$$

which is close to the original estimate.

B.3 Calculation of Spray Cone Angle

First the nozzle supply pressure is calculated from Equation (B-1):

$$\Delta P_n = (13\ 550 - 995{,}7)\times 9{,}796\times 0{,}28$$
$$= 34\ 435 \text{ Pa.}$$

The first calculation of spray cone angle is from the formula of Taylor [48TA1]. Due to the nature of the relationship between K, y and C_n, it is first necessary to iterate to find the value of y that yields a C_n from Equation (3-24) which will then correspond to the correct value of K. In this example the value of K is:

$$K = \frac{932}{68{,}3 \times 37{,}2}$$
$$= 0{,}367.$$

In order to shorten this process we shall demonstrate that a value of y = 0,5904 will yield the above K. Start by calculating z^2 from Equation (3-7) by substituting y = 0,5904:

$$z^2 = \frac{0{,}5904^2}{4} + \sqrt{\frac{0{,}5904^4}{16} + \frac{0{,}5904^2}{2}}$$
$$= 0{,}5136$$
$$\therefore z = 0{,}7167.$$

Substitute into Equation (3-24) and obtain the unknown discharge coefficient:

$$C_d = (1 - 0{,}5136)\sqrt{1 - \frac{0{,}5904^2}{0{,}5136}}$$
$$= 0{,}2757.$$

Now substitute the above values into Equation (3-8):

$$K = \frac{\pi 0{,}2757}{4 \times 0{,}5904}$$
$$= 0{,}367,$$

which is the value calculated earlier.

The value of x is calculated by manipulating Equation (3-6):

$$x^2 = 1 - \frac{y^2}{z^2}$$
$$\therefore x = \sqrt{1 - \frac{0{,}5904^2}{0{,}5136}}$$
$$= 0{,}5668.$$

The spray cone angle is now calculated by substituting for x, y, z and z^2 into Equation (3-5):

$$\cos\theta = 0{,}5668 + \frac{0{,}5904\sqrt{2} \times 0{,}5136}{(1-0{,}5136)^{\frac{3}{2}}}\left[\frac{1}{2}\left(\frac{1}{0{,}5136}-1\right)+\log_e 0{,}7167\right]$$

$$= 0{,}744$$

$$\therefore 2\theta = 2\cos^{-1}(0{,}744)$$

$$= 83{,}8\ ^\circ.$$

The method of Dahl and Muschelknautz [92DA1] required iteration in order to calculate w_o from Equation (3-9), this was due to the fact that the wall friction coefficient is a function of the mean Reynolds number which in turn is also related to w_o. The final iteration yielded a value for w_o of 5,298 m/s, which was based on the actual measured mass flow rate through the nozzle. First the port entry velocity, U_e, is again calculated from continuity:

$$U_e = \frac{3{,}737}{995{,}74 \times 932 \times 10^{-6}}$$

$$= 4{,}027\ \text{m/s}.$$

Next Re_m is calculated as follows:

$$Re_m = \frac{\rho\left(\frac{U_e \sin(\gamma) + w_o}{2}\right)\left(\frac{r_s + r_o}{2}\right)}{\mu}$$

$$= \frac{995{,}7\left(\frac{4{,}027\sin(41{,}5^\circ)+5{,}298}{2}\right)\left(\frac{0{,}03415+0{,}0186}{2}\right)}{7{,}998\times10^{-4}}$$

$$= 176911,$$

where $U_e\sin(\gamma)$ is the tangential component of the port entry velocity. The value of λ which corresponds to this Reynolds number is 0,0034. The frictional area is calculated as follows:

$$A_\tau \approx \pi d_s l_s + 4\pi l_p d_p + \frac{\pi\left(d_s^{\,2} - d_o^{\,2}\right)}{4}$$

$$= \pi 0{,}0683 \times 0{,}0683 + 4\pi 0{,}072 \times 0{,}016 + \frac{\pi\left(0{,}0683^2 - 0{,}0372^2\right)}{4}$$

$$= 0{,}03171\ \text{m}^2.$$

The volume flow rate and entry radius are calculated as follows:

$$\dot{q} = \frac{\dot{m}}{\rho}$$
$$= \frac{3,737}{995,7}$$
$$= 0,003753\ m^3/s$$

and

$$r_e = r_s - r_p$$
$$= 34,15 - 8$$
$$= 26,15\ mm.$$

Substitute the relevant values into Equation (3-9) to obtain w_o:

$$w_o = \frac{4,027\frac{26,15}{18,6}}{1+\frac{0,0034}{2}\frac{0,03171\times 4,027}{0,003753}\sqrt{\frac{26,15}{18,6}}}$$
$$= 5,298\ m/s.$$

The average velocity through the final orifice is calculated from Equation (3-14):

$$U_o = \frac{0,003753}{\pi\, 0,0186^2}$$
$$= 3,453\ m/s.$$

Converting w_o to dimensionless form:

$$W_o = \frac{w_o}{U_o}$$
$$= \frac{5,298}{3,453}$$
$$= 1,534$$

and solving Equation (3-11) with n = 1 we obtain $V_o = 1,807$, or $v_o = 6,24$ m/s.

Next the dimensionless axial velocity leaving the nozzle is calculated from Equation (3-15):

$$V_a^{\,2} = 1,807^2 + \frac{1}{1}1,534^2\left[\left(\frac{1,807}{1,807-1}\right)^1 - 1\right]$$
$$\therefore V_a = 2,486$$

and the dimensionless mean axial velocity is obtained from Equation (3-16) as follows:

$$\overline{V} = \sqrt{\frac{1,807^2 + 2,486^2}{2}}$$
$$= 2,173.$$

The mean axial velocity in metres per second is:

$$\begin{aligned}\overline{v} &= \overline{V} \times U_o \\ &= 2{,}173 \times 3{,}453 \\ &= 7{,}505 \text{ m/s}.\end{aligned}$$

From Equation (3-17) we obtain the film thickness

$$\begin{aligned}t &= 0{,}0186 - \sqrt{0{,}0186^2 - \frac{0{,}003753}{\pi\, 6{,}24}} \\ &= 0{,}0062 \text{ m}\end{aligned}$$

which when substituted into Equation (3-18) yields the total velocity of the liquid sheet:

$$\begin{aligned}U_a &= \sqrt{7{,}505^2 + 5{,}298^2\left(\frac{0{,}0186}{0{,}0186 - 0{,}00617}\right)^1} \\ &= 9{,}916 \text{ m/s}.\end{aligned}$$

Finally the spray cone angle is obtained from Equation (3-19):

$$\begin{aligned}2\theta &= 2\cos^{-1}\left(\frac{7{,}505}{9{,}916}\right) \\ &= 81{,}62\,^\circ.\end{aligned}$$

In order to use the correlations of Som [83SO1], Equation (3-20) and Equation (3-26) the generalised inlet Reynolds number, Re_{gi}, must first be calculated from the following equation:

$$Re_{gi} = \frac{\rho U_e \sin\gamma\, d_s}{\mu}. \qquad \text{(B-5)}$$

Therefore, substituting into Equation (B-5) we obtain:

$$\begin{aligned}Re_{gi} &= \frac{995{,}7 \times 4{,}027 \times \sin(41{,}5^\circ) \times 0{,}0683}{7{,}998 \times 10^{-4}} \\ &= 226892,\end{aligned}$$

which when substituted into Equation (3-20) yields:

$$\begin{aligned}2\theta &= \frac{77{,}260(37{,}2/68{,}3)^{0{,}3153}(\pi)^{0{,}1949}}{(68{,}3/68{,}3)^{0{,}0611}}\left[1 - e^{(-8{,}695\times10^{-5})226\,892}\right] \\ &= 79{,}74^\circ.\end{aligned}$$

B.4 Calculation of Discharge Coefficient

The experimental testing of nozzle discharge coefficient was done at nozzle supply pressures other than 34,4 kPa and since Figure 5-6 compares the test data at 28 kPa with the various other correlations from Chapter 3 it is appropriate to provide sample calculations at this pressure. The mass flow rate through the nozzle with K = 0,367 at a pressure of 28 kPa is 3,33 kg/s. The actual discharge coefficient is calculated from Equation (3-23) as follows:

$$\therefore C_n = \frac{3,33}{995,7\pi 0,0186^2\sqrt{\frac{2\times 28000}{995,7}}}$$
$$= 0,4125.$$

The prediction of C_n from Equation (3-24) has already been calculated on page B3, the value obtained was 0,2757. The first sample calculation to be done here will be for Equation (3-25). First the pressure velocity, U_p, is calculated:

$$U_p = \sqrt{\frac{2\times 28000}{995,7}}$$
$$= 7,46\,\text{m/s},$$

which when substituted together with the other relevant values into Equation (3-25) yields:

$$C_n = 0,45\left(\frac{995,7\times 7,46\times 0,0372}{7,998\times 10^{-4}}\right)^{-0,02}\left(\frac{3}{37,2}\right)^{-0,03}\left(\frac{68,3}{68,3}\right)^{0,05} 0,367^{0,52}\left(\frac{68,3}{37,2}\right)^{0,23}$$
$$= 0,2567.$$

From Equation (3-26) we obtain a value for C_n of:

$$C_n = \frac{3,377(1)^{1,520}(68,3/68,3)^{0,117}}{(226892)^{0,347}(37,2/68,3)^{1,166}(\pi)^{0,274}}$$
$$= 0,0694,$$

while the correlation of Rizk and Lefebvre [85RI1], Equation (3-27), yields the following solution for discharge coefficient:

$$C_n = 0,35\times 0,367^{0,5}(68,3/37,2)^{0,25}$$
$$= 0,2467.$$

Equation (5-1) which was modelled on Equation (3-27) predicts C_n as follows:

$$C_n = 0{,}578 \times 0{,}367^{0{,}5}\left(68{,}3/37{,}2\right)^{0{,}25}$$
$$= 0{,}4075,$$

which is within 1,23 percent of the measured value. The coefficient of this equation was calculated from the following equation:

$$B_f = \sum_{i=1}^{n} \frac{C_{ni}}{K_i^{0{,}5}\left(d_s/d_{oi}\right)^{0{,}25}}, \qquad \text{(B-6)}$$

where n is the total number of data points and B_f is the unknown coefficient. B_f is in effect the average of all the individual constants which could be calculated for each measured discharge coefficient, C_{ni}. In calculating B_f, the data from the nozzle with K = 0,632 was excluded for two reasons. Firstly, looking at the general trend of the data in Figure 5-6 and Figure 5-7 it appears that discharge coefficient falls away for nozzles with K values in excess of 0,51, while for K values less than 0,51 the trend is more linear. Secondly, from a design perspective there is no problem in only correlating C_n for lesser values of K since it is in this range that cooling tower nozzles are usually designed. Therefore, by substituting the data, obtained at the four injection pressures, from the remaining six nozzles, into Equation (B-5) the value of $B_f = 0{,}578$ was obtained.

The orifice Reynolds number at 28 kPa is calculated based on the pressure velocity:

$$Re_{do} = \frac{\rho U_p d_o}{\mu}$$
$$= \frac{995{,}7 \times 7{,}46 \times 0{,}0372}{7{,}998 \times 10^{-4}}$$
$$= 345499.$$

This Reynolds number is used to calculate C_n from Equation (5-2):

$$C_n = 1{,}468 \times 345499^{-0{,}067}0{,}367^{0{,}5}\left(68{,}3/37{,}2\right)^{0{,}125}$$
$$= 0{,}4082,$$

which is within 1,06 percent of the measured value.

The exponent of Re_{do} in Equation (5-2) was chosen in such a way as to yield a minimum value for the following dimensionless equation:

$$\sigma = \frac{STD\left(B_{\sigma i}\right)}{AVG\left(B_{\sigma i}\right)}, \qquad \text{(B-7)}$$

where STD refers to standard deviation and AVG is the average. The values of $B_{\sigma i}$ are calculated from an equation not unlike Equation (B-5):

$$B_{\sigma i} = \frac{C_{ni}}{Re_{doi}^{-0,067} K_i^{0,5} \left(d_s / d_{oi}\right)^{0,125}}. \qquad \text{(B-8)}$$

The coefficient in Equation (5-2) is the average of all the $B_{\sigma i}$ values. Once again only the data from nozzles with K values less than 0,51 was used in obtaining this equation.

B.5 Film Thickness Calculations

The sample calculations for film thickness which coincide with the formulas of Chapter 3 are as follows. Firstly we shall note that the measured film thickness is 13,8 mm. From Equation (3-28), which is a prediction of t using Taylor's [48TA1] theory:

$$t = 0,0186(1 - 0,7167)$$
$$= 0,0053 \text{ m} \left(\text{or } 5,3 \text{ mm}\right).$$

From Equation (3-31) we obtain:

$$t = 0,0186 - \sqrt{0,0186^2 - \frac{0,003753}{\pi 6,24}}$$
$$= 0,0062 \text{ m} \left(\text{or } 6,2 \text{ mm}\right).$$

The flow number, FN, which must be calculated in order to use Equation (3-32) and Equation (3-33) is calculated from Equation (3-34):

$$FN = \frac{3,33}{\sqrt{995,7 \times 28\,000}}$$
$$= 631 \times 10^{-6} \text{ m}^2.$$

The value of t that satisfies Equation (3-32) is t = 0,0052 m, to demonstrate this substitute for t and calculate both the left hand side, LHS, and right hand side, RHS, of the equation.

$$LHS = 0,0052^2$$
$$= 2,7 \times 10^{-5} \text{ m}^2.$$

To calculate the RHS the ratio of air-core area to orifice area, X, must first be calculated:

$$X = \frac{(d_o - 2t)^2}{d_o^2}$$

$$= \frac{(0{,}0372 - 2 \times 0{,}0052)^2}{0{,}0372^2}$$

$$= 0{,}5217.$$

Substituting into the RHS of Equation (3-32) yields:

$$RHS = \frac{1560 \times 631 \times 10^{-6} \times 7{,}998 \times 10^{-4}}{\sqrt{995{,}7 \times 28000} \times 0{,}0372} \frac{1 + 0{,}5217}{(1 - 0{,}5217)^2}$$

$$= 2{,}7 \times 10^{-5}\ m^2.$$

Since the LHS and RHS are equal, t = 0,0052 m is the solution to Equation (3-32).

The film thickness obtained from Equation (3-33) is not much different from the value obtained above:

$$t = 3{,}66\left[\frac{0{,}0372 \times 631 \times 10^{-6} \times 7{,}998 \times 10^{-4}}{\sqrt{995{,}7 \times 28000}}\right]^{0{,}25}$$

$$= 0{,}0050\ m\ (\text{or } 5{,}0\ mm).$$

Equation (5-3), which was derived from Equation (3-33) gives the following estimate for t:

$$t = 9{,}81\left[\frac{0{,}0372 \times 631 \times 10^{-6} \times 7{,}998 \times 10^{-4}}{\sqrt{995{,}7 \times 28000}}\right]^{0{,}25}$$

$$= 0{,}0135\ m\ (\text{or } 13{,}5\ mm),$$

which only differs from the measured value by 2,4 percent. The coefficient of this equation was calculated from the following equation:

$$B_t = \sum_{i=1}^{n} \frac{t_i}{\left[\frac{d_{oi} F N_i \mu}{\sqrt{\rho \Delta P_n}}\right]^{0{,}25}} \Big/ n, \qquad \text{(B-9)}$$

where B_t is the unknown coefficient and n is the total number of data points. For this calculation there were only five data points which resulted in a value for B_t of 9,81.

B.6 Calculation of Rainfall Intensity

The calculation of rainfall intensity, I, is a basic operation which involves the area of the sampler cylinder, A_{rs}, and the mass flow rate of water. Take for example a distribution test which lasted 3 minutes and the mass of water collected in one particular sampler was 2,34 kg. Since rainfall intensity is traditionally measured in terms of kilograms per square metre per second, I must be calculated as follows. First the mass flow rate through the sampler, $\dot{m}_{rs}$, is calculated:

$$\begin{aligned}\dot{m}_{rs} &= \frac{m_{rs}}{\Delta t} \\ &= \frac{2,34}{3 \times 60} \\ &= 0,013 \text{ kg/s},\end{aligned}$$

from which the intensity for this specific sampler can then be calculated:

$$\begin{aligned}I_{rs} &= \frac{\dot{m}_{rs}}{A_{rs}} \\ &= \frac{0,013}{\pi 0,045^2/4} \\ &= 8,17 \text{ kg/m}^2\text{s}.\end{aligned}$$

B.7 Calculation of Swirler Pressure Drop in HCN

The swirler pressure drop is calculated from Equation (6-5), however, due to the implicit nature of this equation, F_{sw} being itself a function of ΔP_{sw}, iteration is required to solve it. Take for example a nozzle using the sharp swirler and operating at a supply pressure of 50 kPa. Characteristic dimensions are: $d_s = 68,3$ mm², $d_o = 37,2$ mm and $A_p = 932$ mm², therefore $K = 0,367$. The solution is $\Delta P_{sw} = 28,984$ kPa. To demonstrate this, calculate U_e and F_{sw} and substitute into Equation (6-5). From the definition of C_n:

$$\begin{aligned}\dot{m} &= \rho U_e A_p \\ &= \rho U_p A_o C_n\end{aligned}$$

$$\therefore U_e = \frac{U_p A_o C_n}{A_p}, \qquad \text{(B-10)}$$

where C_n is calculated from Equation (5-2). Therefore, assuming $\rho = 1000$ kg/m³ and $\mu = 0,001$ kg/ms calculate U_p and Re_{do}:

$$U_p = \sqrt{\frac{2 \times 50\,000}{1000}}$$
$$= 10 \text{ m/s}$$

and

$$Re_{do} = \frac{1000 \times 10 \times 0{,}0372}{0{,}001}$$
$$= 372\,000.$$

Calculating C_n:

$$C_n = 1{,}468 \times 372\,000^{-0{,}067} 0{,}367^{0{,}5} \left(68{,}3/37{,}2\right)^{0{,}125}$$
$$= 0{,}4062$$

and then U_e:

$$\therefore U_e = \frac{10 \times \pi 0{,}0372^2 \times 0{,}4062}{932 \times 10^{-6}}$$
$$= 4{,}734 \text{ m/s}.$$

From Equation (6-4):

$$F_{sw} = 27{,}2 \times 29894^{-0{,}942} + 0{,}556$$
$$= 1{,}664,$$

which when substituted into Equation (6-5) yields:

$$\Delta P_{sw} = 1/2 \times 4{,}734^2 \left(1{,}664 + 1\right)$$
$$= 29894 \text{ Pa},$$

which is the same value used to initiate this example.

EXPERIMENTAL DATA

Conditions:

P_n [kPa]	$\dot{m}$ [kg/s]	h [cm]	T_w [°C]	d_o [mm]	d_j [mm]	l_j [mm]	ϕ_n [°]
79.3	3.93	26.5	29	37.2	0	0	sharp

y [cm] \ x [cm]	0	8	16	24	32	40	48
0	0.25	0.50	1.82	5.85	11.19	5.66	0.88
8	0.44	0.82	2.70	6.79	11.51	4.53	0.75
16	1.89	2.77	5.47	9.75	10.19	2.33	0.57
24	6.22	7.48	9.68	11.51	4.84	1.13	0.19
32	11.25	11.57	9.62	4.28	1.32	0.38	--
40	5.03	3.96	2.20	0.94	0.38	0.13	--
48	0.88	0.75	0.50	0.25	0.06	--	--

Table C - 1: *RID [kg/m²s] of HCN with sharp-edged swirler.*

Conditions:

P_n [kPa]	$\dot{m}$ [kg/s]	h [cm]	T_w [°C]	d_o [mm]	d_j [mm]	l_j [mm]	ϕ_n [°]
61.5	3.87	26.5	34	37.2	0	0	sharp

y [cm] \ x [cm]	0	8	16	24	32	40	48	56
0	0.00	0.00	0.08	0.75	2.06	1.43	0.31	0.07
8	0.00	0.02	0.21	0.99	2.27	1.19	0.27	0.06
16	0.17	0.25	0.72	1.74	2.26	0.74	0.18	0.05
24	0.96	1.14	1.77	2.33	1.18	0.34	0.10	0.03
32	2.29	2.35	2.10	1.15	0.44	0.15	0.05	0.02
40	1.18	0.95	0.64	0.33	0.15	0.06	0.02	0.01
48	0.28	0.23	0.17	0.10	0.05	0.02	0.01	0.01
56	0.07	0.06	0.04	0.03	0.02	0.01	--	--

Table C - 2: *RID [kg/m²s] of HCN with streamlined swirler.*

Conditions:

P_n [kPa]	$\dot{m}$ [kg/s]	h [cm]	T_w [°C]	d_o [mm]	d_j [mm]	l_j [mm]	ϕ_n [°]
30.7	3.74	29	24.5	37.2	16	0	sharp

y [cm] \ x [cm]	0	8	16	24	32	40	48
0	9.64	10.53	10.22	8.65	12.21	8.49	0.73
8	10.37	10.53	9.59	8.44	13.20	6.97	0.52
16	8.96	8.96	8.38	8.38	12.63	4.51	0.31
24	7.18	7.44	7.60	8.23	10.16	2.72	0.21
32	11.27	10.37	9.48	8.38	6.71	1.52	0.10
40	6.18	5.13	4.14	3.25	2.10	0.58	0.05
48	0.52	0.47	0.42	0.42	0.31	0.16	--

Table C - 3: *RID [kg/m²s] of FCN with sharp-edged orifice.*

Conditions:

P_n [kPa]	$\dot{m}$ [kg/s]	h [cm]	T_w [°C]	d_o [mm]	d_j [mm]	l_j [mm]	ϕ_n [°]
30.7	5.07	27	30.5	37.2	13.5	10	130

x [cm] / y [cm]	0	8	16	24	32	40	48
0	8.75	8.54	7.65	6.97	7.81	8.02	2.93
8	9.43	8.33	7.60	7.60	8.49	7.49	2.67
16	7.65	6.92	6.81	8.28	9.12	5.71	1.47
24	6.34	6.08	7.34	9.75	8.02	2.57	3.67
32	7.44	7.65	9.01	8.02	2.93	0.58	--
40	7.81	7.49	5.45	2.10	0.47	--	--
48	2.83	1.78	0.84	0.21	--	--	--

Table C - 4: *RID [kg/m²s] of FCN with protruding central jet.*

Conditions:

P_n [kPa]	$\dot{m}$ [kg/s]	h [cm]	T_w [°C]	d_o [mm]	d_j [mm]	l_j [mm]	ϕ_n [°]
24.6	4.76	27	30	37.2	14.5	10	130

x [cm] / y [cm]	0	8	16	24	32	40	48
0	7.71	8.47	8.34	7.42	7.84	6.71	1.89
8	9.35	8.84	8.09	7.67	8.22	6.04	1.76
16	9.18	7.63	7.55	8.59	8.51	4.15	0.84
24	7.63	7.17	7.92	9.26	6.12	1.38	0.21
32	8.63	8.59	8.89	5.95	1.72	0.25	--
40	7.00	6.04	3.60	1.09	0.25	0.13	--
48	1.72	1.05	0.38	0.08	--	--	--

Table C - 5: *RID [kg/m²s] of FCN with protruding central jet.*

Conditions:

P_n [kPa]	$\dot{m}$ [kg/s]	h [cm]	T_w [°C]	d_o [mm]	d_j [mm]	l_j [mm]	ϕ_n [°]
61.5	6.63	26.5	34	37.2	12 to 17	0	130

x[cm] / y[cm]	0	8	16	24	32	40	48	56	64
0	1.77	1.61	1.59	1.88	2.21	1.74	0.88	0.36	0.15
8	1.50	1.46	1.63	1.92	2.16	1.63	0.82	0.34	0.13
16	1.62	1.61	1.82	2.12	2.09	1.37	0.64	0.27	0.11
24	2.01	1.97	2.09	2.13	1.67	0.97	0.44	0.19	0.09
32	2.19	2.12	2.00	1.67	1.09	0.60	0.29	0.13	0.05
40	1.67	1.51	1.29	0.95	0.58	0.32	0.16	0.08	0.04
48	0.83	0.74	0.60	0.43	0.28	0.16	0.09	0.05	0.02
56	0.37	0.32	0.26	0.19	0.12	0.08	0.04	0.02	0.01
64	0.15	0.13	0.10	0.08	0.06	0.04	0.02	0.02	0.01

Table C - 6: *RID [kg/m²s] of FCN with diffusing central jet.*

Conditions:

P_n [kPa]	$\dot{m}$ [kg/s]	h [cm]	T_w [°C]	d_o [mm]	d_j [mm]	l_j [mm]	ϕ_n [°]
27.1	4.60	26.5	29	37.2	17	0	130

x [cm] / y [cm]	0	8	16	24	32	40	48	56
0	5.24	4.85	4.82	5.74	6.76	5.89	2.88	1.15
8	4.93	4.69	5.00	6.03	6.84	5.71	2.67	1.02
16	5.08	5.00	5.55	6.68	6.99	4.82	2.17	0.84
24	5.84	5.84	6.42	7.02	5.95	3.56	1.57	0.60
32	6.55	6.55	6.65	5.92	4.01	2.07	0.89	0.37
40	6.03	5.66	4.74	3.46	1.94	1.07	0.47	0.13
48	3.27	2.93	2.44	1.65	1.00	0.52	0.21	0.08
56	1.34	1.18	0.94	0.65	0.37	0.21	0.08	--

Table C - 7: *RID [kg/m²s] of FCN with diffusing central jet.*

Conditions:

P_n [kPa]	$\dot{m}$ [kg/s]	h [cm]	T_w [°C]	d_o [mm]	d_j [mm]	l_j [mm]	ϕ_n [°]
105.8	8.44	26.5	28.5	37.2	12 to 17	0	130

x[cm] / y[cm]	0	8	16	24	32	40	48	56	64
0	5.99	5.83	6.92	9.47	11.86	10.10	5.49	2.47	1.01
8	5.99	6.04	7.29	10.23	12.20	9.81	5.11	2.22	0.92
16	7.13	7.42	9.05	11.69	12.03	8.30	4.19	1.80	0.75
24	9.89	10.19	11.53	12.32	10.40	6.33	3.10	1.43	0.59
32	12.49	12.28	11.99	10.23	7.17	4.11	2.10	0.96	0.46
40	10.61	9.98	8.55	6.37	4.02	2.31	1.22	0.63	0.29
48	5.95	5.37	4.40	3.31	2.18	1.26	0.71	0.38	0.21
56	2.64	2.43	1.93	1.43	0.96	0.63	0.38	0.25	0.13
64	1.13	0.96	0.92	0.71	0.50	0.34	0.21	0.17	--

Table C - 8: *RID [kg/m²s] of FCN with diffusing central jet.*

Conditions:

P_n [kPa]	$\dot{m}$ [kg/s]	h [cm]	T_w [°C]	d_o [mm]	d_j [mm]	l_j [mm]	ϕ_n [°]
32.0	4.6	26.5	31	37.2	12 to 17	0	sharp

x[cm] / y[cm]	0	8	16	24	32	40	48	56	64
0	3.56	2.93	2.81	2.91	3.40	3.94	3.77	2.62	1.32
8	3.25	2.72	2.64	2.96	3.35	3.92	3.86	2.58	1.30
16	3.12	2.87	2.93	3.25	3.69	4.00	3.42	2.12	1.03
24	3.31	3.19	3.40	3.77	4.09	3.84	2.87	1.63	0.78
32	3.90	3.81	4.07	4.21	4.05	3.31	2.12	1.11	0.52
40	4.38	4.36	4.30	3.98	3.16	2.16	1.26	0.63	0.27
48	4.17	3.94	3.48	2.83	2.03	1.30	0.75	0.38	0.13
56	2.56	2.35	2.05	1.57	1.09	0.69	0.38	0.19	--
64	1.11	1.05	0.88	0.67	0.44	0.23	0.13	--	--

Table C - 9: *RID [kg/m²s] of FCN with diffusing central jet.*

Conditions:

P_n [kPa]	$\dot{m}$ [kg/s]	h [cm]	T_w [°C]	d_o [mm]	d_j [mm]	l_j [mm]	ϕ_n [°]
61.5	6.92	26.5	34	37.2	17	0	sharp

x[cm] / y[cm]	0	8	16	24	32	40	48	56	64
0	3.56	2.42	1.83	1.84	1.94	1.39	0.63	0.25	0.08
8	2.53	2.01	1.80	1.81	1.79	1.23	0.54	0.21	0.08
16	2.21	1.96	1.85	1.88	1.62	0.95	0.42	0.16	0.06
24	2.21	2.04	1.94	1.71	1.20	0.65	0.28	0.12	0.05
32	1.98	1.80	1.60	1.20	0.74	0.37	0.17	0.08	0.04
40	1.17	1.07	0.86	0.61	0.35	0.19	0.10	0.05	0.02
48	0.52	0.48	0.38	0.27	0.16	0.09	0.05	0.02	--
56	0.21	0.189	0.14	0.12	0.07	0.04	0.03	0.02	--
64	0.08	0.072	0.06	0.05	0.03	0.02	0.02	--	--

Table C - 10: *RID [kg/m²s] of FCN with enlarged central jet.*

Conditions:

P_n [kPa]	$\dot{m}$ [kg/s]	h [cm]	T_w [°C]	d_o [mm]	d_j [mm]	l_j [mm]	ϕ_n [°]
92.2	8.44	26.5	28	37.2	17	0	130

x[cm] / y[cm]	0	8	16	24	32	40	48	56
0	25.90	20.62	15.03	14.71	15.03	9.37	3.52	1.19
8	17.67	14.71	13.02	13.64	13.71	8.68	3.46	1.26
16	14.21	12.76	12.83	13.46	12.14	6.98	2.77	1.01
24	14.08	12.95	12.89	12.32	9.12	4.78	1.95	0.75
32	13.90	13.27	11.82	9.31	5.78	2.77	1.26	0.50
40	9.37	8.55	7.04	4.78	2.70	1.45	0.69	0.25
48	4.65	4.15	3.27	2.33	1.45	0.82	0.38	0.19
56	1.82	1.57	1.32	0.94	0.63	0.38	0.19	--

Table C - 11: *RID [kg/m²s] of FCN with enlarged central jet.*

Conditions:

P_n [kPa]	$\dot{m}$ [kg/s]	h [cm]	T_w [°C]	d_o [mm]	d_j [mm]	l_j [mm]	ϕ_n [°]
65.2	6.59	29	27	37.2	17	0	profiled

x [cm] / y [cm]	0	8	16	24	32	40	48
0	17.50	15.82	12.31	10.53	13.89	7.55	1.31
8	15.35	14.09	11.37	10.95	12.99	4.77	0.94
16	11.47	10.43	9.54	10.79	12.05	3.93	0.58
24	10.37	9.43	9.59	11.42	9.54	2.52	0.37
32	12.52	11.42	10.32	9.43	4.98	1.26	0.26
40	5.45	5.50	3.88	2.67	1.15	0.37	0.05
48	1.00	1.05	0.73	0.58	0.26	0.10	0.89

Table C - 12: *RID [kg/m²s] of commercially available FCN.*

P_n [kPa]	55.3	30.7	30.7	55.3	30.7	30.7	30.7	30.7	30.7	46.7
$\dot{m}$ [kg/s]	5.69	4.23	5.06	6.72	5.3	5.26	4.91	5.56	6.71	8.17
h [cm]	40.5	40.5	40.5	40.5	40.5	40.5	40.5	40.5	40.5	40.5
T_w [°C]	35	35	35	35	35	35	35	35	31	31
d_o [mm]	32	32	37	37	37	37	37	37	45	45
d_i [mm]	14	14	16	16	16	17	16	16	18	18
l_i [mm]	14.5	14.5	0	0	10	10	10	10	0	0
r [cm]	I [kg/m²s]									
0	3.88	3.00	2.44	2.14	5.87	1.91	1.72	1.87	3.04	3.67
8	3.53	2.72	3.01	2.64	5.87	2.49	2.13	2.01	3.02	3.49
16	3.44	2.62	4.36	3.64	4.00	3.55	2.96	1.91	2.72	3.16
24	3.72	2.83	5.06	4.16	2.69	3.66	3.27	1.65	3.74	4.22
32	2.45	1.77	3.10	2.75	1.59	2.03	2.00	1.99	3.20	3.77
40	0.79	0.48	0.96	0.94	0.57	0.62	0.61	2.88	1.34	1.80
48	0.11	0.09	0.20	0.22	0.13	0.10	0.12	0.56	0.33	0.50

Table C - 13: *RID from FCNs with sharp-edged orifices.*

$\dot{m}$ [kg/s]	5.48	5.66	5.66	5.59	5.68	5.43	5.48	5.66	5.74	5.38
d_i [mm]	15	15.5	15.5	15.5	16	15	15.5	15	16	15
l_i [mm]	3	12	13	11.5	11.5	11.5	13	13	13	11
ϕ_n [°]	sharp	110	130	130	130	130	130	130	130	130
r [cm]	I [kg/m²s]									
0	2.88	1.67	1.69	1.26	1.40	1.45	1.71	1.78	1.89	1.14
8	2.81	1.75	1.72	1.30	1.59	1.48	1.71	1.72	1.89	1.22
16	2.96	1.79	1.70	1.46	1.71	1.52	1.78	1.62	1.94	1.35
24	3.18	1.56	1.54	1.48	1.56	1.49	1.57	1.45	1.69	1.35
32	2.28	1.55	1.35	1.40	1.41	1.39	1.38	1.24	1.41	1.32
40	0.83	2.24	1.31	1.39	1.41	1.38	1.29	1.28	1.28	1.33
48	0.45	1.03	1.13	1.18	1.21	1.21	1.10	0.31	1.02	0.31
56	--	0.14	0.63	0.65	0.61	0.68	0.64	0.63	0.57	0.64
64	--	--	0.19	0.18	0.14	0.18	0.17	0.15	0.17	0.18

Table C - 14: *RID from FCNs with: d_o = 37,2 mm, P_n = 30 kPa, h = 29 cm and T_w = 27 °C.*

P_n [kPa]	30.7	30.7	30.7	55.3	88.5	55.3	55.3	55.3	55.3
$\dot{m}$ [kg/s]	4.2	4.45	3.28	3.86	4.9	5.67	5.82	5.96	5.61
d_i [mm]	13.25	14	0	0	0	16	17	18	12 to 17
l_i [mm]	3	3	0	0	0	0	0	0	0
r [cm]	I [kg/m²s]								
0	1.40	0.99	0.01	0.02	0.02	2.91	3.55	5.02	2.12
8	1.45	1.02	0.04	0.03	0.04	3.27	4.02	5.20	2.55
16	2.26	1.04	0.23	0.26	0.28	4.13	4.84	5.63	3.78
24	3.60	1.04	2.37	2.53	2.91	4.14	3.85	3.76	4.22
32	1.95	1.03	2.81	3.36	4.37	1.99	1.70	1.44	2.14
40	0.42	1.06	0.48	0.63	0.89	0.50	0.46	0.37	0.57
48	0.04	0.82	0.05	0.07	0.09	0.10	0.10	0.07	0.31
56	--	0.39	--	--	--	0.01	0.01	0.01	0.02

Table C - 15: *RID from FCNs and HCNs with: sharp-edged orifices, d_o = 32 mm, h = 40,5 cm and T_w = 28 °C.*

P_n [kPa]	39.3	55.3	88.5	30.7	55.3	30.7	55.3	30.7	55.3	30.7
$\dot{m}$ [kg/s]	4.01	4.69	5.94	3.49	4.56	3.49	4.56	3.49	4.56	3.49
ϕ_n [°]	sharp	sharp	sharp	90	90	110	110	130	130	sharp
r [cm]	I [kg/m²s]									
0	0.01	0.01	0.01	0.01	0.01	0.01	0.01	0.00	0.01	0.01
8	0.03	0.03	0.03	0.01	0.02	0.02	0.02	0.02	0.02	0.03
16	0.17	0.20	0.21	0.13	0.19	0.15	0.14	0.14	0.15	0.25
24	1.21	1.29	1.43	0.59	0.88	0.58	0.77	0.59	0.79	4.45
32	3.55	3.85	4.52	2.16	2.26	1.33	1.48	1.20	1.54	1.97
40	1.41	1.87	2.60	2.19	3.53	2.40	2.24	1.69	1.90	0.21
48	0.19	0.29	0.45	0.04	0.15	0.52	0.99	0.88	1.30	0.01
56	--	0.04	0.06	--	--	0.01	0.07	0.19	0.33	

Table C - 16: *RID from HCNs with: d_o = 37,2 mm, h = 38 cm and T_w = 29 °C.*

P_n [kPa]	24.6	39.3	59	81.1	108.2	92.2	61.5	30.7
$\dot{m}$ [kg/s]	4.17	5.3	6.45	7.55	8.69	8.05	6.22	4.67
h [cm]	43	43	43	43	43	34	34	34
T_w [°C]	35	35	33	27	27	29	29	29
r [cm]	I [kg/m²s]							
0	1.49	1.80	2.01	2.37	2.72	3.99	3.24	2.58
8	1.39	1.69	1.91	2.25	2.59	3.71	2.95	2.35
16	1.23	1.51	1.71	1.97	2.33	3.07	2.46	1.92
24	1.00	1.24	1.44	1.66	1.92	2.52	1.99	1.57
32	0.93	1.10	1.29	1.42	1.71	2.70	2.19	1.95
40	1.34	1.34	1.48	1.60	1.90	3.01	2.54	1.96
48	1.31	1.57	1.71	1.88	2.13	1.43	0.98	0.47
56	0.38	0.77	1.11	1.32	1.51	0.32	0.20	0.08
64	0.06	0.18	0.33	0.44	0.55	0.05	0.03	0.01

Table C - 17: *RID from commercial FCN.*

P_n [kPa]	K [-]							
	0.299	0.323	0.367	0.421	0.457	0.509	0.632	0.719
12	0.364	0.391	0.425	0.467	0.496	0.525	0.619	0.631
28	0.351	0.372	0.412	0.453	0.473	0.519	0.592	0.609
49	0.347	0.368	0.407	0.444	0.470	0.506	0.577	0.589
77	0.345	0.364	0.402	0.440	0.467	0.502	0.562	0.590

Table C - 18: *Measured discharge coefficients, C_n, for HCNs with streamlined swirler and T_w = 25,5 °C.*

P_n [kPa]	d_i [mm]			
	12 to 17	16	17	18
11.6	0.939	1.081	0.989	1.283
25.2	1.302	1.551	1.424	1.779
44.3	1.669	2.004	1.831	2.310
60.3	1.752	2.371	2.119	2.687
92.2	1.920	2.906	2.634	3.256
113.1	2.073	3.411	3.048	3.838

Table C - 19: *Measured mass flow rates, $\dot{m}$ [kg/s], through central jets inserted into streamlined swirler.*

$\dot{m}$ [kg/s]	K [-]		
	0.299	0.367	0.457
2.8	80	85	90
3.8	82	86	94
5.3	84	87	96
6.9	86	87	93

Table C - 20: *Measured spray cone angle, 2θ [°].*

P_n [kPa]	$\dot{m}$ [kg/s]	
	streamlined	sharp
3.7	1.24	1.12
12.6	1.84	1.70
24.1	2.45	2.15
43.4	3.28	2.78
56.6	3.78	3.13
78.9	4.40	3.59
99.6	4.97	3.99

Table C - 21: *Measured mass flow rates for HCN with different swirlers but K = 0,367.*

l_i [mm]	15			30			45		
d_o [mm]	$\dot{m}$ [kg/s]								
	3.8	4.9	6.2	3.8	4.9	6.2	3.8	4.9	6.2
32.4	51.0	51.0	50.4	86.7	86.1	86.1	140.2	137.7	140.2
37.2	35.1	33.2	38.7	60.3	56.6	65.2	97.8	92.8	107.6
45.5	21.3	22.1	20.3	36.3	35.7	35.1	59.0	58.4	57.2

Table C - 22: *Measured injection pressure, P_n [kPa], for HCNs with protruding solid core.*

P_n [kPa]	121.8	72.6	36.3	18.4
$(r_o - r)$ [mm]	$\frac{1}{2}\rho v_o^2$ [kPa]			
0	0	0	0	0
0.60	49.91	31.72	15.98	8.11
1.48	35.78	21.02	9.84	5.04
2.36	26.92	16.11	7.13	3.44
3.24	26.68	15.61	7.13	3.44
4.56	29.51	17.21	7.99	3.69
5.88	31.60	18.44	8.61	4.06
6.76	29.75	17.33	8.24	3.93
7.64	24.83	14.63	7.01	4.06
8.52	18.56	11.19	5.29	2.70
9.40	12.54	7.38	3.57	1.84
10.28	6.64	4.67	2.09	1.11
11.16	3.57	2.09	0.98	0.49
12.04	1.60	1.11	0.49	0.25
12.92	0.61	0.37	0.12	0.00
13.80	0.25	0.09	0.00	--
14.50	0.06	0.00	--	--
15.21	0.00	--	--	--

Table C - 23: *Measured dynamic pressure distribution in outlet plane of HCN with d_o = 37,2 mm.*

d_o [mm]									
42.3		45.5		37.2		32.4		21.6	
$(r_o - r)$ [mm]	$½\rho v_o^2$ [kPa]	$(r_o - r)$ [mm]	$½\rho v_o^2$ [kPa]	$(r_o - r)$ [mm]	$½\rho v_o^2$ [kPa]	$(r_o - r)$ [mm]	$½\rho v_o^2$ [kPa]	$(r_o - r)$ [mm]	$½\rho v_o^2$ [kPa]
0.00	0.00	0.00	0.00	0.00	0.00	0.00	0.00	0.00	0.00
0.18	1.23	0.7	1.97	0.60	8.11	0.44	14.76	0.09	13.16
0.35	11.31	1.14	1.35	1.48	5.04	0.88	18.69	0.26	24.23
0.79	16.36	1.58	1.41	2.36	3.44	1.32	16.23	0.70	23.61
1.23	13.65	2.46	1.11	3.24	3.44	1.76	14.14	1.14	21.15
2.11	9.96	3.34	1.35	4.56	3.69	2.20	12.91	1.58	20.29
2.99	8.61	4.22	1.78	5.88	4.06	2.64	12.42	2.02	19.43
3.87	8.73	5.1	2.83	6.76	3.93	3.08	12.05	2.46	19.43
4.75	8.85	5.98	3.57	7.64	4.06	3.52	11.62	2.90	19.06
5.63	9.22	6.86	4.80	8.52	2.70	4.40	11.56	3.34	18.57
6.51	9.35	7.74	5.17	9.40	1.84	5.28	11.19	3.78	18.08
7.39	9.41	9.06	5.29	10.28	1.11	6.16	10.70	4.22	17.46
8.27	8.92	10.38	3.94	11.16	0.49	7.04	9.47	4.66	17.83
9.15	8.24	11.26	2.89	12.04	0.25	7.92	8.24	5.10	17.46
10.03	6.89	12.14	1.78	12.92	0.00	8.80	6.15	5.98	15.86
10.91	5.29	13.02	1.05	--	--	9.68	4.49	6.42	11.19
11.79	3.57	13.9	0.68	--	--	10.56	2.34	6.86	8.61
12.67	1.84	14.34	0.49	--	--	11.00	1.84	7.30	6.03
13.55	0.98	14.78	0.31	--	--	11.88	1.05	7.74	1.48
14.43	0.37	15.22	0.12	--	--	12.76	0.43	8.18	0.43
15.31	0.12	15.66	0.06	--	--	13.64	0.12	8.62	0.06
16.19	0.00	16.1	0.00	--	--	14.52	0.00	9.06	0.00

Table C - 24: *Measured dynamic pressure distribution in outlet plane of various HCNs with P_n = 30,7 kPa.*

APPENDIX D

DESIGNING A FCN

This appendix describes a step by step method for designing specific cooling tower nozzles. The correlations used in this procedure are the same correlations that are given elsewhere in this thesis, except that they have been rewritten to expose the hidden nozzle dimensions.

As demonstration a numerical example is given to show how this design code is implemented. Assume that the following constraints apply:

- water temperature = 45°C
- required intensity, I = 4 kg/m²s
- spray area, b = 1,2 m
- nozzle height, h = 0,35 m
- ΔP_n = 35 kPa.

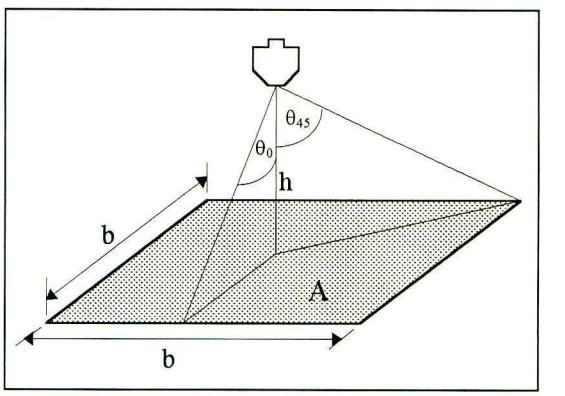

***Figure D - 1** : Nozzle arrangement.*

Since discharge coefficient is directly proportional to $A_p^{0,5}$ and inversely proportional to $d_s,^{0,25}$ it was decided to use the relationship between A_p and d_s from the prototype nozzle as a basis for designing nozzles of other sizes. The following equation can be used to obtain d_s from A_p or vice versa:

$$d_s = 3,6 \times A_p^{0,57}. \qquad \text{(D-1)}$$

The steps that follow are the recommended means of designing a FCN.

1 Calculate the required volume flow rate through the nozzle that will give the desired rainfall intensity for the area to be wetted.

$$A = b \times b$$
$$= 1,2 \times 1,2$$
$$= 1,44 \text{ m}^2$$
$$\dot{m} = I \times A$$
$$= 4 \times 1,44$$
$$= 5,76 \text{ kg/s}.$$

From Equation (A-1) $\rho = 990{,}4\ kg/m^3$

$$\therefore \dot{q} = \dot{m}/\rho$$
$$= 5{,}76/990{,}4$$
$$= 5{,}82 \times 10^{-3}\ m^3/s$$

2 Now calculate the major nozzle dimensions, A_p, d_s and d_o, that will satisfy the recommendation that K be less than 0,5. The process of selecting these dimensions may require iteration because the swirler flow coefficient, E_{sw}, is unknown. The swirler flow coefficient is defined as the percentage of the total mass flow rate passing through the swirl ports. Assume a value for either A_p or d_s and calculate the other from Equation (D-1), then solve Equation (D-2) to obtain a value for d_o. Alternatively values for A_p and d_o can be read directly off Figure D-2, which is a series of solutions of Equation (D-2) for which the nozzle parameter, K, has a value of 0,4. These curves can also be interpolated to find solutions for intermediate rainfall intensities or spray areas. These nozzle dimensions were calculated to yield a K of 0,4, however, this may not always be the most suitable choice. The maximum recommended K value for any specific injection pressure should be read off Figure 6-1.

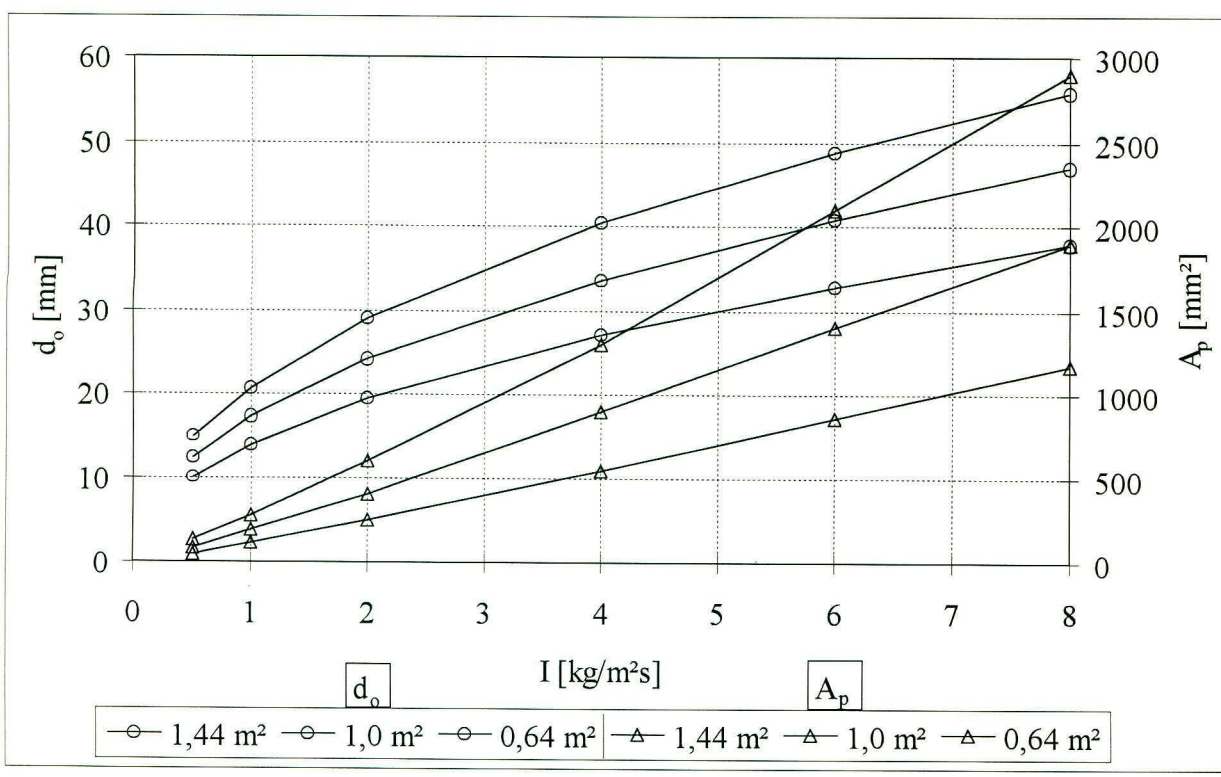

Figure D - 2: *Chart for selecting major nozzle dimensions.*

Equation (D-2) is the closed form solution to the combination of Equation (3-23) and Equation (5-1). Equating these two equations and inserting the unknown swirler flow coefficient, Esw, the following equation is derived:

$$C_n = \frac{E_{sw}\dot{m}}{\rho\sqrt{\frac{2\Delta P_n}{\rho}}\frac{\pi}{4}d_o^{\,2}}$$

$$= 0{,}578K^{0{,}5}\left(d_s/d_o\right)^{0{,}25}$$

eliminating C_n to reveal

$$d_o = \left[\frac{1{,}558E_{sw}\dot{m}d_s^{\,0{,}25}}{\sqrt{\rho\Delta P_n A_p}}\right]^{0{,}8}. \qquad \text{(D-2)}$$

Assuming a value for E_{sw} of 0,82, which is in line with the recommendation of Prywer and Kulesza [87PR1], and a swirl port area, A_p, of 1300 mm^2 the major nozzle dimensions are calculated as follows:

$$d_s = 3{,}6\times\left(1300\times10^{-6}\right)^{0{,}57}$$

$$= 0{,}0815\,m$$

and

$$d_o = \left[\frac{1{,}558\times0{,}82\times5{,}76\times0{,}0815^{0{,}25}}{\sqrt{990{,}4\times35000\times1300\times10^{-6}}}\right]^{0{,}8}$$

$$= 0{,}0411\,m,$$

which yields a K value of 0,388. The anticipated nozzle discharge coefficient cab be calculated from Equation (5-1):

$$C_n = 0{,}578\times0{,}388^{0{,}5}\left(0{,}0815/0{,}0411\right)^{0{,}25}$$

$$= 0{,}427.$$

Alternatively Figure 6-1 can be used to estimate a maximum permissible K for the given flow conditions. In this instance the nozzle supply pressure, Pn, of 35 kPa corresponds to a K value of approximately 0,47. This is correct under the assumption that streamlined swirl ports will be used and a minimum swirler pressure drop, ΔP_{sw}, of 10 kPa will be observed. A smaller K may always be used, so long as the diameter ratio, d_s/d_o remains greater than 2. In order to use Figure D-2 K must be taken as 0,4, which together with the desired rainfall intensity of

4 kg/m²s and a wetted area of 1,44 m² leads to the following approximate solution for the three unknowns:

$d_o \cong 40{,}5$ mm,

$A_p \cong 1300$ mm²

and using the relationship between K, d_o, d_s and A_p:

$$d_s = A_p / d_o K$$
$$= 1300/(40{,}5 \times 0{,}4)$$
$$= 80{,}2\,\text{mm}.$$

There is no difference between the equations used here and those used previously. The small discrepancy in the calculated dimensions is as a result of having read from the graphical solution.

3 Calculate the central jet diameter from Equation (D-3), which is simply Equation (5-4) that has been modified by adding an additional 1,2 mm. This correction compensates for the fact that Equation (5-4) is a correlation for nozzles with sharp-edged orifices, but nozzles with profiled exits are requiring to be designed. Therefore:

$$d_j = 0{,}0193 X^{0{,}117} + 0{,}0012, \qquad \text{(D-3)}$$

where X is calculated from the following equation derived from Equation (5-3):

$$X = \left(\left\{ d_o - 19{,}62 \left[\frac{d_o \dot{q} \mu}{\Delta P_n} \right]^{0{,}25} \right\} \Big/ d_o \right)^2 . \qquad \text{(D-4)}$$

Substitute into Equation (D-4):

$$X = \left(\left\{ 0{,}0411 - 19{,}62 \left[\frac{0{,}0411 \times 0{,}82 \times 5{,}82 \times 10^{-3} \times 5{,}91 \times 10^{-4}}{35\,000} \right]^{0{,}25} \right\} \Big/ 0{,}0411 \right)^2$$
$$= 0{,}127$$

and then into Equation (D-3) to obtain d_j:

$$d_j = 0{,}0193 \times 0{,}127^{0{,}117} + 0{,}0012$$
$$= 0{,}0164\,\text{m}.$$

4 Now check that the total flow rate through the swirler and central jet agrees with the required flow rate. Calculate the jet flow rate from the swirl port flow rate using Equation (5-5). Substituting into this equation yields:

$$\dot{q}_j = 0{,}989\frac{\pi/4 \times 0{,}0164^2}{1300 \times 10^{-6}}0{,}82\dot{q}$$
$$= 0{,}132\dot{q}.$$

The total flow rate through this nozzle is 95,2 percent of the required flow rate, which is suitably accurate for the purpose of nozzle design. However, had the total flow rate at this point been 15 percent out, then it would have been necessary to return to step 2 to re-estimate the swirler flow coefficient and then recalculate the major nozzle dimensions. The solution obtained above is accurate enough and no further iteration shall be performed here.

5 The final step in this design process is to outline the profiled outlet needed to produce a *square* spray pattern. The geometry of the following profile is calculated with the intent that the profile be manufactured on a 3-axis NC machine. It is recommended that the outlet be machined with circular cutter paths that vary in height to produce the profile, see Figure 4-7.

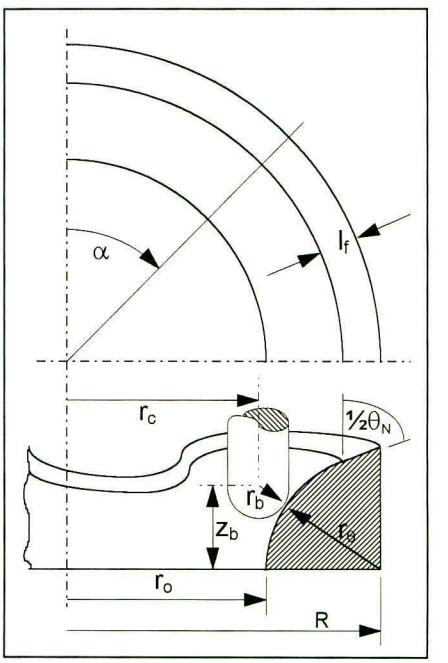

Figure D - 3: *Geometry of profiled outlet.*

- The first thing to note about the profile is that it will be repetitive through 45°, therefore, it is only necessary to determine cutter positions for the first 45° and for as many number of circular cuts necessary to give the desired finish.
- Calculate the required minimum and maximum spray angles for the nozzle, these are θ_0 and θ_{45} in Figure D-1.
- The equation for the required spray angle, i.e. the angle at which the spray should exit the nozzle in order to wet the full spray area, at an arbitrary value of α is:

$$\theta_i = \tan^{-1}\left(\frac{b}{2\,h\cos\alpha_i}\right) \qquad \text{(D-5)}$$

- The half nozzle angle, ϕ_n, is calculated from the following equation:

$$\tfrac{1}{2}\phi_{n_i} = \left(\frac{\theta_i - \theta_0}{\theta_{45} - \theta_0}\right) \times 12^\circ + \theta_i, \qquad \text{(D-6)}$$

where the extra 12° is used to exaggerate the Coanda effect, which would otherwise have little effect on producing a square spray pattern. Alternatively this extra 12° could be viewed as a means of deepening the *grooves* in the exit profile.

- The outer radius of the profiled outlet, R, has a value 1,6 times the radius of the orifice, r_o. This is in keeping with the prototype designs tested throughout this project, however, values in excess of this may also prove useful.
- The radius of the ball-nosed cutter used to machine the outlet is r_b. The more pronounced a profile, the smaller will have to be the cutter in order to machine the sharper curves.
- The width of the flat section of the profile is designated as l_f in Figure D-3.
- The radius of curvature, r_θ, to which the flat section is tangent, is calculated from the following equation:

$$r_{\theta_i} = \frac{\left(R - r_o - l_f\right)}{\left(1 - \cos\left(\tfrac{1}{2}\phi_{\theta_i}\right)\right)}. \qquad \text{(D-7)}$$

- Finally, the cutter height, z_b, can now be calculated from the following equations:

  for $r_{c_i} \leq R - l_f$:

$$z_{b_i} = \sqrt{\left(r_{\theta_i} + r_b\right)^2 - \left(r_{\theta_i} + r_o - r_{c_i}\right)^2} \qquad \text{(D-8)}$$

  and for $r_{c_i} > R - l_f$:

$$z_{b_i} = r_{\theta_i}\sin\left(\tfrac{1}{2}\phi_{\theta_i}\right) + \frac{r_{c_i} - R + l_f}{\tan\left(\tfrac{1}{2}\phi_{\theta_i}\right)} + \frac{r_b}{\sin\left(\tfrac{1}{2}\phi_{\theta_i}\right)}. \qquad \text{(D-9)}$$

There is one last alteration, which must be done to the co-ordinates calculated with the above equations before they can be included in the NC codes for machining the profile, and that is to translate these values to between 30° and 40° in the direction in which the liquid will be spinning when it exits the nozzle. This translation is vital to the success of the nozzle because of the fact that water leaving the nozzle does not exit in a purely radial direction, which is due to the significant tangential component of velocity. Without translating the co-ordinates for the *groove*, the spray is likely to separate from the profiled exit causing instabilities and unpredictable spray cone angles. This translation is illustrated in Figure D-4.

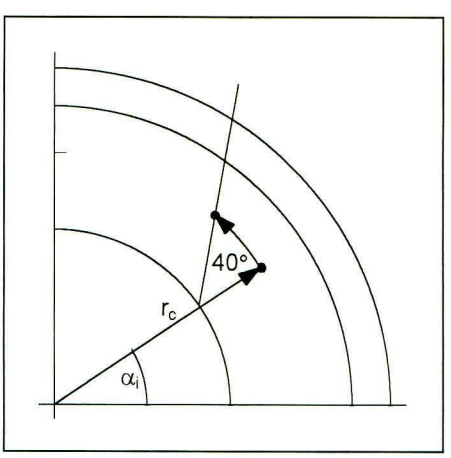

***Figure D- 4**: Translation of cutter co-ordinates.*

The final consideration, which specifically concerns nozzle assembly in a cooling tower, is the orientation of the profiled exit relative to the desired orientation of the *square* spray pattern. This particular aspect was overlooked in this project even though it is certain that this global would affect the spray orientation. However, the single profiled exit that was tested, was found to spray squarely onto the projected spray area when the line drawn between opposing groove exits was orientated at an angle of 12° relative to the axis of the supply pipe. Figure D-5, shows the orientation of the tested profile against the supply pipe. The 12° angle discussed here may be used as a guide, however, it is recommended that individual outlets be tested experimentally to determine their required orientation.

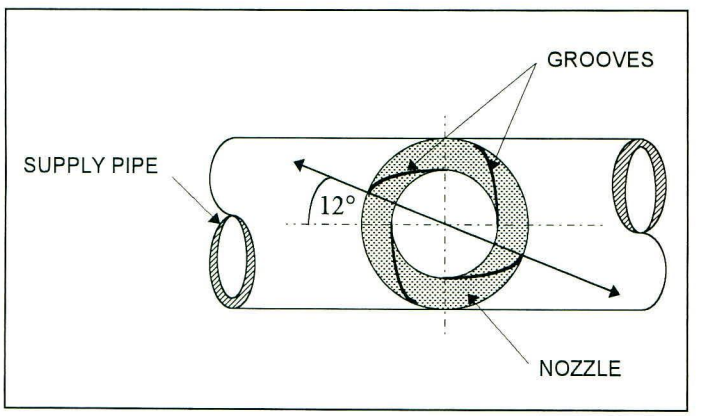

Figure D - 5: *Outlet orientation.*